

WEB BUCKLING CAPACITY OF STEEL BRIDGE BOX GIRDERS DURING
INCREMENTAL LAUNCHING

by

Riccardo Ciccarelli

Submitted in partial fulfilment of the requirements
for the degree of Master of Applied Science

at

Dalhousie University
Halifax, Nova Scotia
August 2023

Dalhousie University is located in Mi'kma'ki,
the ancestral and unceded territory of the Mi'kmaq.
We are all Treaty people.

TABLE OF CONTENTS

LIST OF TABLES	v
LIST OF FIGURES	vii
ABSTRACT	x
LIST OF ABBREVIATIONS AND SYMBOLS USED	xi
ACKNOWLEDGEMENTS	xiv
CHAPTER 1 INTRODUCTION.....	1
1.1 Background on Incremental Girder Launching.....	1
1.2 The Launching Method	2
1.3 Behaviour of Girder Webs During Launching.....	4
1.4 Purpose of the Research	5
1.5 Objectives and Scope	6
1.6 Outline of the Research	6
CHAPTER 2 LITERATURE SURVEY.....	8
2.1 General	8
2.2 Elastic Buckling of Steel Plates under Patch Loading.....	9
2.3 Inelastic Behaviour of Steel Plates and Girder Webs Subjected to Patch Loading.....	14
2.4 Girders Subjected to Loading Combinations	20
2.4.1 Girders Subjected to Combined Patch Loading and Shear.....	20
2.4.2 Girders Subjected to Combined Patch Loading and Bending	22
2.4.3 Girders Subjected to Combined Patch Loading, Shear, and Bending	26
2.5 General Code Requirements.....	28
2.5.1 Canadian Highway Bridge Design Code	28
2.5.2 AASHTO Bridge Design Specifications	29
2.5.3 Eurocode 3 Part 1-5 Design of Plated Structures.....	29
2.5.4 Commonalities among the Design Codes	31
2.6 Summary	32
CHAPTER 3 EXPERIMENTAL PROGRAM.....	33
3.1 General	33
3.2 Existing Bridge Background and Site Features.....	33

3.3	Test Specimens.....	37
3.4	Material Properties	42
3.5	Field Test Set-Up	43
3.6	Data Acquisition Equipment & Instrumentation.....	45
3.6.1	Strain Gauges	45
3.6.2	Data Acquisition Equipment.....	47
3.7	Test Procedure.....	49
3.8	Potential Sources of Error from Field Testing	51
CHAPTER 4 EXPERIMENTAL RESULTS.....		53
4.1	General	53
4.2	Global Load Effects	54
4.3	Theoretical Stresses at Gauge Field	55
4.4	Post Processing of Recorded Data	55
4.5	Experimental Results.....	56
4.5.1	Girder 1 Recorded Stresses	58
4.5.2	Girder 2 Recorded Stresses.....	60
4.6	Concluding Remarks	65
CHAPTER 5 FINITE ELEMENT ANALYSIS.....		66
5.1	General	66
5.2	Description of Elements	66
5.3	Material Stress-Strain Relationship.....	67
5.4	Girder Model Length & Finite Element Mesh.....	69
5.5	Initial Web Geometric Imperfections.....	73
5.6	Boundary Conditions & Load Application	74
5.7	Nonlinear Buckling Analysis	75
5.8	Verification of the Finite Element Model	76
5.8.1	Verification of G1 and G2 Flange Stresses.....	76
5.8.2	Comparison of the Experimental Versus FE Web Stresses	78
5.8.3	Verification of the Plate Girder Model from Literature.....	81
5.9	Summary	83
CHAPTER 6 PARAMETRIC STUDY.....		84
6.1	General	84

6.1.1	Girder Geometry Development and Applied Loading.....	84
6.1.2	Finite Element Model Characteristics.....	86
6.2	Effect of Web Thickness	87
6.3	Effect of Web Height	88
6.4	Effect of Web Inclination.....	90
6.4	Effect of Web Stiffener Spacing	92
6.4.1	Effect of Stiffener Thickness	94
6.5	Effect of Flange Thickness.....	96
6.6	Effect of Residual Stresses.....	98
6.7	Comparison of P_{cr} with CSA S6 (2019) Web Bearing Resistances	100
6.8	Comparison of P_{cr} with Eurocode 3 Part 1-5 (2006).....	102
CHAPTER 7 CONCLUSIONS AND RECOMMENDATIONS.....		106
7.1	Summary	106
7.2	Conclusions	107
7.3	Recommendations	108
REFERENCES.....		110
APPENDIX A		115
APPENDIX B		121
APPENDIX C		123

LIST OF TABLES

Table 3.1: Nominal dimensions of tested box girder sections	38
Table 3.2: Location of the gauge field & web panel dimensions	39
Table 3.3: Shubenacadie River Bridge steel plate properties	42
Table 3.4: Vertical and longitudinal spacing of web strain gauges	44
Table 4.1: Global load effects	54
Table 4.2: Theoretical stresses	55
Table 4.3: Strain gauge # paring	56
Table 5.1: Element summary	67
Table 5.2: One-bay versus three-bay stresses above roller support.....	70
Table 5.3: Mesh convergence study results	70
Table 5.4: Comparison of flange stresses between numerical and theoretical models.....	78
Table 5.5: Relevant properties of girder specimens tested by Granath et al. (1999).....	81
Table 5.6: Comparison of FE results with specimens from Granath et al. (1999)	82
Table 5.7: Comparison of the critical buckling load to the web yielding and crippling resistances	83
Table 6.1: Summary of girders used to create the parametric study envelope	85
Table 6.2: Geometric properties & FE results per web; effect of web thickness	87
Table 6.3: Geometric properties and FE results per web; effect of web height.....	89
Table 6.4: Web inclination and corresponding slope.....	91
Table 6.5: Geometric properties and FE results per web; effect of web inclination	91
Table 6.6: Geometric properties and FE results per web; effect of stiffener spacing.....	93
Table 6.7: Geometric properties and FE results per web; effect of vertical stiffener thickness.....	95
Table 6.8: Geometric properties and FE results per web; effect of flange thickness	97
Table 6.9: Properties of girder models and FE results; effect of residual stresses	99
Table 6.10: B_{ry} and B_{rc} values for web thicknesses considered	101
Table A.11: Procedure to determine the critical buckling height, H_{cr} , of Girder G1:	115
Table A.12: Procedure to determine the critical buckling height, H_{cr} , of Girder G2:	118
Table B.1: Strain gauge properties - G1	121
Table B.2: Strain gauge properties - G2	122

Table C.1: Worked example - critical buckling stress	123
Table C.2: Calculation of B_{ry} and B_{rc} from CHBDC (CSA S6, 2019).....	129
Table C.3 Calculation of F_{cr} from Eurocode 3 (EN 1993 1-5, 2006)	130

LIST OF FIGURES

Figure 1.1: General girder launching process	2
Figure 1.2: Cross section of a box girder supported by roller bearing assemblies, including lateral restrainers.....	3
Figure 2.1: Plate subjected to patch loading adapted from Zetlin (1955).....	8
Figure 2.2: Thin steel plate subjected to uniform compressive edge load studied by Timoshenko (Timoshenko, 1934).....	10
Figure 2.3: Plate model used by Zetlin (1955)	11
Figure 2.4: Plate girder subjected to patch loading (Lagerqvist 1994).....	12
Figure 2.5: Equivalent edge strips effective in resisting load after critical buckling load levels (Timoshenko, 1961).....	14
Figure 2.6: Three prominent failure modes for girders subjected to patch loading (Gozzi, 2007)	15
Figure 2.7: Schematic of web crippling and web yielding adapted from Tang (2005)	16
Figure 2.8: Specimens tested by Granath and Lagerqvist (1999).....	19
Figure 2.9: Interaction between shear and patch loading adapted from Graciano and Ayestarán, 2013	22
Figure 2.10: Interaction between patch load and bending moment proposed by Lagerqvist and Johansson (1996).....	25
Figure 2.11: Transverse loading arrangements corresponding to specific k_F values. Adapted from Eurocode 3 (EN 1993 1-5, 2006).....	31
Figure 3.1: Halifax bound structure during construction (north girder shown).....	34
Figure 3.2: Satellite image of the Shubenacadie River Bridge construction site (Google Maps, 2015)	35
Figure 3.3: Schematic plan and elevation views of the Halifax bound bridge	36
Figure 3.4: Geometry of a typical box girder cross section	38
Figure 3.5: Schematic elevation view of the progression of the gauge field from the West to East abutment for Girder 1	39
Figure 3.6: Schematic elevation view of the progression of the gauge field from the West to East abutment for Girder 2	40
Figure 3.7: Partial plan and elevation views of the gauge field on Girder 1	41
Figure 3.8: Partial plan and elevation views of the gauge field on Girder 2	41
Figure 3.9: Elevation and sectional views of the web and flange strain gauge arrangement.....	44

Figure 3.10: Completed gauge field on the outside web of Girder 2.....	46
Figure 3.11: Testing of a uniaxial strain gauge on the inside web of Girder 2.....	46
Figure 3.12: Data acquisition equipment arrangement of Girder 2	48
Figure 3.13: Photos of the CR5000 data logger (left) and two multiplexers (right).....	48
Figure 3.14: Gauge field of Girder 1 approaching pier 1	50
Figure 4.1: Elevation view of strain recording locations	53
Figure 4.2: Strain gauge numbering schematic - outside web surface	57
Figure 4.3: Strain gauge numbering schematic – inside web surface.....	57
Figure 4.4: G1-A results	58
Figure 4.5: G2-A results	60
Figure 4.6: G2-C results.....	62
Figure 4.7: G2-D results	63
Figure 5.1: Material models used to verify the experimental results.....	68
Figure 5.2: Material model used for the parametric study.....	68
Figure 5.3: Extents of one-bay and three-bay finite element models	69
Figure 5.4: G1 model discretization (cross section)	71
Figure 5.5: G1 model discretization (isometric view)	71
Figure 5.6: G2 model discretization (cross section)	72
Figure 5.7: G2 model discretization (isometric view)	72
Figure 5.8: Initial web out-of-straightness shape (G1 cross section shown, G2 similar) .	73
Figure 5.9: Example of the loads applied to the cross section.....	75
Figure 5.10: G1-A flange stresses.....	77
Figure 5.11: G2 flange stresses (G2-A shown, G2-C and G2-D stresses similar)	77
Figure 5.12: G2-A longitudinal (left) and vertical (right) web stresses.....	79
Figure 5.13: G2-D longitudinal (left) and vertical (right) web stresses.....	80
Figure 5.14: Test set up by Granath et al. (1999)	81
Figure 5.15: Example of the critical web buckling stress (specimen A61p shown).....	82
Figure 6.1: Box girder geometric schematic.....	85
Figure 6.2: Critical buckling stress versus web panel slenderness for web thicknesses of 10mm to 16mm.....	87
Figure 6.3: Critical buckling stress versus web panel slenderness for web heights of 1500mm to 3000mm.....	90

Figure 6.4: Critical buckling stress versus web inclination	92
Figure 6.5: Critical buckling stress versus web panel aspect ratio for stiffener spacing of 1m to 8m.....	94
Figure 6.6: Critical buckling stress versus web panel aspect ratio for vertical stiffener thicknesses of 16mm to 40mm	95
Figure 6.7: Critical buckling stress versus the ratio of flange to web thickness.....	97
Figure 6.8: Idealized longitudinal residual stress profile applied to the FE models.....	99
Figure 6.9: Critical buckling stress versus applied residual stress.....	100
Figure 6.10: Critical load versus web thickness for varying h/w ratios.....	102
Figure 6.11: Critical load versus h/w for (a) a/h=1.9, (b) a/h=2.8, and (c) a/h=3.8	103
Figure 6.12: Critical load versus a/h for (a) h/w=125, (b) h/w=167, and (c) h/w=200 ..	105
Figure A.1: G1-A cross section (S-Frame, 2023)	115
Figure A.2: G1-A buckling analysis set up (S-Frame, 2023)	116
Figure A.3: G1-A buckled shape and H_{cr} (S-Frame, 2023)	117
Figure A.4: G2-A cross section (S-Frame, 2023)	118
Figure A.5: G2-A buckling analysis set up (S-Frame, 2023)	119
Figure A.6: G2-A buckled shape and H_{cr} (S-Frame, 2023)	120
Figure C.1: Box girder section schematic.....	123
Figure C.2: Nodal loads applied in FE model (S-Frame, 2023)	125
Figure C.3: Example of update geometry window; 8 mm imperfection applied (S-Frame, 2023)	126
Figure C.4: Model B3.2 buckled shape and H_{cr} (S-Frame, 2023)	126
Figure C.5: Non-linear analysis set up (S-Frame, 2023)	127
Figure C.6: Model B3.2 non-linear static stress results (S-Frame, 2023).....	128

ABSTRACT

The incremental launching method for bridge construction continues to gain popularity over conventional girder erection methods. During the launching operation, the bridge superstructure (or components of the superstructure) is “moved” along a series of rollers or sliding bearings. These rollers are removed following the launch and the bridge is lowered to rest on permanent bearings. An important design component of launched steel girders is that these girders need to be designed for launch load cases of combined bending moment and a traveling concentrated patch load applied by the temporary roller bearing. Although the current Canadian Highway Bridge Design Code (CSA S6, 2019) addresses web yielding and web crippling at the ultimate limit state, little guidance is provided to determine the buckling capacity of the web panel while the stress level is low. For typical steel bridge box girders, the slenderness ratio of the web is large and thus, web panel buckling within the elastic stress range is likely the predominant failure consideration during girder launching.

This research, consisted of both field work and a numerical study, was motivated to provide a general understanding of the behaviour of box girder webs subjected to the combination of patch load and flexure in the elastic stress range. The field monitoring phase of the research involved installing strain gauges on two steel box girders of the Shubenacadie River Bridge and collecting field readings during their erection in 2014. A finite element model was developed to simulate the stresses in the girders during the launch. However, difficulties related to winter field work resulted in unreliable field data. As such, the finite element model developed for comparison with the field monitoring program was verified using other methods. A numerical study was subsequently conducted using finite element models to investigate the effects of several influential geometric parameters on web buckling of box girders. The comparison of numerical results with design equations from CSA S6 (2019) shows that web panel buckling can occur at significantly lower load levels than those causing web yielding or crippling. Comparison of the numerical results with Eurocode 3 (2006) shows that the Eurocode provides an accurate estimate of critical buckling capacity when web panel buckling is concerned.

LIST OF ABBREVIATIONS AND SYMBOLS USED

a	longitudinal spacing of vertical web stiffeners
ASHTO	American Association of State Highway and Transportation Officials
ASTM	American Society for Testing and Materials
a/h	web panel aspect ratio
b	longitudinal spacing of strain gauges
B_{ry}	web yielding resistance from CSA S6
B_{rc}	web crippling resistance from CSA S6
b_1	top flange width
b_2	bottom flange width
CHBDC	Canadian Highway Bridge Design Code S6
CSA	Canadian Standards Association
D	plate flexural rigidity
DOF	degree of freedom
E	modulus of elasticity
E_s	modulus of elasticity for steel
F_{cr}	critical buckling resistance
FE	finite element
F_R	patch load resistance
F_y	yield stress
F_u	applied patch load; ultimate tensile stress
GF	gauge factor
G1	Girder 1; North girder, Shubenacadie River Bridge
G2	Girder 2; South girder, Shubenacadie River Bridge
H_{cr}	critical web buckling height (height of maximum buckled amplitude)
h	web height
h_{slope}	web height measured along the slope of the web for box girders
h_w	web height
h/w	web slenderness ratio
k_F	critical buckling coefficient
k_{FE}	critical buckling coefficient obtained through FE analysis

L_{eff}	modified effective load length
LRFD	Load and Resistance Factor Design
l_y	effective load length
M	applied bending moment
M_R	moment resistance
MTR	Material Test Report
N	length of bearing
P	applied patch load
P_{cr}	critical buckling load
P_R	ultimate patch load resistance
r	length of roller support
R_b	reduction factor to account for the presence of bending moment
s	vertical spacing of strain gauges
S_s	patch load length
t_f	flange thickness
t_w	web thickness
t_1	top flange thickness
t_2	bottom flange thickness
ν	Poisson's ratio
V	applied shear force
V_r	change in electrical resistance
V_R	shear resistance
w	web thickness; plate thickness
w_1	distance between box girder top flanges
β	flange torsional restraint stiffness parameter
θ	web slope relative to the horizontal axis
λ	buckling factor; eigenvalue
$\bar{\lambda}_F$	slenderness parameter defined by Eurocode 3 Part 1-5
$\mu\varepsilon$	microstrain
Υ_{M1}	reduction factor from Eurocode 3 Part 1-5
σ_b	applied bending stress

σ_{BF}	bottom flange longitudinal stress
σ_{cr}	critical buckling stress
σ_{RC}	compressive residual stress
σ_{RT}	tensile residual stress
σ_{TF}	top flange longitudinal stress
τ_{Max}	maximum web shear stress
Φ_{bi}	resistance factor for web yielding and crippling from CSA S6
$\chi(\lambda)$	yield strength reduction function from Eurocode 3 Part 1-5

ACKNOWLEDGEMENTS

First, I would like to thank my supervisor, Dr. Yi Liu, for her guidance, support, and incredible patience throughout this thesis, as well as providing me with the opportunity to work on this project.

Thank you to my committee members, Dr. Kyle Tousignant and Dr. George Jarjoura, for taking the time to review this research project.

I would like to thank NSERC IPS and Harbourside Engineering Consultants for providing funding to conduct this research. I would also like to thank Harbourside Engineering Consultants for their technical guidance throughout the project.

For their assistance and cooperation during the field monitoring phase of this research, I would like to thank Mike Archibald (Dexter Construction Ltd.), Marc Gasparetto (Cherubini Group), Brian Liekens (Dalhousie University), Jesse Keane (Dalhousie University), Brian Kennedy (Dalhousie University), and Blair Nickerson (Dalhousie University). I would also like to thank Matthew Sauer (Altair S-Frame) for his technical assistance with S-Frame.

Thank you to Shelley Parker, Tiffany Cooper, June Ferguson, and Allyson Fitch for their administrative assistance and general encouragement.

Special thank you to my family, especially to my parents and mother-in-law for their unwavering support. Finally, to my wife, Cassie: thank you for putting your life on hold and for taking care of our family, especially over the past year, as I worked to complete this thesis. This would not have been possible without you all.

"Success is a tale of obstacles overcome, and for every obstacle overcome, an excuse not used." - Robert Breault

CHAPTER 1 INTRODUCTION

1.1 Background on Incremental Girder Launching

The incremental launching method has become increasingly popular over conventional bridge construction methods. In this method of construction, bridge girders are assembled on one side of the obstacle that is to be crossed and are then incrementally pushed or pulled (“launched”) until the girders are in their final position. Figure 1.1 schematically illustrates this process, where the arrow indicates the launching direction.

This method of construction can be applied to either steel or concrete bridges. The first girder erected by the launching method was a post-tensioned concrete bridge spanning the Caroni River in Venezuela in 1963 (Baur, 1977). Through advancements in both construction equipment and design practice, this method has evolved to be applied to steel plate girder and box girder bridges. The first steel bridge launched in North America is believed to be a railroad box girder bridge owned by the Kansas City Southern Railroad in 1970 (Durkee, 1972).

The launching method is preferred over conventional construction methods in locations with deep valleys, water crossings with steep slopes, and environmentally protected regions. As environmental laws and regulations continue to limit permissible work in sensitive environmental areas, the launching method, because of its minimal disturbance to surroundings, provides an attractive alternative over conventional construction methods.

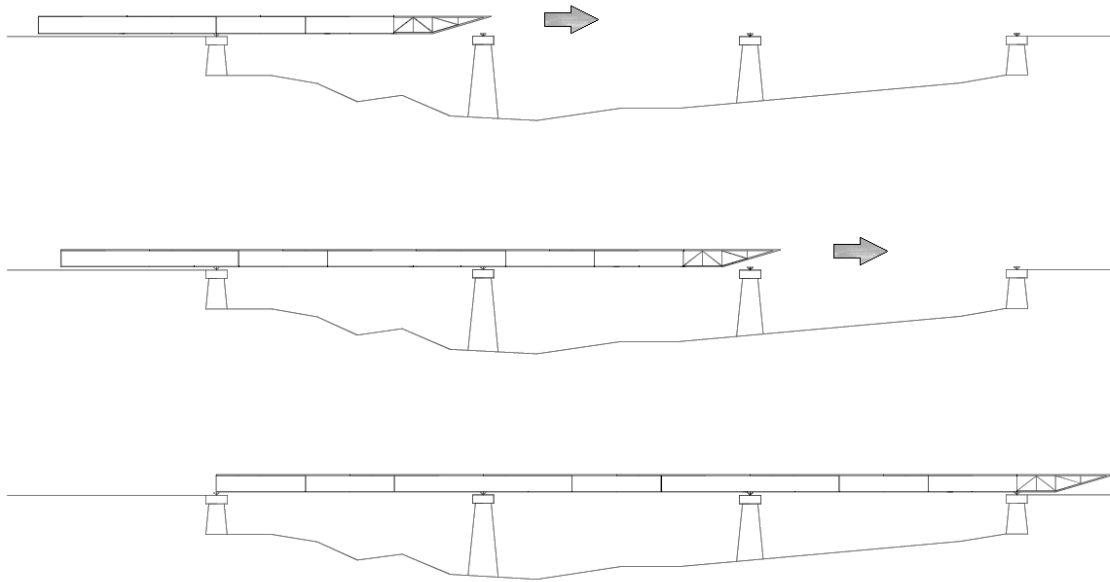


Figure 1.1: General girder launching process

1.2 The Launching Method

The launching method generally involves the assembly of a girder on site and incrementally launching it over a series of piers from one abutment to the other. Launch pads are temporary structural components that are located on the bridge approach and provide a support location on which girder segments can be offloaded and spliced together. Once a sufficient counterweight has been established (i.e., enough girder segments have been spliced together), pulling or pushing of the girder can begin. As the girder is launched, remaining girder segments are added to the end of the girder until the entire girder has been spliced together, as shown in Figure 1.1.

To allow longitudinal movement of the girder, roller bearings are installed at abutment, pier, and launch pad locations. Roller bearings are typically positioned beneath the webs of the girder, under the bottom flange. Lateral restrainers are present at every roller location and prevent excessive lateral movement of the girder while it is in motion. Figure 1.2 illustrates a typical roller bearing assembly and lateral restrainer. In some cases, instead of using single rollers, double rollers are used to better distribute the reaction force. Once the

girder has arrived at its final longitudinal position, all rollers are removed. Using hydraulic jacks, the girders are lowered and adjusted to rest on permanent bearings.

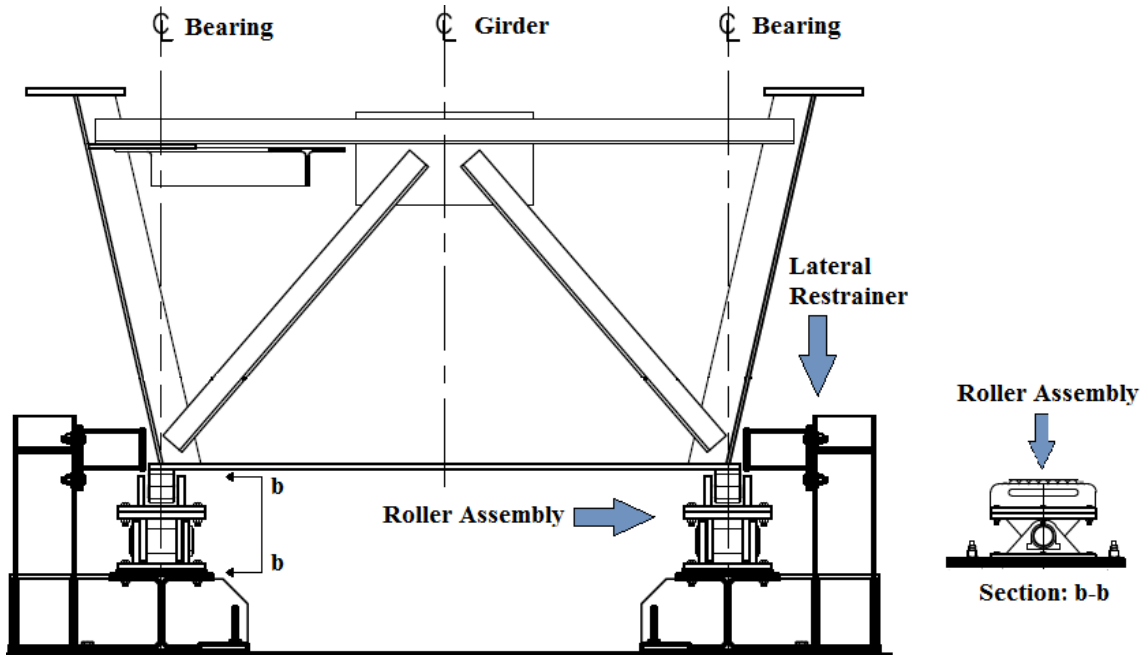


Figure 1.2: Cross section of a box girder supported by roller bearing assemblies, including lateral restrainers

A nosing assembly (which is the tapered truss segment on the leading end of the girder in Figure 1.1), can be utilized to allow the girder to ride onto an oncoming bearing. The launching nose controls leading end tip deflections by reducing the dead load of the cantilevered span, and its tapered profile assists in ‘lifting’ the mass of the girders as they are launched forward onto an oncoming bearing.

Although the practices described above are the most frequently used, certain circumstances allow for alternate launch schemes. For example, rather than launching a single girder, groups of girders can be launched together as one unit. In those cases, cross bracing or diaphragms are installed prior to the commencement of the launch.

1.3 Behaviour of Girder Webs During Launching

When girders are erected via the launching method, they experience varying load effects throughout the entirety of the launch. In particular, at certain times during the launch, the girder experiences concentrated reaction forces, introduced by temporary roller bearings, in combination with in-plane bending moment and shear, due to its self-weight, at critical locations along the length of the girder. Typically, these critical locations correspond to a position on the girder where the web is unstiffened (i.e., between two vertical stiffeners), creating a situation where the web panel is vulnerable to instability. Since it is not economical to provide closely spaced vertical stiffeners, or continuous horizontal stiffeners throughout the entire length of the girder, it is necessary that the resistance of the unstiffened web panel is adequate to resist this type of loading.

During launching, the concentrated load applied from a temporary roller bearing is transferred through the bottom flange of the girder into the web. Since this concentrated load acts over a localised length of the web panel, it is called patch loading or partial edge loading. The girder is also subjected to global bending and shear stresses from its dead load. The combination of these stresses in the web, coupled with geometric initial imperfections and inherent residual stresses, makes the evaluation of web behaviour a complex problem.

Previous studies showed that three failure modes exist for an unstiffened web panel subjected to a concentrated support reaction applied through the bottom flange. The observed failure mode largely depends on the slenderness of the web. The potential failure modes are local web yielding directly above the applied load, local buckling in the lower part of the web near loaded flange (web crippling), and overall web buckling of the web panel. Stocky webs tend to fail by web yielding, while more slender webs fail by web crippling or web panel buckling.

Numerous experimental and numerical studies have been conducted over the past six decades to investigate the behaviour of girder webs subjected to localized edge loading in combination with global loading. The majority of the research in this area has been focused

on isolated plates and I-shaped plate girders, and as a result, design provisions have been developed from that body of work. Conversely, research conducted on webs of box girders is limited (Zhang and Luo, 2012). Due to differences in boundary conditions and geometric alignment between the webs of a plate and a box girder, the findings derived from plate girders may not be directly transferrable to box girders without experimental or numerical verification (Chen, 1994). An examination of the literature suggests that little research has been conducted to investigate web panel buckling capacity specific to box girder bridges.

1.4 Purpose of the Research

The Canadian Highway Bridge Design Code (CHBDC) CSA S6 (2019), the American Association of State Highway and Transportation Officials (AASHTO) LRFD Bridge Design Specifications (2015), and Eurocode 3 Part 1-5 Design of Steel Structures (2006), address the web yielding and web crippling capacities of plate girders. In addition, the design codes restrict the slenderness ratio of webs to prevent web breathing and local buckling due to compression. However, little guidance is provided for determining the web panel buckling capacity with various levels of moment and shear. This lack of guidance is important to this research, as web panel buckling is likely the most predominant failure consideration for typical launched steel plate or box girders due to their large web slenderness ratio.

Finite element analysis is used in industry design practice to determine the buckling capacity of web panels subjected to combinations of patch loading and global loading effects. The ability of modern software to incorporate residual stresses, geometric imperfections, material properties, and second-order effects into finite element models makes it an attractive analysis tool. However, the use of finite element modeling is often time consuming and expensive in terms of model development and computing cost. Therefore, its use may not be justified during the preliminary design phase. When proportioning girder webs for launching load cases, designers often resort to conservative solutions by using thick webs, adding closely spaced vertical stiffeners or adding continuous horizontal web stiffeners.

In light of the above, this research investigates the buckling behaviour of steel box girder webs subjected to patch loading in combination with bending moment. An experimental program was conducted where web stresses in two bridge box girders, erected via the launching method, were monitored during erection of the girders. Concurrent with the experimental program, a numerical study using non-linear buckling finite element analysis was also conducted to further investigate the effects of several influential parameters on the web panel buckling behaviour of box girder webs. It is hoped that the results of this study will provide practical recommendations on web panel behaviour to improve the design of webs of box girders erected by the launching method.

1.5 Objectives and Scope

This study was conducted to develop a better understanding of the behaviour of steel box girder webs subjected to patch loading in combination with in-plane bending. The objectives of this experimental and numerical study were:

- 1 To conduct an experimental monitoring study of the stress levels present in the webs of the Shubenacadie River Bridge box girders during launching;
- 2 To develop numerical models capable of simulating the behaviour of webs subjected to various combinations of loading;
- 3 To conduct an in-depth numerical study to investigate the effect of several influential parameters on the behaviour of box girder web panels subjected to combined patch loading and flexure; and
- 4 To make recommendations on the current design practice where appropriate.

1.6 Outline of the Research

A review of the literature most relevant to the present research, as well as the design philosophies applied in current design guidelines, are included in Chapter Two. Chapter Three presents a detailed description of the experimental program, which was designed to obtain the stress levels present in the webs of the steel box girders of the Shubenacadie

River Bridge during launching. The experimental results are presented in Chapter Four. The finite element model developed to verify experimental results is presented in Chapter Five and the results of an in-depth parametric study are presented in Chapter Six. Finally, a summary of conclusions, as well as recommendations for further research, are presented in Chapter Seven.

Appendix A contains an outline of the preliminary analysis used to determine the critical locations for placement of strain gauges. Detailed information about the strain gauges used in the experimental program is presented in Appendix B. Worked examples demonstrating the procedures used to obtain the FE critical buckling stresses, the web yielding and crippling resistances from CSA S6, and the critical buckling load from Eurocode 3 are presented in Appendix C.

CHAPTER 2 LITERATURE SURVEY

2.1 General

Research on elastic buckling of thin steel plates subjected to uniform compression dates back to the mid-1930s. Since then, a set of classic solutions have been derived to calculate the buckling capacity of such plates, accounting for various boundary conditions and common loading scenarios (Ziemian, 2010). Traditionally, researchers have separated the theoretical studies of the elastic critical buckling loads from studies on the ultimate load carrying capacities. However, as the buckling and ultimate resistance of plates are co-dependent, current design codes have incorporated the effects of buckling into the ultimate resistance functions (Loaiza et al., 2019).

Studies on the behaviour of steel plates subjected to patch loading began in the 1950s. It was found that the presence of a patch load, shown in Figure 2.1, produced failure mechanisms not previously seen in uniform loading situations, and also reduced the buckling capacity of plates.

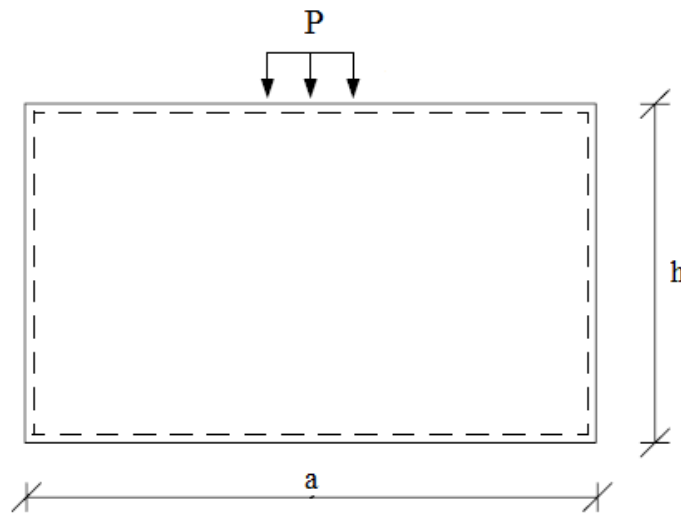


Figure 2.1: Plate subjected to patch loading adapted from Zetlin (1955)

From the 1970s onward, the effects of structural imperfections (namely residual stresses from welding and fabrication) and geometric imperfections of steel plates were studied. Subsequently, these effects were, to varying extents, incorporated into research on the

buckling behaviour of plates and plate girders. Further, as computer technology advanced, numerical modeling based on finite element methods proved to be an effective tool to study parameters such as patch load lengths, scenarios of patch loading combined with bending and shear, girder geometric properties, and various boundary conditions.

A review of available literature illustrates that, compared to I-shaped plate girders, research conducted on webs of box girders is limited (Zhang and Luo, 2012). While it is commonly agreed that the general design principles for plate girders are applicable to box girders, the design formulae developed specifically for I-shaped plate girders cannot be applied wholly or directly to box girders without experimental or numerical verification (Wolchuk, 1980). The basis for this argument is that the interaction between flanges and webs of box girders is different from the interaction in plate girders (Chen, 1994).

Since research on plate girders formed the foundation for work in the area of box girders on this subject, this chapter begins with a review of research pertaining to the elastic and inelastic behaviour of plates subjected to patch loading in sections 2.2 and 2.3. Research on the behaviour of plate girder webs subjected to combinations of patch loading with shear, and/or bending is presented in section 2.4. This is followed by a brief review of the relevant code requirements found in the Canadian, American, and European bridge design codes in section 2.5.

2.2 Elastic Buckling of Steel Plates under Patch Loading

The elastic buckling behaviour of thin steel plates subjected to a uniform compressive edge load applied along the entire length of the plate, as shown in Figure 2.2, was first investigated by Timoshenko (1934).

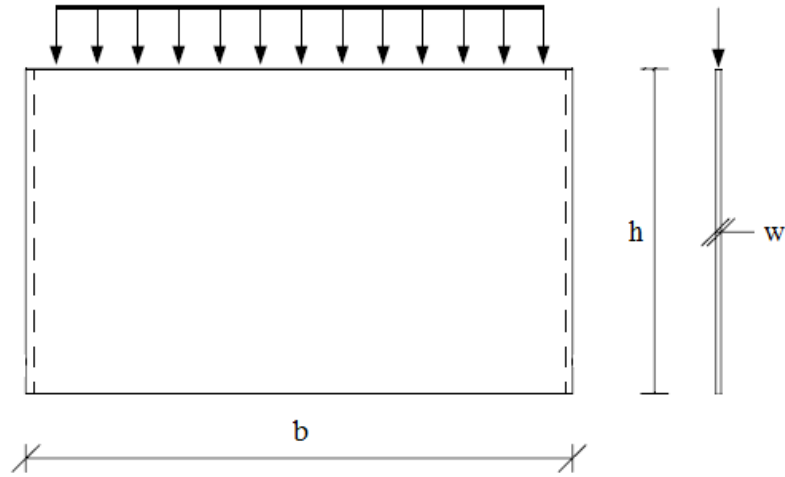


Figure 2.2: Thin steel plate subjected to uniform compressive edge load studied by Timoshenko (Timoshenko, 1934)

He derived an equation for calculating the critical elastic buckling stress (σ_{cr}) expressed in Equation [2.1] as:

$$\sigma_{cr} = \frac{k\pi^2 E}{12(1 - \nu^2)} \left(\frac{w}{b}\right)^2 \quad [2.1]$$

where b is the plate width, w is the plate thickness, and k is a buckling coefficient that accounts for the effects of plate aspect ratio, boundary conditions, and loading conditions. As indicated, the critical compressive buckling resistance is affected by the plate thickness to width (w/b) ratio. Poisson's ratio is included to account for the two-way action involved in plate buckling (Kulak and Grondin, 2010). This classic solution has formed the basis for subsequent research by others.

The first work in assessing buckling loads of flat rectangular plates subjected to partial edge loading was performed by Zetlin (1955). By applying the energy method to solve the differential equations of simply supported plates he derived Equation [2.2] for the critical buckling load:

$$P_{cr} = k_{cr} \frac{\pi^2 D}{b^2} \quad [2.2]$$

where P_{cr} is the critical buckling load, k_{cr} is the buckling coefficient which is a function of the loaded length to plate width ratio (s_s/b) and plate depth to width ratio (h/b), D is the flexural rigidity of the plate, and b is the width of the plate as shown in Figure 2.3.

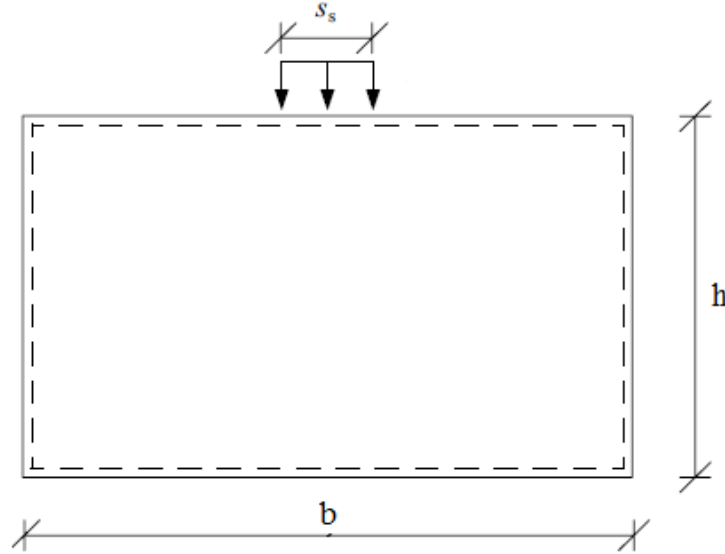


Figure 2.3: Plate model used by Zetlin (1955)

Through experimental testing of nine plates, Zetlin provided buckling coefficient curves that incorporated the plate thicknesses, w , and the s_s/b ratios. However, these curves were only applicable to simply supported plates.

Khan and Johns (1975) also investigated the buckling behaviour of simply supported plates subjected to patch loading and they proposed the critical buckling equation shown in Equation [2.3]. This equation differs from the equation proposed by Zetlin (1955) because the expression is divided by the plate height (h). Khan and Johns observed that the ratio of the loaded length to plate the height (s_s/h) has a greater influence on the buckling coefficient than the ratio of the loaded length to plate width (s_s/b). Thus the buckling coefficient was expressed as a function of s_s/h and the plate aspect ratio (b/h). As the loaded length to plate height ratio increased, the buckling coefficient also increased.

$$P_{cr} = k \frac{\pi^2 D}{h} \quad [2.3]$$

When the flexural rigidity is substituted into Equation [2.3], the classical elastic buckling load formula for plates subjected to patch loading is produced as shown in Equation [2.4], where w and h are the plate thickness and height respectively.

$$P_{cr} = k \frac{\pi^2 E}{12(1 - \nu^2)} \frac{w^3}{h} \quad [2.4]$$

Rockey and Bagchi (1968) extended the work on plates to the behaviour of webs of plate girders subjected to patch loading. Using the finite element method, they found that the presence of a flange not only prevents the web from rotating, but also aids in distributing the patch load to a longer portion of the web. This, in turn, results in a larger buckling coefficient for girder webs than for an equivalently sized simply supported plate.

A study by Lagerqvist (1994) concluded that the loaded length (s_s) depicted in Figure 2.4, had a negligible effect on the web buckling coefficient for I-shaped plate girders. This finding allowed Lagerqvist to propose a simplified equation for the critical buckling coefficient (k_F) of web plates subjected to patch loading, shown in Equation [2.5]. In addition, Lagerqvist showed that a constant value may be used to account for the flange restraining effect on the web buckling behaviour. Equation [2.5] was incorporated into Eurocode 3 Part1-5: Design of Steel Structures (EN 1993 1-5, 2006).

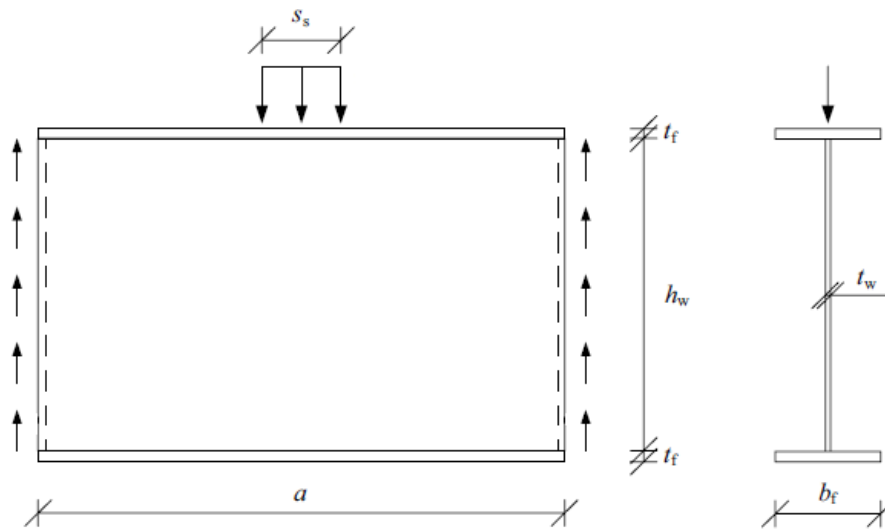


Figure 2.4: Plate girder subjected to patch loading (Lagerqvist 1994)

$$k_F = 5.5 + 2.1 \left(\frac{h_w}{a} \right)^2 \quad [2.5]$$

Shahabian and Roberts (1999) applied a numerical modelling technique to study the elastic critical buckling coefficient for slender girder webs subjected to a combination of patch loading and in-plane bending. The buckling coefficient for the combined loading condition was presented in a relationship with the individual buckling coefficients of the respective applied loads. One such expression is reproduced in Equation [2.6].

$$\left(\frac{k_{pb}}{k_p} \right)^\alpha + \left(\frac{k_{pb}}{k_b} \right)^\alpha = 1.0 \quad [2.6]$$

where k_{pb} is the buckling coefficient for combined patch loading and bending,
 k_p is the buckling coefficient for patch loading,
 k_b is the buckling coefficient for bending,
 α is the numerical factor based on the height to thickness of the web.

Graciano and Lagerqvist (2003) performed numerical analyses on longitudinally stiffened I-shaped plate girders subjected to patch loading. They proposed Equation [2.7] to determine the buckling coefficient (k_{cr}). This buckling coefficient accounts for the web restraining effects of the flanges by the term β , which was defined as a measure of torsional stiffness provided to the web from the flange.

$$k_{cr} = 5.82 + 2.1 \left(\frac{h_w}{a} \right)^2 + 0.46^4 \sqrt{\beta} \quad [2.7]$$

When β is small, the effect of the flange on the web is small and thus the web plate behaves as a simply supported plate. When β is very large, the web behaviour approaches that of a fully clamped plate. For situations in between, β can be calculated by Equation [2.8].

$$\beta = \frac{b_f t_f^3}{h_w t_w^3} \quad [2.8]$$

2.3 Inelastic Behaviour of Steel Plates and Girder Webs Subjected to Patch Loading

The inelastic behaviour and strength of steel plates was first investigated by Timoshenko (1961) where he showed that thin plates under full uniform edge loading can carry greater loads than the critical buckling load. This reserve is called post buckling strength and can be developed in slender plates where redistribution of stresses in the plate is possible. To account for this phenomenon, an effective width method, where only edge strips are effective in resisting load and the central portion is ineffective (see Figure 2.5), was developed by Timoshenko (1961). He provided an equation for calculating the effective width (c) which was determined to be a function of the plate thickness (w) and was independent of the plate width (b). The ultimate load, given by Equation [2.9], can then be determined assuming that the edge strips reach the yield stress of the plate.

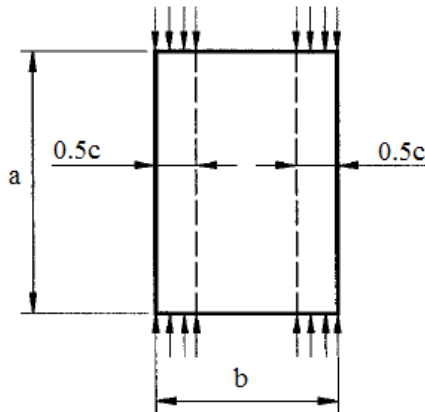


Figure 2.5: Equivalent edge strips effective in resisting load after critical buckling load levels (Timoshenko, 1961)

$$P_u = cw\sigma_{cr} = \frac{\pi w^2}{\sqrt{3(1-\nu^2)}} \sqrt{E\sigma_y} \quad [2.9]$$

where P_u is the ultimate compressive load resistance and σ_{cr} is the critical elastic buckling stress.

The work on inelastic behaviour of plates extended to webs of I-shaped plate girders subjected to patch loading. For plate girder webs of varying slenderness, studies have

identified three failure modes within the inelastic buckling regime (Paik & Thayamballi, 2003). These failure modes are shown in Figure 2.6. The first failure mode is web yielding where the web yields in a location near the loaded flange. The second mode is crippling, which causes a small buckle or ripple of the web adjacent to the loaded flange. Lastly, the third failure mode is web panel buckling, which consists of the web buckling out-of-plane between flanges and stiffeners. Generally, stocky webs fail by yielding and more slender webs fail by either crippling or web panel buckling (Gozzi, 2007).

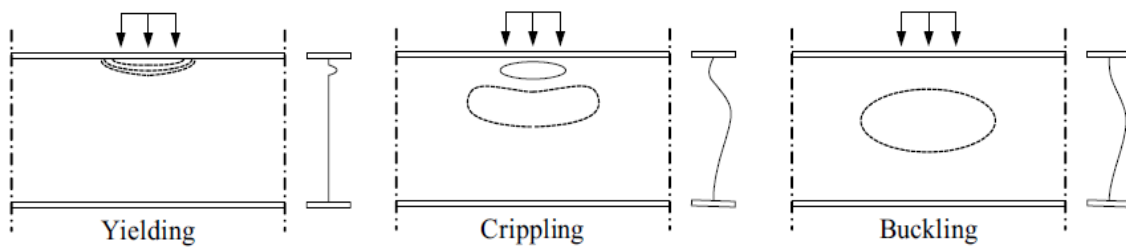


Figure 2.6: Three prominent failure modes for girders subjected to patch loading (Gozzi, 2007)

The presence of structural, geometric, and material imperfections in realistic plates causes certain locations through the thickness of a plate to begin yielding prior to other locations. This weakening effect causes inelastic buckling and results in the reduction of the ultimate load of the plate (Tupula Yamba, 1981).

Bergfelt (1971) performed over 100 tests on plate girders and proposed Equation [2.10] where the web thickness, t_w , was shown to be the main contributor for the yielding resistance of the web. The effect of the flange thickness, t_f , was also included in the equation.

$$P_u = 0.045Et_w^2 \left(0.55 + 0.22 \frac{t_f}{t_w} \right) \quad [2.10]$$

El-gaaly (1983) agreed that the ultimate patch load resistance, P_u in Equations [2.10] and [2.11], is largely dependent on the square of the web thickness and less dependent on the loaded length. The equation that he proposed shared a similar form to Equation [2.10] but El-gaaly incorporated the yield strength of the web steel, f_{yw} , in the web resistance calculation.

$$P_u = 0.5t_w^2 \sqrt{E f_{yw} \frac{t_f}{t_w}} \quad [2.11]$$

A plastic collapse mechanism was proposed by Roberts and Rockey (1979) and was later modified by Roberts (1981). The failure mechanism procedure was developed to predict either web crippling or web yielding. A schematic presented by Tang (2005) of the two failure mechanisms is shown in Figure 2.7 for the case of interior patch loading. As the applied patch load was increased, plastic hinges formed in the loaded flange concurrent with the formation of yield lines in the web near the loaded flange.

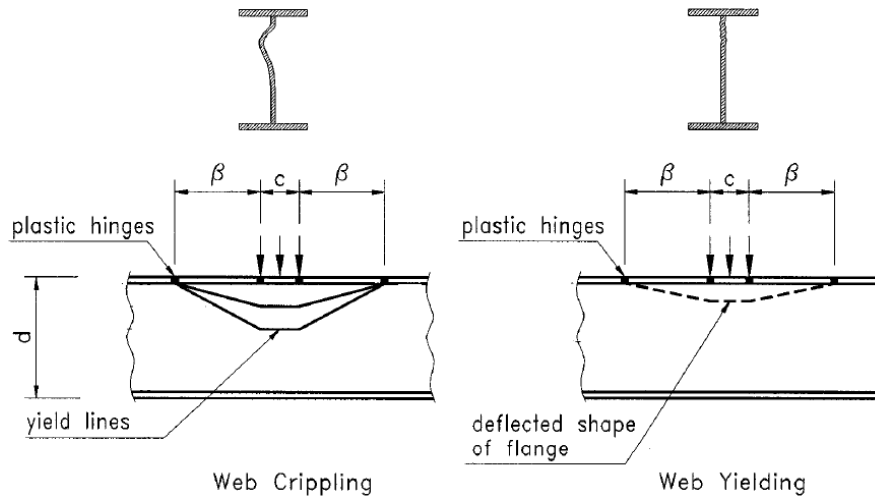


Figure 2.7: Schematic of web crippling and web yielding adapted from Tang (2005)

In the case of web crippling, yield lines were observed on the webs of the slender test girders in the region where the web deflected laterally and plastic hinges were observed on the flanges. Plastic hinges were also observed on the flanges of stockier test specimens that failed by web yielding, however, the magnitude of flange deflection was greater for girders that failed by web crippling than those that failed by web yielding.

Roberts and Newark (1997) proposed closed form solutions for the web crippling and web yielding mechanisms specific to interior patch loading and they are expressed as Equations [2.12] and [2.13] respectively. This work was based on the analysis of 168 I-shaped girders previously studied by other researchers and was used to modify the

mechanism equations initially proposed by Roberts and Rockey (1979).

$$P_{uc} = \left[1.1t_w^2(E\sigma_w)^{0.5} \left(\frac{t_f}{t_w} \right)^{0.25} \left(1 + \frac{c_e t_w}{d_w t_f} \right) \right] \frac{1}{F} \quad [2.12]$$

$$P_{uy} = (16M_f \sigma_w t_w)^{0.5} + \sigma_w t_w c_e \quad [2.13]$$

where

P_{uc} = ultimate collapse (crippling) load,	M_f = plastic moment of the flange,
P_{uy} = ultimate yield load,	d_w = girder depth,
t_w = web thickness,	c_e = effective patch load length,
t_f = flange thickness,	F = factor of safety.
σ_w = web yield stress,	

It should be noted that c_e is equal to the length of the patch load plus two flange thicknesses to account for a 45° load distribution through the loaded flange. A limiting value of $c_e/d_w \leq 0.2$ in Equation [2.12] was recommended so that the mechanism would correspond to test data. Further, it was recommended that F be taken as 1.45 in Equation [2.12]. A factor of safety is not required in Equation [2.13] because the equation was found to produce overly conservative results. Lastly, the effect of vertical stiffeners was determined to confine the spread of plastic hinges in the loaded flange (Roberts & Newark, 1997).

Lagerqvist (1994) slightly modified the plastic collapse mechanism originally proposed by Roberts and Rockey (1979) to include a portion of the web in resisting load between the inner plastic hinges whereas Roberts and Rockey only considered the loaded flange as effective. Lagerqvist then proposed a design procedure to calculate the patch load resistance of a plate girder where the patch load resistance, (F_R), is expressed as the product of the yield strength of the web (F_y), and a reduction function ($\chi(\lambda)$), as shown in Equation [2.14].

$$F_R = F_y \chi(\lambda) \quad [2.14]$$

The yield strength of the web is calculated by Equation [2.15].

$$F_y = f_{yw} t_w (s_s + 2t_f) \sqrt{\left[\frac{f_{yf} b_f}{f_{yw} t_w} + 0.02 \left(\frac{h_w}{t_f} \right)^2 \right]} \quad [2.15]$$

where f_{yw} and f_{yf} are the material yield stresses for the web and flanges respectively, t_f and b_f represent the thickness and width of the flanges respectively, h_w is the web height, and s_s is the length of the patch load.

Given by Equation [2.16], the reduction function $\chi(\lambda)$, was calibrated by Lagerqvist (1994) from 190 tests where the moment capacity utilization (i.e., the ratio of applied moment to the ultimate moment capacity) of the girder was less than 40%.

$$\chi(\lambda) = 0.06 + \frac{0.47}{\lambda} \leq 1.0 \quad [2.16]$$

The reduction factor is dependent upon the relationship between the yield strength and the critical buckling resistance as shown by Equation [2.17].

$$\lambda = \sqrt{\frac{F_y}{F_{cr}}} \quad [2.17]$$

where the critical buckling resistance, F_{cr} , is calculated by:

$$F_{cr} = k_F \frac{\pi^2 E}{12(1 - \nu^2)} \frac{t_w^3}{h_w} \quad [2.18]$$

and k_F is the buckling coefficient for patch loading calculated by Equation [2.5].

Johansson et al. (2001) modified the work by Lagerqvist (1994) (Equations [2.14-2.18]) to include an effective loaded length parameter (l_y). This parameter incorporates how the patch load is physically applied to the flange (i.e., by a bearing plate, roller, etc.) and how the load travels and spreads through the flange and into the web. The equation for the effective loaded length, as it appears in Eurocode 3 (2006), as well as modified forms of Equations [2.5, 2.14-2.18] that were adopted into Eurocode 3, are presented in section 2.5. The effect of vertical stiffener spacing on the capacity of girder webs subjected to patch loading was investigated by Chacón et al. (2013). They performed 63 numerical studies on one web panel, varying the aspect ratio (from 1 to 3) and the loaded length. It was

determined that the design procedure proposed by Lagerqvist (1994) underestimated the resistance of the web under patch loading when the spacing of the transverse stiffeners is small.

Granath and Lagerqvist (1999) performed experimental and numerical testing on three plate girder specimens to study the deformation behaviour of web plates due to repetitive patch loading. They investigated the case where permanent deformations are created in a girder during the first patch load application then then the cross section is subjected to the same patch load (for example, a girder passing over subsequent supports during launching). In this case, subsequent patch loads have the same magnitude as the previous load but the geometric properties are different. Part of this research compared the behaviour of linear elastic girder finite element models to elastic-plastic simulations. The elastic models were shown to produce results that can be described as web panel buckling. The elastic-plastic simulations allowed for partial yielding of the web plate and the results showed the collapse mechanism categorized as web crippling. The authors showed that the linear elastic models predicted panel buckling at lower load levels than those that caused web crippling (for non-stocky girders). In practice, designers are usually concerned with the lowest load level that will cause failure either by buckling or yielding of a combination of the two. The three girder specimens tested and analyzed by Granath and Lagerqvist (1999) are presented in Figure 2.8.

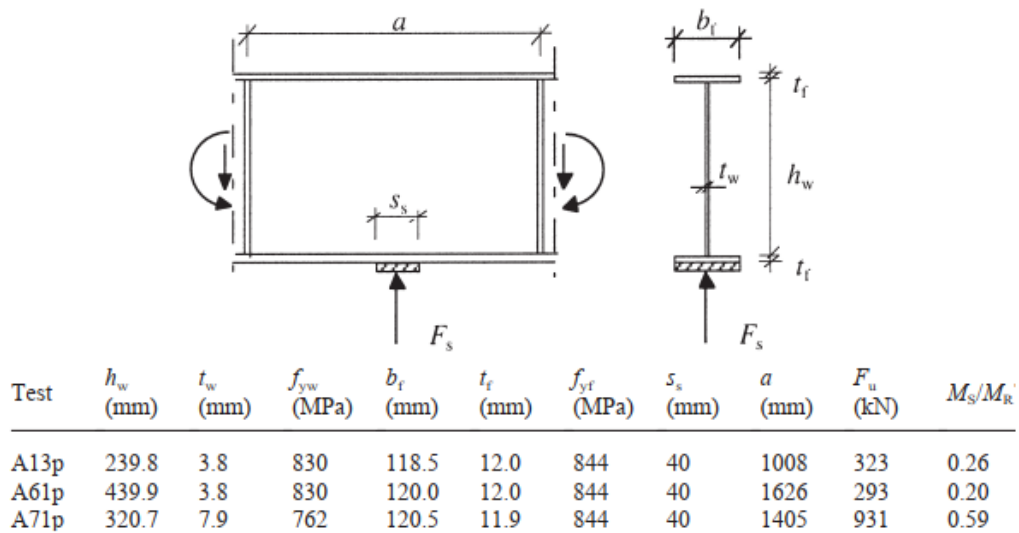


Figure 2.8: Specimens tested by Granath and Lagerqvist (1999)

Bedair (2015) presented a simplified expression for determining the web shear buckling coefficient for box sections accounting for the restraint provided by the flanges. Current design codes assume simply supported webs as boundary conditions when the real degree of restraint exists somewhere between a simply supported and fully fixed condition. Bedair (2015) showed that the critical shear buckling stress increased as the ratio of flange to web thickness (t_f/t_w) approached 2. It appears that Bedair (2015) did not test specimens with t_f/t_w ratios larger than 2. It should be noted that in typical box girders, the t_f/t_w ratios commonly exceed 2.

2.4 Girders Subjected to Loading Combinations

In this section, a summary of the available literature on girder webs subjected to combinations of patch loading, shear force, and bending moment is presented. During launching, and during the service life of a bridge, all three load effects are often present at the same time. The behaviour of the web is affected by the magnitude of each load effect acting in combination.

2.4.1 Girders Subjected to Combined Patch Loading and Shear

El-gaaly (1975) performed twenty tests on thin web panels consisting of thicknesses from 1.2 mm to 2.6 mm subjected to patch load, shear force, and combinations of the two. By testing the pure patch load and pure shear load cases independently, El-gaaly was able to observe the reduction in capacity when the load cases were combined. The interaction proposed by El-gaaly (1975) is shown in Equation [2.19] as:

$$\left(\frac{P_u}{P_{u0}}\right)^{1.8} + \left(\frac{Q_u}{Q_{u0}}\right)^{1.8} = 1.0 \quad [2.19]$$

where P_u is the ultimate patch load in the presence of shear force, P_{u0} is the ultimate patch load in the absence of shear force, Q_u is the ultimate shear force in the presence of patch loading, and Q_{u0} is the ultimate shear force in the absence of patch load. These values were obtained experimentally.

Graciano and Ayestarán (2013) presented the work of Zoetemeijer (1980) who tested rolled European I-beam sections by applying a patch load while introducing shear stresses separately. He found that the shear force developed from an applied patch load (P), has no influence on the patch loading resistance. Zoetemeijer then proposed the relationship, shown in Equation [2.20] below, to describe the interaction where the applied shear force (V) is an external force and not a result of the applied patch load. The shear resistance (V_R) was calculated by the 1980 Swedish Design Standards.

$$\left(\frac{P}{P_R}\right)^2 + \left(\frac{V}{V_R}\right)^2 \leq 1.0 \quad [2.20]$$

Shahabian and Roberts (2001) conducted twenty-four tests on stiffened I-shaped plate girders subjected to pure patch loading, pure shear loading, and the combination of patch load and in-plane shear. The girders were simply supported and the set up was such that the patch load was applied to a flange at the middle of the web panel, and the shear force was applied to the end of the web panel. The panel aspect ratios were varied from 1 to 2 and the flange thicknesses were also varied. The tested girders were 1500 mm to 2300 mm in length. Based on the test results, the following interaction equation was proposed and was shown to fit the data better than Equation [2.20] (Shahabian & Roberts, 2001).

$$\left(\frac{P}{P_u}\right) + \left(\frac{V}{V_u}\right)^2 \leq 1.0 \quad [2.21]$$

where P and V are the applied patch and shear loads respectively,
 P_u is the patch load resistance of the plate girder,
 V_u is the shear resistance given by Equation [2.22].

$$V_u = \tau_{cr}d_w t_w + \sigma_t^y \sin^2 \theta (d_w \cot \theta - b_w) + 4d_w t_w \sin \theta \sqrt{(\sigma_{ow} M_p^* \sigma_t^y)} \quad [2.22]$$

In Equation [2.22]:

τ_{cr} = critical shear buckling strength of a simply supported web,
 d_w = web depth,
 t_w = web thickness,
 b_w = web width,

σ_t^y = web tension field membrane stress,
 σ_{ow} = web yield stress,
 M_p^* = nondimensional flange strength parameter,
 θ = inclination of the web tension field.

A large number of numerical simulations were performed by Kuhlmann and Braun (2007)

to extend the interaction of Equation [2.21] such that it would be applicable for a larger range of I-shaped girder geometries. The authors proposed Equation [2.23].

$$\left(\frac{P}{P_R}\right) + \left(\frac{V}{V_R}\right)^{1.6} \leq 1.0 \quad [2.23]$$

Graciano and Ayestarán (2013) plotted Equations [2.20], [2.21], and [2.23] shown in Figure 2.9. The authors noted that the three equations were not developed to account for the effect of bending moment. Interestingly, although it was intended to cover the largest range of girder geometries the equation proposed by Kuhlmann and Braun (2007) is the least conservative.

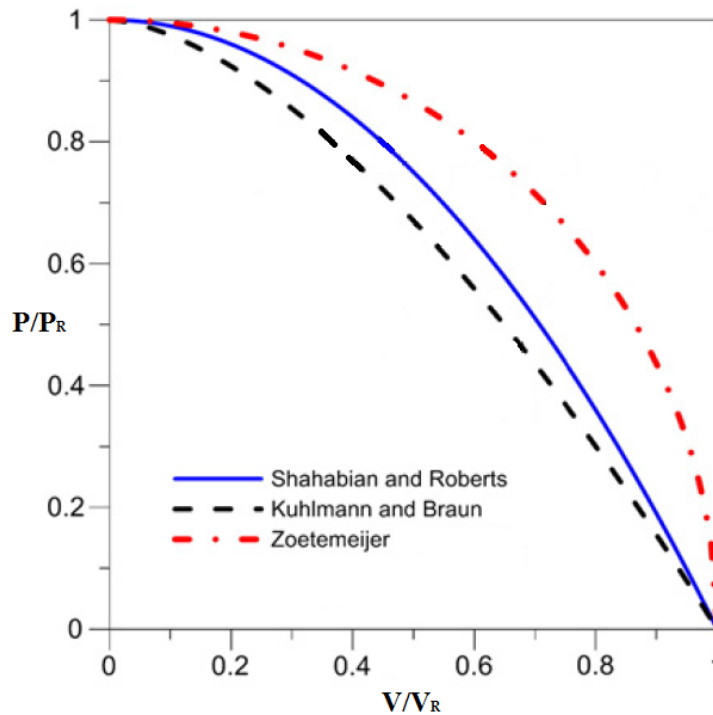


Figure 2.9: Interaction between shear and patch loading adapted from Graciano and Ayestarán, 2013

2.4.2 Girders Subjected to Combined Patch Loading and Bending

Previous research on this subject has shown that the patch load resistance of I-shaped plate girder webs is reduced when a bending moment is also present (Rockey & El-gaaly, 1973; Roberts, 1983; Shimizu, 1994; Lagerqvist and Johansson, 1996; Graciano and Casanova, 2004; and others). Consider a girder where a patch load is applied through the bottom

flange, and it is also subjected to negative bending. The bottom flange and lower region of the web experience compressive stresses in two directions. This state of stress can cause the girder to fail at a lower load level than the state of stress produced from a pure patch loading scenario.

One of the first major studies investigating the effect of combined patch loading and bending moment was undertaken by Rockey and El-gaaly (1973). A series of experimental tests were performed on thin-walled trapezoidal beams featuring web thicknesses of 1.2 mm to 2.6 mm and a constant depth of 305 mm. The span of all tested girders was 4570 mm. It was found that for moment utilization ratios of less than 50%, no significant reduction in patch load resistance was observed. It is noted that other authors such as Bossert and Ostapenko (1967) and Johansson et al. (2001) have arrived at a similar conclusion. The interaction proposed by Rockey and El-gaaly (1973) is expressed as:

$$\left(\frac{P}{P_R}\right)^3 + \left(\frac{M}{M_R}\right)^3 = 1.0 \quad [2.24]$$

where P and M are the applied patch load and bending moment respectively, and P_R and M_R are the patch load and moment resistances respectively. In this study, only a constant aspect ratio was tested and thus the authors mention the need to further expand this study (Rockey & El-gaaly, 1973).

Roberts (1983) proposed a reduction factor on the patch loading resistance to account for the effect of bending moment. The reduction factor, R_b , is intended to be applied to the lesser of the values calculated from Equations [2.12] for web crippling and [2.13] for web yielding to obtain the final resistance. The factor is calculated as shown in Equation [2.25], where σ_w is the web yield stress, and σ_b is the applied bending stress.

$$R_b = \left(1 - \sqrt{\frac{\sigma_b^2}{\sigma_w^2}}\right) \quad [2.25]$$

Shimizu (1994) performed a finite element study of nine I-shaped plate girders with longitudinal stiffeners to determine the effect of a longitudinal stiffener on the web resistance when subjected to the combination of patch load and bending. In the numerical study, three levels of bending stress to shear stress (caused by patch loading) ratios ($\sigma/\tau = 0, 4.1, 7.3$) were considered. He found that the presence of bending moment changes the formation of yield lines in the plastic collapse mechanism presented by Lagerqvist (1994). However, the predicted capacities from the plastic collapse mechanism remained conservative. Furthermore, although the presence of a longitudinal stiffener works to restrict the out-of-plane deflection of the web and thus increase the web resistance to pure patch loading, its effect on increasing the patch load resistance when bending is present is small (Shimizu, 1994). This effect was confirmed by Graciano (2015) who presented work done by Davine (2005) and showed that the presence of a longitudinal stiffener near the loaded flange increases the patch load resistance. However, the critical buckling load increases as the longitudinal stiffener is placed further away from the loaded flange, up to a certain extent, dependent on the cross-sectional properties of the girder.

Lagerqvist and Johansson (1996) compiled data from 250 patch load tests in the available literature (both stiffened and unstiffened girders) and arrived at two interaction equations. The first equation applies to welded girders as shown in Equation [2.26]. This interaction equation is shown as the solid line in Figure 2.10 along with the test data points for welded girders. In this equation, F_u and M_S are the applied patch load and bending moment respectively. A second interaction equation was developed for rolled beams; however, it is not presented in this thesis because it does not apply to plate girders. Both equations were validated for aspect ratios of $a/h \geq 1$ as well as $M_S/M_R \leq 0.4$.

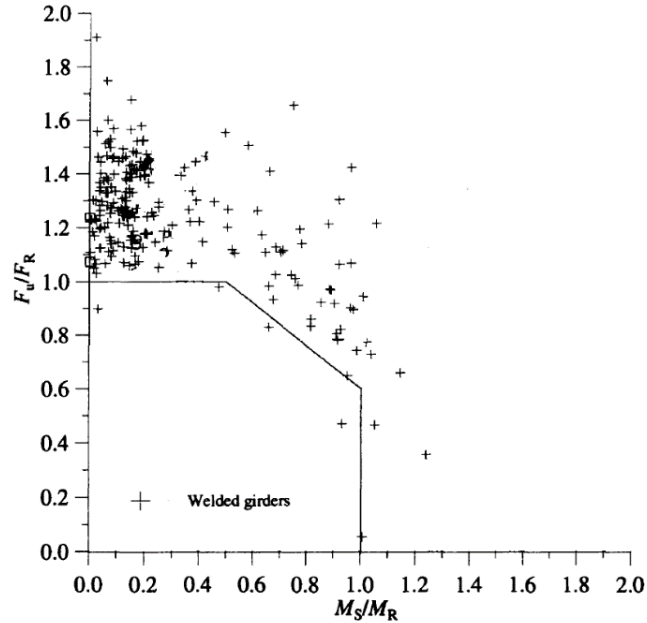


Figure 2.10: Interaction between patch load and bending moment proposed by Lagerqvist and Johansson (1996)

$$\frac{F_u}{F_R} + 0.8 \left(\frac{M_S}{M_R} \right) = 1.4 \quad [2.26]$$

Graciano and Casanova (2005) further studied the interaction between patch loading and bending moment with the presence of a longitudinal web stiffener. In their numerical study, the magnitude of applied bending moment varied such that the utilization also varied from 0.19 to 0.9. In addition, the location of the longitudinal stiffener and the loaded length was varied. It was concluded that the optimum position of the longitudinal stiffener is influenced by the loaded length and the loaded flange size. For moment utilizations of 60% or less, the longitudinal stiffener is best placed at a height of $0.2h_w$ from the loaded flange. For moment utilizations greater than 60%, the optimum location of the stiffener is $0.2h_w$ to $0.25h_w$ from the loaded flange. The authors noted that for moment utilizations of 90% or greater, the stiffener is deemed ineffective regardless of its location. This was found to be consistent with the work of Shimizu (1994) presented earlier.

Kovacevic et al. (2021) conducted a parametric study on the patch load resistance of unstiffened and longitudinally stiffened crane rail support plate girders. The research investigated the effect of geometric imperfections on the capacity of the cross section. The

parametric study showed that the patch load resistance of unstiffened and longitudinally stiffened plate girders increases as the length of the patch load increases regardless of the magnitude of the initial geometric imperfection. Kovacevic et al. (2021) observed that the effect of the longitudinal stiffener on increasing the patch load resistance is negligible when the ratio of patch load length (s_s) to web height (h_w) is less than 0.15. In most cases, girders that are erected via the launching method have s_s/h_w ratios of less than 0.15 indicating that the addition of longitudinal stiffeners for launched girders is not very effective. However, in the case of crane rail beams, which was the inspiration of the work by Kovacevic et al., the ratio is commonly greater than 0.15. This research also showed that the unfavourable shape of the initial geometric imperfections resembles the deformation of the cross section once buckling has occurred at the lowest eigenvalue state.

A study to predict the critical buckling load of unstiffened webs under the interaction of patch loading and bending moment was undertaken by Maiorana et al. (2008). Linear buckling analyses were carried out on plates of widths ranging from 2750 mm to 5750 mm, thicknesses of 10 mm to 14 mm, and heights of 1500 mm to 3800 mm. The patch load level and the magnitude of linear compressive stress (due to in-plane bending) were also varied. The results produced the following prediction for the critical buckling load:

$$F_{cr} = \left[3.2048 \frac{\pi^2 E}{12(1 - \nu^2)} \right] \frac{t^3 c_1}{h c_2 c_3} \quad [2.27]$$

where c_1 represents the effect of the web height to web panel width, c_2 represents the effect of the loaded length to the web panel width, and c_3 represents the distribution of the bending stress on the cross section. The functions c_1 , c_2 , and c_3 are presented in the paper by Maiorana et al. (2008). Interestingly, the authors do not specifically include the effect of varying flange dimensions in their study. However, they do use Equation [2.27] to assess the web buckling capacity of I-shaped girders.

2.4.3 Girders Subjected to Combined Patch Loading, Shear, and Bending

The interaction relating the combination of patch load, shear, and bending had not been

studied until the mid-1990s. An interaction correlating all three load effects was first proposed by Takimoto (1994). He performed a numerical analysis on 143 plate girders available in the literature and proposed Equation [2.28] (Paik & Thayamballi, 2003).

$$\left(\frac{P}{P_R}\right)^4 + \left(\frac{M}{M_R}\right)^4 + \left(\frac{V}{V_R}\right)^4 = 1.0 \quad [2.28]$$

Shahabian and Roberts (2001) proposed an interaction formula relating the combination of patch loading, shear, and bending moment. By integrating proposed interaction equations for patch loading combined with bending, and patch loading combined with shear found in the literature, the authors proposed the following interaction formula.

$$[M_n V_n (M_n^4 + V_n^4 - 1) + M_n P_n (M_n^2 + P_n^2 - 1) + V_n P_n (V_n^2 + P_n - 1) + 2M_n V_n P_n] \leq 0 \quad [2.29]$$

In this equation, M_n , V_n , and P_n are the moment, shear, and patch load utilizations respectively. It should be noted that this equation is a surface in three dimensions. If one of the three load effects is not present, the interaction remains plane and is still valid (Shahabian and Roberts, 2001). This interaction equation was verified through testing of three simply supported I-shaped plate girders containing three web panels with dimensions of 600 mm in height and 705 mm in panel width. Based on the limited amount of verification work performed, the authors stated that Equation [2.29] is valid for aspect ratios of 1 to 2 and moment utilization ratios of 0 to 50%. The authors recommend that a wider range of experimental and numerical tests be performed to further verify Equation [2.29].

More recently, Braun and Kuhlmann (2010) presented the simplified interaction equation presented below. In Equation [2.30] the patch load resistance, plastic moment resistance, and shear resistance are all calculated from Eurocode 3 Part 1-5.

$$\left(\frac{P}{P_R}\right) + \left(\frac{M}{M_R}\right)^{3.6} + \left(\frac{V - 0.5P}{V_R}\right)^{1.6} \leq 1.0 \quad [2.30]$$

A numerical study was conducted by Graciano and Ayestarán (2013) to build upon the studies of Shahabian and Roberts (2001) and Braun and Kuhlmann (2010). In this study, approximately 80 numerical simulations were performed on I-shaped plate girders by altering the load levels of patch load, shear, and bending moment. It was concluded that a greater reduction in resistance results once the moment utilization exceeds 60% and that the presence of bending has a more profound negative affect on the resistance of the girder than the presence of shear. Further, the authors stated that the equation proposed by Shahabian and Roberts (Equation [2.29]) is conservative while the interaction by Braun and Kuhlmann (Equation [2.30]) fits the test data well.

2.5 General Code Requirements

The major bridge design codes in Canada, the United States of America, and Europe have been studied and relevant information pertaining to the design of girder webs subjected to patch loading, and/or combinations of patch loading with shear or bending moment is presented in this section.

2.5.1 Canadian Highway Bridge Design Code

The CHBDC (CSA, 2019) addresses ‘web bearing resistance’ through two equations that account for web yielding and web crippling. The web bearing resistance, for loads applied at a distance from the end of the girder that is greater than the depth of the girder, is calculated from the lesser of Equations [2.31] and [2.32], which address web yielding and web crippling respectively.

$$B_r = \Phi_{bi}w(N + 10t)F_y \quad [2.31]$$

$$B_r = 1.45\Phi_{bi}w^2\sqrt{F_yE_s} \quad [2.32]$$

In both equations, Φ_{bi} is a resistance factor equal to 0.8, w is the web thickness, N is the length of bearing, t is the thickness of the loaded flange, F_y is the yield stress of the steel, and E_s is the modulus of elasticity for steel. Semi-empirical in nature, the equations were calibrated using test data by Kennedy et al. (1997). For web crippling resistance, the web

thickness is the only geometric property explicitly included in the equation. The effect of other parameters on the bearing capacity such as the length of the patch load and the flange thickness are collectively considered using a coefficient of 1.45.

2.5.2 AASHTO Bridge Design Specifications

The AASHTO Bridge Design Specification (2015) code for bridge design addresses ‘concentrated loads applied to webs without bearing stiffeners’ through two equations that account for web yielding and crippling, similar to the CHBDC. For interior loads, the resistance to web yielding, R_u , is given as:

$$R_u = \Phi_b(5k + N)F_{yw}t_w \quad [2.33]$$

where Φ_b is a resistance factor, t_w is the web thickness, N is the length of bearing, k is the distance from the outer face of the loaded flange to the web toe of the fillet weld, and F_{yw} is the yield stress of the web.

The resistance to web crippling is calculated by:

$$R_u = \Phi_b 0.8t_w^2 \left[1 + 3 \left(\frac{N}{d} \right) \left(\frac{t_w}{t_f} \right)^{1.5} \right] \sqrt{\frac{EF_{yw}t_f}{t_w}} \quad [2.34]$$

where d is the depth of the girder, t_f is the thickness of the loaded flange and E is the modulus of elasticity for steel. This equation reflects the design philosophy of Roberts and Newark (1997).

2.5.3 Eurocode 3 Part 1-5 Design of Plated Structures

The effects of web yielding and crippling were treated separately in previous versions of Eurocode 3. However, based on work by Johansson et al. (2001), the two design checks were merged with a local web buckling check and now appear together in one design section (EN 1993-1-5, 2006). The design procedure for resistance to transverse forces is presented in the following equations. The main difference between the way the procedure is presented in Eurocode 3 and the original proposal (Equations [2.14 - 2.18]), is that the function relating the critical buckling load to the yield load is now applied to the loaded length (l_y) as opposed to the yield resistance.

The resistance to transverse loading is given as Equation [2.35] where γ_{M1} is a reduction factor equal to 1.1, f_{yw} is the yield stress of the web, and t_w is the web thickness.

$$F_R = \frac{f_{yw}L_{eff}t_w}{\gamma_{M1}} \quad [2.35]$$

The function (χ_F) is then applied to the loaded length (l_y) to obtain a modified effective length (L_{eff}) given by:

$$L_{eff} = \chi_F l_y \quad [2.36]$$

where χ_F and l_y are given by Equations [2.37] and [2.38] respectively.

$$\chi_F = \frac{0.5}{\bar{\lambda}_F} \leq 1.0 \quad [2.37]$$

$$l_y = s_s + 2t_f(1 + \sqrt{m_1 + m_2}) \leq a \quad [2.38]$$

In Equation [2.38], s_s is the patch load length, t_f is the flange thickness and m_1 and m_2 are constants defined by Equations [2.39] and [2.40] respectively. A limit of the panel width (a) is placed on the loaded length to ensure that the calculated panel resistance is limited to the physically loaded web panel.

$$m_1 = \frac{f_{yf}b_f}{f_{yw}t_w} \quad [2.39]$$

$$m_2 = 0.02 \left(\frac{h_w}{t_f} \right)^2 \quad \text{if } \bar{\lambda}_F < 0.5, \quad \text{otherwise } m_2 = 0 \quad [2.40]$$

The function (χ_F) is dependent on the slenderness parameter given by Equation [2.41].

$$\bar{\lambda}_F = \sqrt{\frac{l_y t_w f_{yw}}{F_{cr}}} \quad [2.41]$$

The slenderness parameter ($\bar{\lambda}_F$) is dependent upon the loaded length (l_y), the web thickness (t_w), the yield stress of the web (f_{yw}), and the elastic critical buckling resistance (F_{cr}) expressed as:

$$F_{cr} = 0.9k_F E \frac{t_w^3}{h_w} \quad [2.42]$$

where E is the modulus of elasticity and h_w is the web height. The buckling coefficient (k_F) is dependent on the loading arrangement as shown in Figure 2.11, the web height (h_w), and the panel width (a).

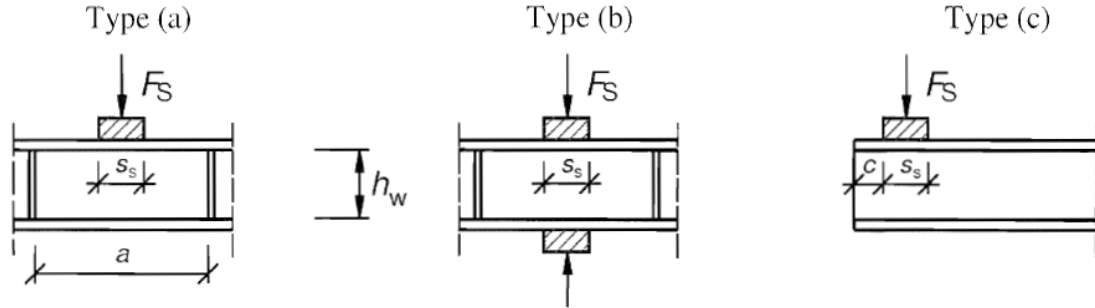


Figure 2.11: Transverse loading arrangements corresponding to specific k_F values. Adapted from Eurocode 3 (EN 1993 1-5, 2006)

For the purposes of this thesis, the patch load is applied through one flange and therefore k_F is calculated by Equation [2.43] which corresponds to Type (a) in Figure 2.11.

$$k_F = 6 + 2 \left(\frac{h_w}{a} \right)^2 \quad [2.43]$$

Equation [2.26], which accounts for the combined action of patch loading and bending moment, is a required Eurocode 3 check. The interaction must be calculated when the moment utilization is greater than 50% (Johansson et al, 2001). It is important to note that the interaction equation has not been verified for box girders and, to date, is only valid for I-shaped plate girders (Guide to Eurocode 3, 2010).

2.5.4 Commonalities among the Design Codes

All three codes require the use of finite element software when a particular design parameter exceeds code specified limits. However, details on the type of analysis to perform and the extent to which geometric imperfections should be included in the analysis is vague and is left to the discretion of the design engineer.

A maximum depth to thickness ratio for girder webs is specified in all three design codes to prevent web breathing. Web breathing occurs when out-of-plane flexing of the web under repeated transverse loads (i.e., loading perpendicular to the longitudinal axis of the girder) causes fatigue cracks in the vicinity of the web-to-flange junction. In addition, all three design codes explicitly recommend that the effect of any transverse loading should be translated onto the plane of the web through the angle of inclination for inclined box girder webs.

2.6 Summary

As shown in the previous sections, a significant amount of research has been conducted to develop an understanding of plate and plate girder behaviour when subjected to patch loading or combinations of patch load with bending and/or shear. Although some of the research (Lagerqvist & Johansson, and Roberts et al. for example) has been incorporated and formatted for design code use, the proposed equations have not been verified for box girder geometries. Some researchers (Wolchuk, 1981) have expressed that equations developed for I-shaped plate girders cannot be directly applied to box girders.

The range of tested girders in the literature is relatively narrow in terms of girder cross-sectional geometry and girder span lengths. The majority of the literature in this area has focused on short span girders where the magnitude of normal stress due to bending is not representative of some practical applications (i.e., girder launching).

CHAPTER 3 EXPERIMENTAL PROGRAM

3.1 General

This experimental program was designed to obtain and monitor stress levels in the webs of steel box girders of the Shubenacadie River Bridge, during the girder launching phase of construction. Field data was collected during the months of January and February of 2014. The collected field data was intended to provide an understanding of the behaviour of box girder webs, in real time, during launching. The stress results were also used in an attempt to verify the finite element model developed in this study.

3.2 Existing Bridge Background and Site Features

The Shubenacadie River Bridges are located on NS-HWY 102 between exits 10 (Milford) and 11 (Stewiacke). The original bridges were constructed in 1975, with one bridge accommodating Halifax bound traffic and a separate bridge carrying Truro bound traffic. Significant deterioration of the bridge girders necessitated the replacement of the superstructures of both bridges whereas the existing piers were deemed to be structurally sufficient to accommodate the new superstructures. The Halifax bound structure was replaced first. The identical Truro bound structure was replaced after the completion of the Halifax bound structure. Figure 3.1 is a view of the Halifax bound structure during construction and Figure 3.2 is a satellite image of the bridge site which was taken during construction of the Truro bound structure. Both figures identify major features that are common to both the Halifax and Truro bound structures. Any reference to structural bridge components or to bridge construction activities herein are in relation to the Halifax bound structure only, as all field testing was performed on this structure.

The bridge superstructure consists of a four span, double steel box girder system, with a composite concrete deck. Figure 3.3 is a schematic plan and elevation view of the Halifax bound structure with both girders in their final condition. Girder 1 (the North girder) was launched first, followed by Girder 2 (the South girder). Both girders were constructed on the West approach and were launched toward the East abutment. As shown in Figure 3.3, the site features three permanent piers, as well as a temporary bent that was constructed

between piers 1 and 2. The temporary bent consisted of a truss platform supported by driven circular steel piles and was used to reduce the cantilevered span of the girders during launching, between piers 1 and 2.



Figure 3.1: Halifax bound structure during construction (north girder shown)

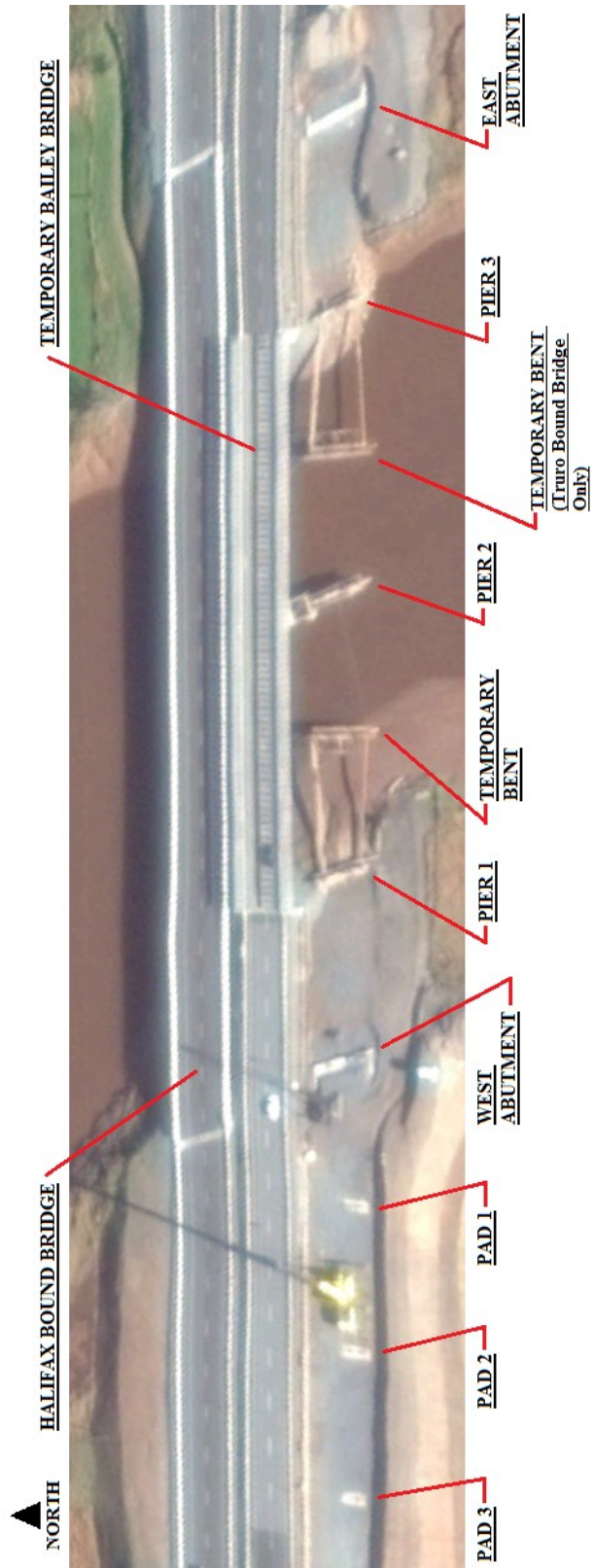


Figure 3.2: Satellite image of the Shubenacadie River Bridge construction site (Google Maps, 2015)

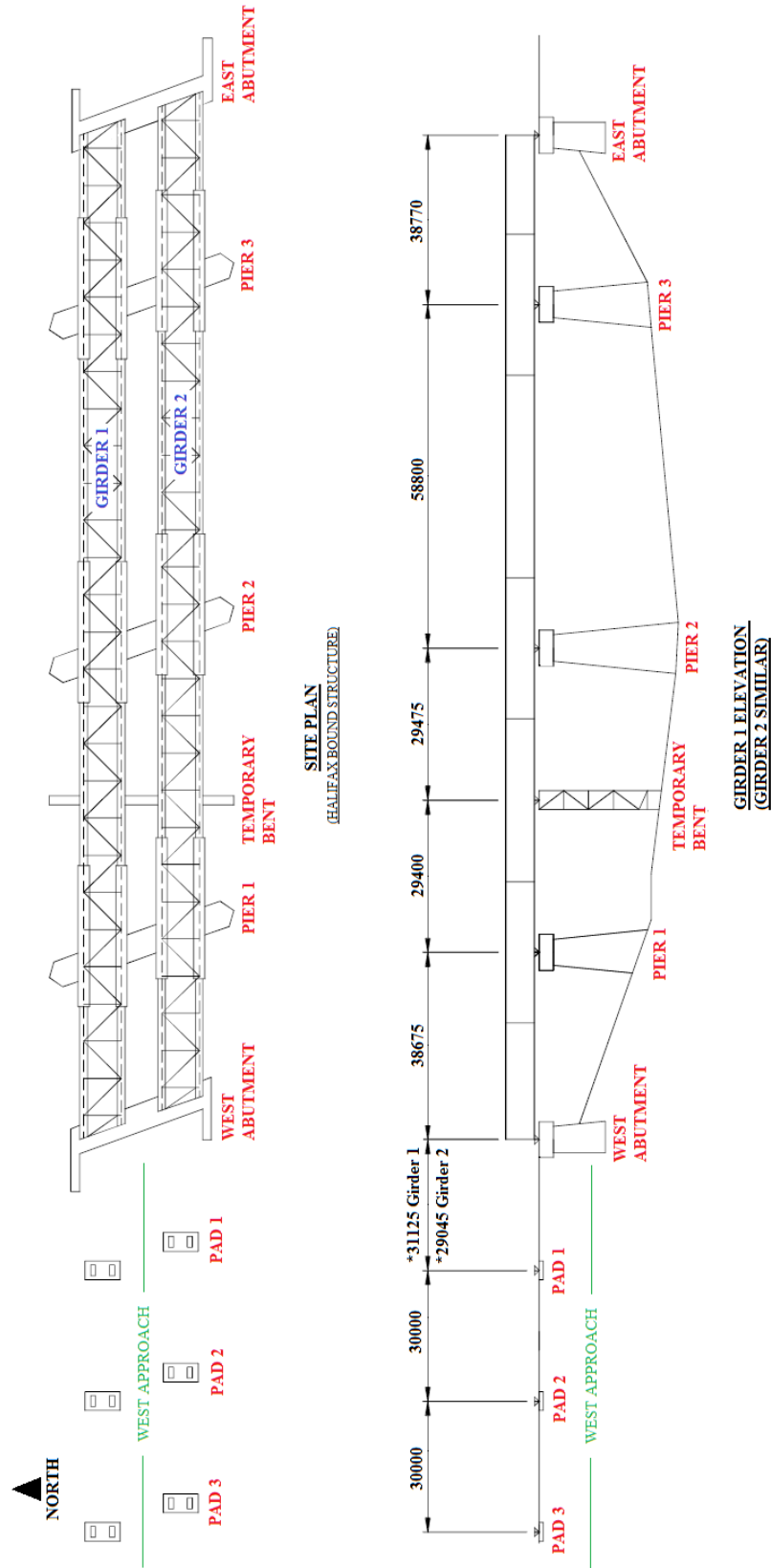


Figure 3.3: Schematic plan and elevation views of the Halifax bound bridge

3.3 Test Specimens

Field testing was conducted on both box girders of the Halifax bound structure. During construction, each girder was launched independently. All structural steel pertaining to the box girders, stiffeners, and diaphragms conformed to (CSA) G40.21M – 350WT, where WT indicates weldable notch-tough steel. All bracing and miscellaneous steel conformed to (CSA) G40.21M – 350W, where W indicates weldable steel.

Figure 3.4 is a cross-sectional view of a typical trapezoidal box girder. Nominal dimensions of the two tested sections are listed in Table 3.1. The dimensions of the two cross sections differ in top flange width and thickness, as well as bottom flange thickness. Note that the geometry of the flanges (i.e., width and thickness) change along the length of each girder to accommodate varying levels of longitudinal bending moment, while the overall depth and thickness of the webs remain constant. Thus, the tested web panels, on which strain gauges were installed, corresponded to a unique cross-section on each girder. Also note that there was no WT bottom flange stiffener present at the strain gauge location on Girder 2.

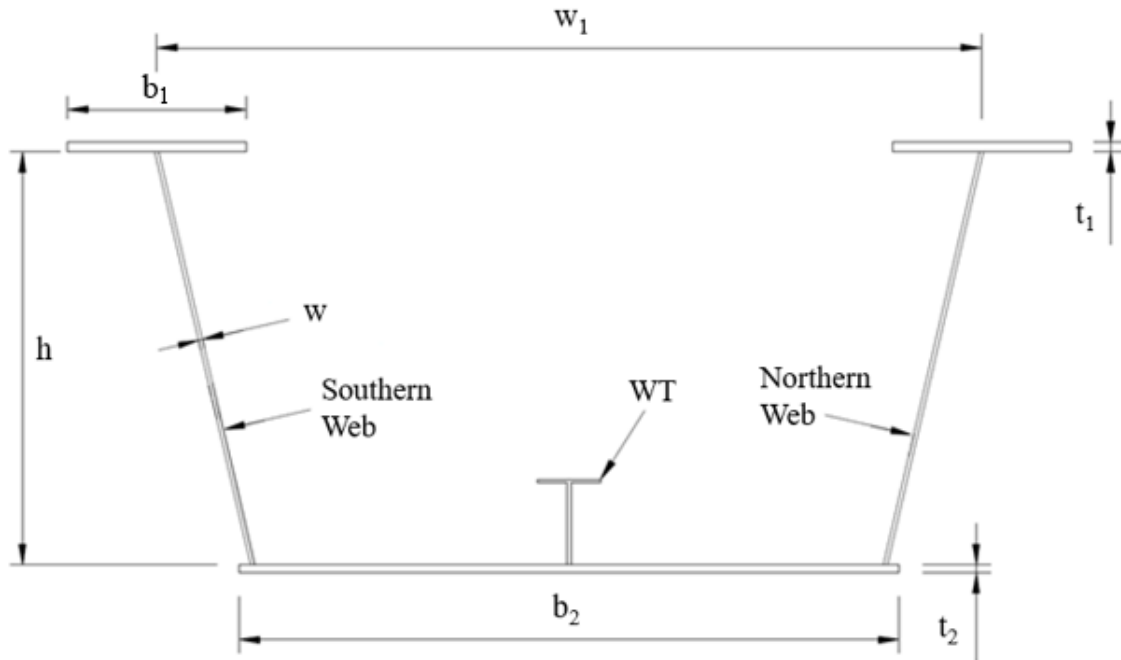


Figure 3.4: Geometry of a typical box girder cross section

Table 3.1: Nominal dimensions of tested box girder sections

Girder	b_1	t_1	b_2	t_2	h	w	w_1	WT
	mm	mm	mm	mm	mm	mm	mm	Stiffener
1	650	60	2400	40	1500	14	3000	WT305x70
2	400	25	2400	22	1500	14	3000	N/A

Strain gauges were installed at a different longitudinal location on each girder in an effort to capture different stress levels in each web panel. Table 3.2 provides information on the location of the centre of the gauge field with respect to the East diaphragm of each girder. A ‘field’ refers to a cluster of uniaxial and biaxial strain gauges installed in a web panel. These locations were selected such that stresses from a maximum cantilever could be generated three times during the launch of Girder 1 and five times during the launch of Girder 2, as illustrated by Figures 3.5 and 3.6 respectively, where the location of the gauge field is highlighted in red in both figures.

Table 3.2: Location of the gauge field & web panel dimensions

Girder	Distance of centre of gauge field with respect to East diaphragm (mm)	a (Stiffener spacing) (mm)	a/h Ratio
1	31855	2770	1.833
2	19390	5540	3.693

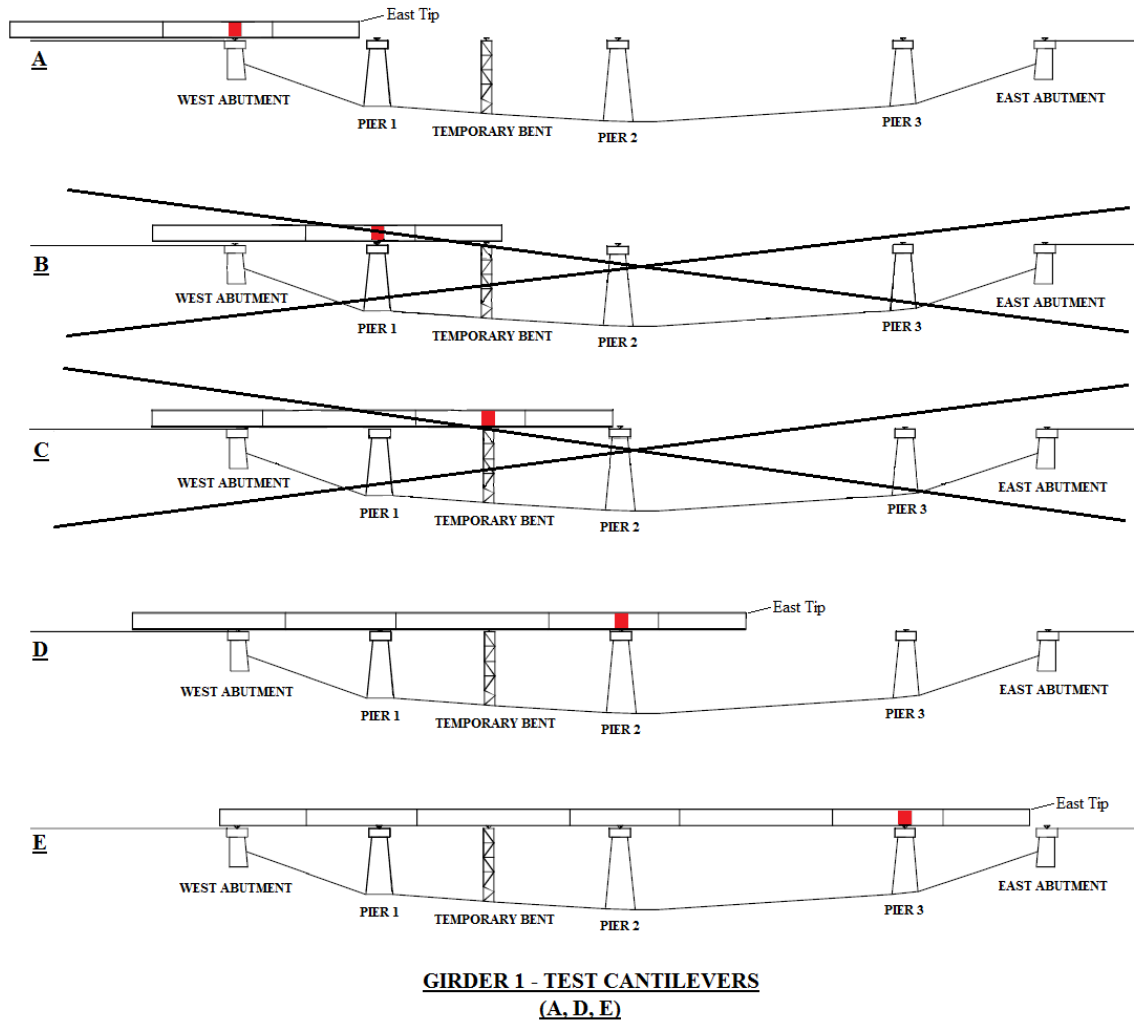
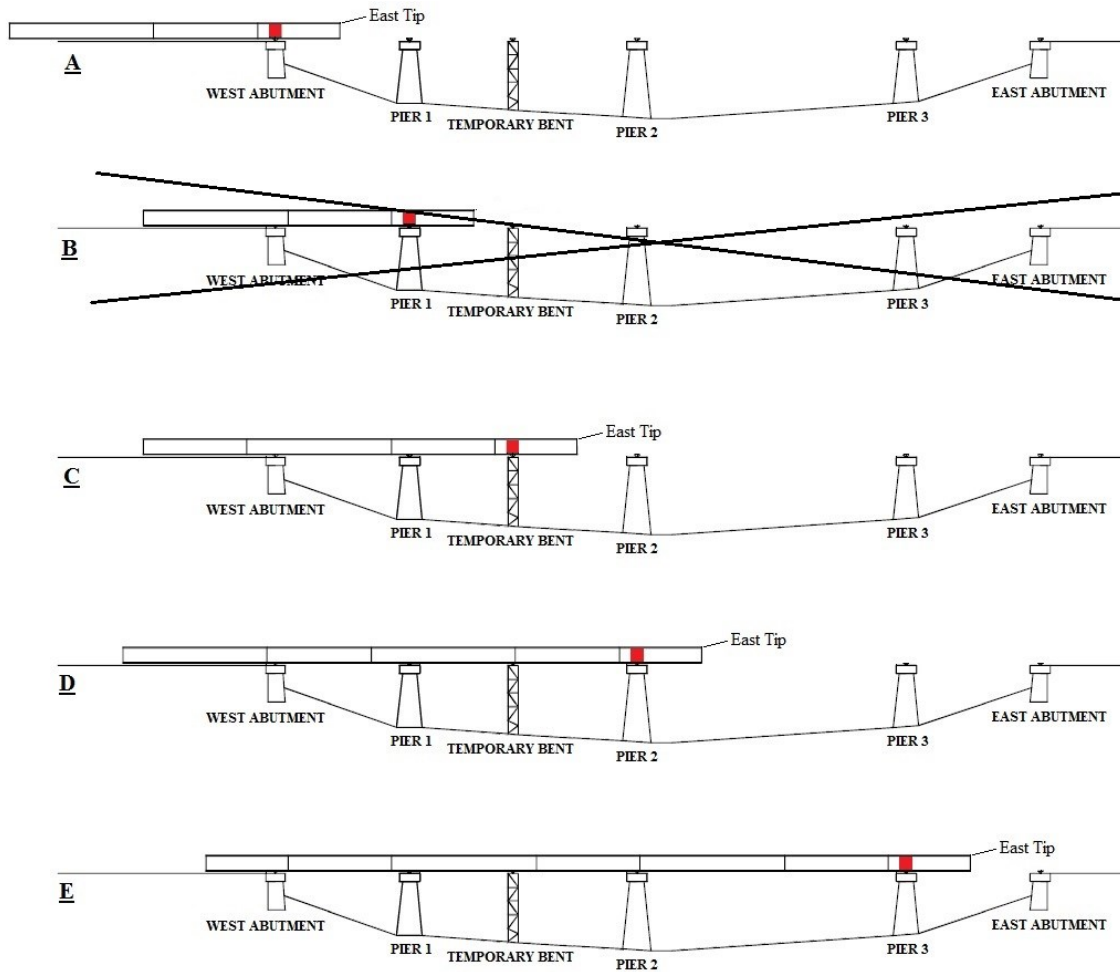


Figure 3.5: Schematic elevation view of the progression of the gauge field from the West to East abutment for Girder 1

In the case of Girder 1, the strain gauges were installed at a distance (31855 mm) from the East diaphragm that was greater than the distance between pier 1 and the temporary bent, as well as the distance between the temporary bent and pier 2. Therefore, cases B and C,

shown in Figure 3.5, were not tested. In the case of Girder 2, the strain gauges were installed at a shorter distance (19390 mm) from the East diaphragm which enabled the test of all 5 locations. Unfortunately, due to inclement weather, the site was temporarily inaccessible and therefore case B was not tested.



GIRDER 2 - TEST CANTILEVERS
(A,C,D,E)

Figure 3.6: Schematic elevation view of the progression of the gauge field from the West to East abutment for Girder 2

Figures 3.7 and 3.8 illustrate a partial plan and elevation view of the longitudinal gauge field arrangements for Girders 1 and 2 respectively. The gauges were installed on both sides of the Southern web of each girder. Further, the gauges were placed in the centre of each tested web panel to limit the restraining effect provided by web stiffeners. The width of the tested web panels differ because the spacing of vertical web stiffeners (a) varies

along the length of the girder. Although the thickness of the bottom and top flanges increased at the shop splice location (see Figure 3.8), the web plate, on which web strain gauges were installed on Girder 2, remained continuous.

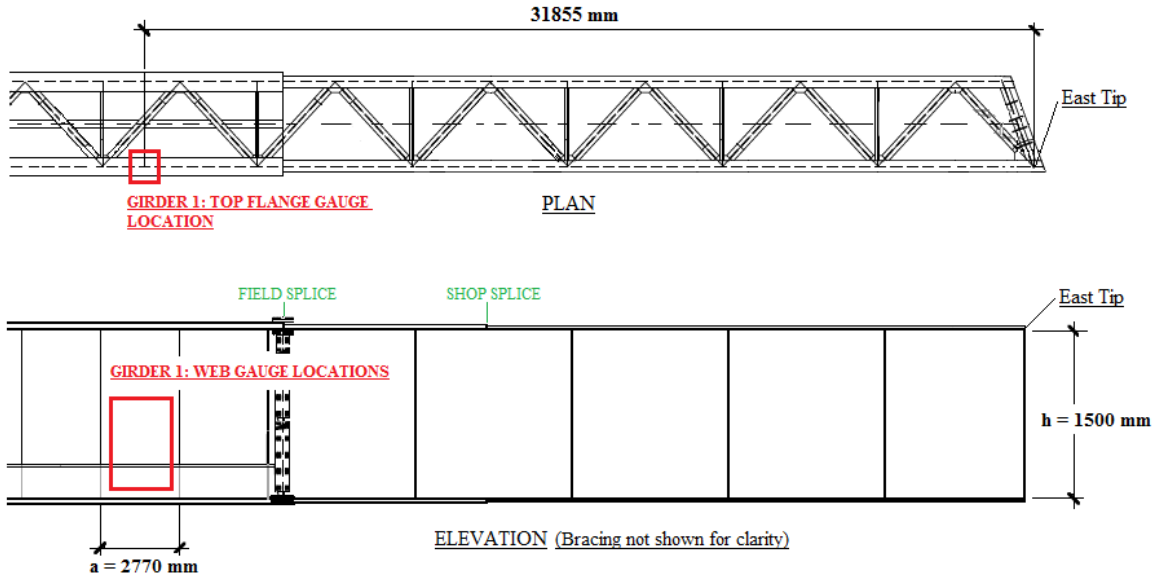


Figure 3.7: Partial plan and elevation views of the gauge field on Girder 1

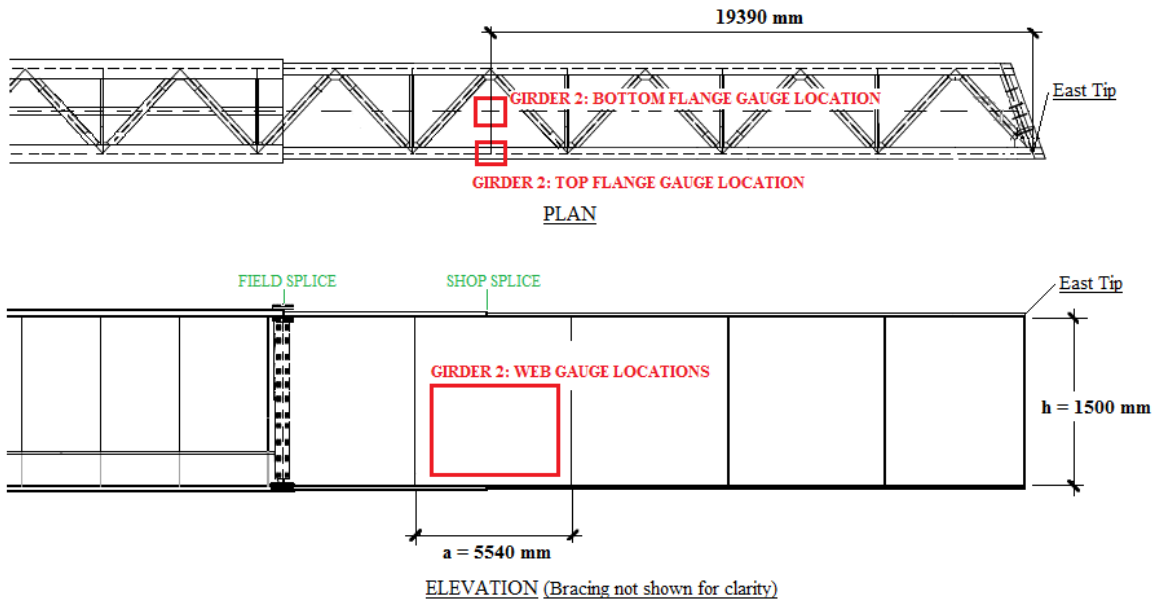


Figure 3.8: Partial plan and elevation views of the gauge field on Girder 2

3.4 Material Properties

Material properties were obtained from material and mill test reports (MTRs) provided by Cherubini Metal Works (CMW), the fabricator of the Shubenacadie River Bridge box girders. Tensile testing of raw plate coupons was completed by each steel mill that supplied plate for the girders. The MTRs reported the steel plate yield stress, F_y , ultimate tensile stress, F_u , % elongation of the coupon, and chemical analysis results for each raw plate that was used to fabricate the girders. CMW also provided material traceability documentation to identify the individual plates used in each girder segment.

Table 3.3 below summarizes the average yield stresses for girder webs and flanges, respectively, within the girder segment on which strain gauges were installed. The modulus of elasticity, E , for each raw plate incorporated into the bridge girders was not provided in the MTRs and therefore, E was calculated using the 0.2% offset method prescribed by the ASTM A370-22 standard (2022). Calculated values for E are presented in Table 3.3.

Table 3.3: Shubenacadie River Bridge steel plate properties

Girder	Location of Girder Segment Containing Strain Gauges	Flange/Web	Plate Thickness (mm)	F_y (MPa)	E (MPa)
Girder 1	Between the first and second eastmost field splices (refer to Figure 3.7)	Top Flange	60	388	194 000
		Web	16	454	227 000
		Bottom Flange	40	365	182 500
Girder 2	Between the eastmost end of the girder and the eastmost first field splice (refer to Figure 3.8)	Top Flange (Section A)	25	413	206 500
		Top Flange (Section C)	35	413	206 500
		Web	16	448	224 000
		Bottom Flange (Section C)	30	406	203 000
		Bottom Flange (Section A)	22	444	222 000

3.5 Field Test Set-Up

A total of 28 web strain gauges were installed on each girder with 14 gauges on each side of the web. The strain gauge arrangement for both girders is depicted in Figure 3.9 where the vertical (s) and longitudinal (b) spacing of strain gauges are given in Table 3.4. The panel width (a) and the roller bearing length (r) are also given in the table. Uniaxial gauges were orientated vertically, and biaxial strain gauges were oriented such that one leg was vertical and one leg was horizontal.

The strain gauges were strategically placed in an effort to capture the strains along the width and height of the web, in the vicinity of the critical buckling height. This height corresponds to the elevation where the maximum out-of-plane deflection would occur at buckling. This height was determined by performing a buckling analysis on a finite element model of a critical section of the girder. The analysis used to determine the critical buckled heights for this field testing is presented in Appendix A. In this study, the critical height, H_{cr} , corresponds to the elevation as shown in Figure 3.9.

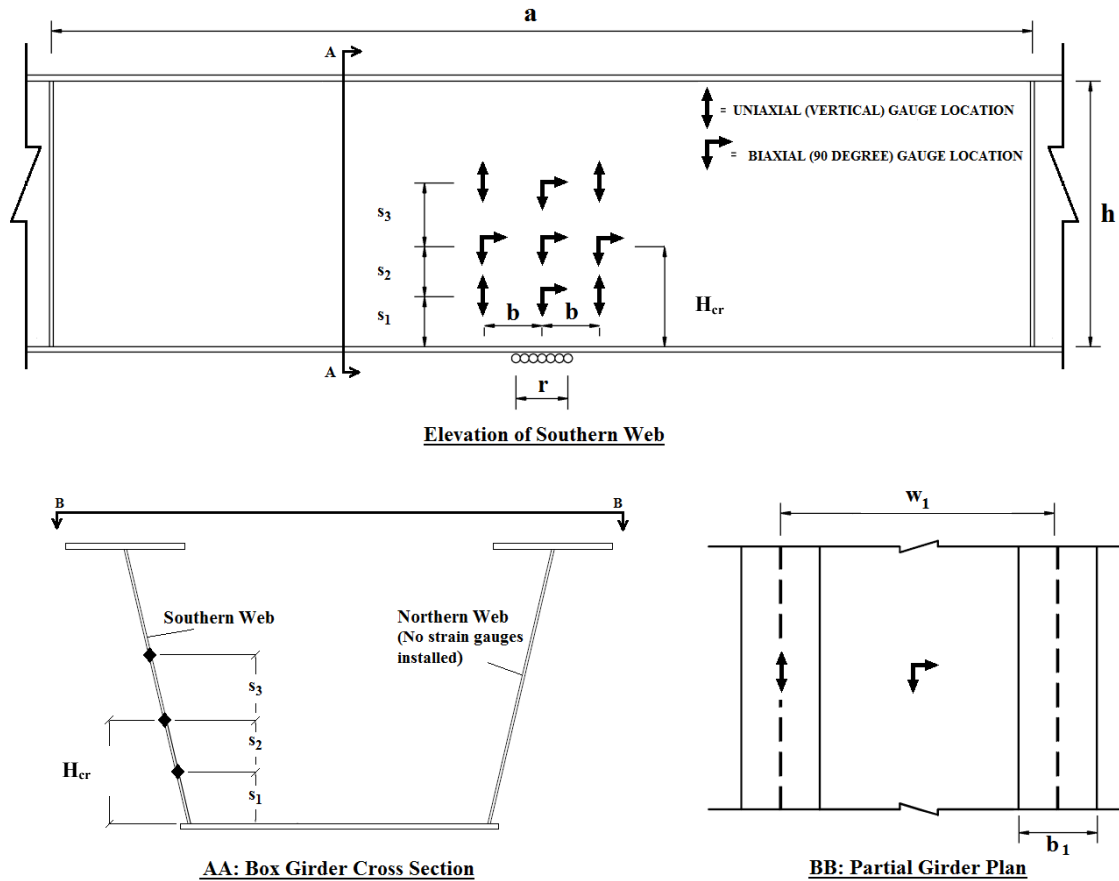


Figure 3.9: Elevation and sectional views of the web and flange strain gauge arrangement

Table 3.4: Vertical and longitudinal spacing of web strain gauges

Girder	a	b	H _{cr}	s ₁	s ₂	s ₃	r
	(mm)	(mm)	(mm)	(mm)	(mm)	(mm)	(mm)
1	2770	325	594	297	297	360	294
2	5540	325	564	282	282	360	294

Additional strain gauges were installed on the top surfaces of the top and bottom flange as shown in Section BB of Figure 3.9. The longitudinal location of these gauges corresponded with the centerline of the web panel gauge field for each girder. For example, the top and bottom flange strain gauges for Girder 2 were installed at 19390 mm from the East tip of the girder. A uniaxial strain gauge was installed at the centre of the top flange and was oriented parallel to the longitudinal axis of the girder. A biaxial strain gauge was installed

at the centre of the bottom flange and was oriented with one leg parallel and one leg perpendicular to the longitudinal axis of the girder. The number of gauges used in the arrangement was primarily dictated by limitations of the data acquisition equipment used for this field testing.

3.6 Data Acquisition Equipment & Instrumentation

3.6.1 Strain Gauges

The strain gauges used for this field testing were 350-OHM Precision Strain Gauges, purchased from OMEGA Engineering. Due to product availability at the time of testing, gauges with different grid sizes were purchased. The grid size varied from 3 mm to 7 mm and the gauge factors ranged from 1.99 to 2.14. Further information pertaining to the strain gauges used in the experimental program, including individual gauge type, location, channel, and gauge factor can be found in Appendix B.

Installation of strain gauges took place in the fabrication yard in January of 2014, prior to the transportation of the girder segments to site. Strain gauges were installed in accordance with guidelines published by Micro-Measurements (Vishay Precision Group, 2014), for strain gauge installations with M-Bond 200 adhesive. A 25000 BTU radiant propane heater was used to locally heat the steel webs to allow for proper bonding of the gauging adhesives. A covered enclosure was built to protect the installation area from winter weather and care was taken to minimize the potential contamination of the strain gauges.

Lead wires were soldered to ribbon leads prior to bonding the gauges to the steel web. Once protected, the lead wires were soldered to 3-core, 22-gauge audio wire. This wire was secured to the webs (shown in Figure 3.10) to prevent movement during transport of the girder as well as during launching.

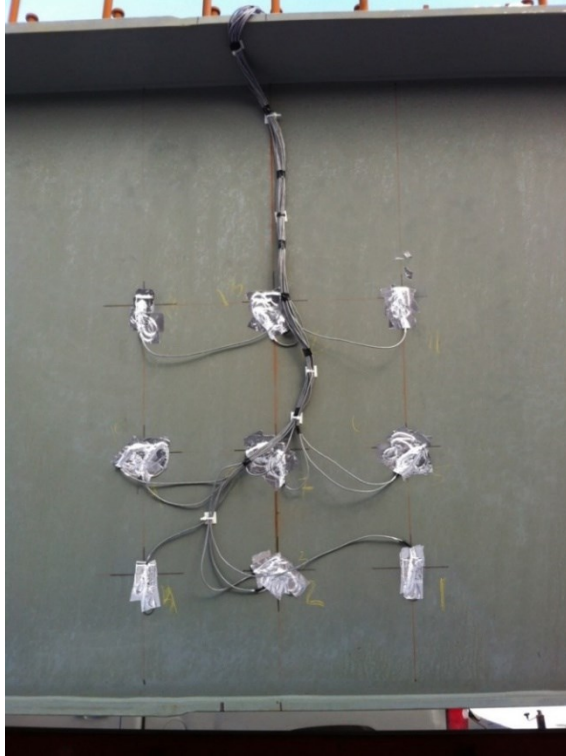


Figure 3.10: Completed gauge field on the outside web of Girder 2

Each gauge was tested prior to transportation to check if it was functioning properly using a TML TC-31k digital strain meter, shown in Figure 3.11. A dense plastic sheet was used to cover and protect the gauges on both sides of the web during transportation.



Figure 3.11: Testing of a uniaxial strain gauge on the inside web of Girder 2

Upon arrival to site, the girder section containing the test web panel was placed on launch pads on the West approach. The data logger was then wired to the strain gauges and the gauges were tested again to ensure working order.

3.6.2 Data Acquisition Equipment

The data logger used for this testing was a Campbell Scientific CR5000. Two 16 channel Campbell Scientific multiplexers were used to increase the channel capacity of the data logger. A total of 32 channels were utilized. The ability to view strains in real time was achieved by installing a Sierra Wireless Raven XT modem and antenna to transmit data. A 12 V external battery was used to power the data acquisition system. The battery was housed in a Rubbermaid container, and two high-density plastic cabinets were used to house the data logger, multiplexers, and wireless modem. Steel plates were used to secure the cabinets to the girder. The cabinets were bolted to the mounting plates, which were then clamped to either the WT bottom flange stiffener or the WT plan bracing. Figure 3.12 depicts the arrangement of the data acquisition equipment installed on Girder 2. The CR5000 and multiplexers are shown in Figure 3.13.

To observe temperature strain, an additional uniaxial strain gauge was installed on an unstressed portion of a steel mounting plate. The location of this gauge is identified as the yellow area, to the right of the battery housing unit, in Figure 3.12. The properties of this strain gauge were consistent with those installed on the box girder webs. However, this strain gauge was installed in the laboratory at Dalhousie University.



Figure 3.12: Data acquisition equipment arrangement of Girder 2



Figure 3.13: Photos of the CR5000 data logger (left) and two multiplexers (right)

The data logger was programmed to record strain readings at a rate of 0.05 Hz, or one reading every twenty seconds for Girder 1. The recording rate was increased to 0.1 Hz for the test on Girder 2 to better accommodate the actual pull speed of the girder. In each test, the data logger was programmed to take fifteen strain measurements at each interval. The first three and last two measurements of each interval were omitted, and the average strain of the remaining ten measurements was recorded.

3.7 Test Procedure

Data acquisition equipment was installed on Girder 1 once the required number of girder segments were set onto launch pads. To track the physical position of the gauge field throughout the entirety of the launch, the West abutment was selected as a reference datum, and a length of 10 m (5 m to the East and West of the centre of the gauge field) was marked on the Southern web at 1 m intervals. Identical 10 m intervals were then marked on the Southern web so that as the gauge field (shown in Figure 3.14) passed over consecutive piers, a corresponding interval would pass over the West abutment. The time that each interval passed over the centreline of the West abutment was recorded. This time was then correlated with a time stamp from the recorded data to obtain the strain reading.



Figure 3.14: Gauge field of Girder 1 approaching pier 1

The camber profile of the girder was monitored throughout the launch. The camber affects the spanning distance of the girder during launching. When the bottom flange is not in contact with a particular roller bearing, the actual span is longer and therefore load effects are more significant. In addition to monitoring the position of the girder throughout the entirety of the launch, the average temperature of the web and flanges was recorded using a thermometer.

Upon completion of the first girder launch, a shunt calibration was performed as per the guidelines outlined in Micro-Measurements Tech Note TN-514. The shunt calibration was performed to assess the sensitivity in the entire circuit for each channel (i.e., the combination of the strain gauge, lead wires, and gauge wire) and was used to adjust the gauge factor for each strain gauge accordingly. A resistor with a resistance of 87150 ohms was used in the shunt calibration. Following the shunt calibration, the data acquisition equipment was disassembled from Girder 1 and installed on the WT plan bracing of

Girder 2. Again, intervals were marked on the Southern web to track the position of the gauge field on Girder 2 accordingly. Following the shunt calibration for Girder 2, the data acquisition equipment was disassembled and removed from the girder.

3.8 Potential Sources of Error from Field Testing

This section discusses the main areas of potential error which may have affected the accuracy of the experimental results. These potential sources of error include, but are not limited to, difficulties associated with cold weather strain gauge installation, equipment malfunctions, and construction issues during girder erection.

Strain gauge installation was conducted outdoors in Dartmouth, Nova Scotia, in January 2014. The adhesive, and other fluids that were used to prepare the steel for bonding of the strain gauges, required the steel to be within a specified temperature range. Although a heat gun and radiant heater were used to locally heat the web to an acceptable installation temperature, ambient elements (i.e., winter wind) may have cooled the steel immediately after the application of the heat gun, causing gauging fluids to freeze, and thus preventing the gauge from properly bonding to the steel.

Further, malfunctioning strain gauges may have been caused by overheating of the strain gauge grid from soldering operations and subsequent rapid cooling. This could cause a lead wire to become brittle and break. If the break occurred after the gauge was protected, the break would not have been visible.

One temperature gauge was used in the test set up and was positioned on the interior of the box girders (on the bottom flange stiffener for girder 1 and on the plan bracing for girder 2). During launching, drastically different steel temperatures were noted between the interior and exterior sides of the webs and flanges. The use of a single gauge positioned at one location may not have been sufficient to capture the effect of thermal strains over the whole cross section.

During field testing, the internal battery of the CR5000 data logger (responsible for powering the internal clock) died over a two-day break in construction. This was noticed and corrected during field testing. However, without calibration from the manufacturer, the presence of inherent errors related to the recorded time stamps, for example, remain unknown to the author.

Finally, construction equipment and construction practices, not specifically related to launching, may have introduced additional stresses into the girders. Sources such as varying girder pull speeds, lateral stresses from attempting to straighten the travel path of the girder on the roller bearings, jacking of the girder while the gauge field was passing over a pier, and increased dead load from ice and snow inside the girder, may have contributed to producing potentially erroneous data. Future similar experimental programs could attempt to pause the launch at critical locations to remove potential dynamic effects. Instead of utilizing a data logger system, once the launch has been paused, the strains could be manually read using a strain meter.

CHAPTER 4 EXPERIMENTAL RESULTS

4.1 General

The experimental program was designed to record the stresses experienced by the Shubenacadie River Bridge box girders during launching. The stress data was intended to be used to verify the numerical model. The experimental program did not involve loading the girders to the point of failure of any part of the cross section. This chapter presents the data collected during the experimental program and provides a discussion on the observed stresses.

As the strain gauge field passed over a support, strain readings were recorded in 1 meter intervals, starting 5 meters ahead of the gauge field and ending 5 meters behind, as shown in Figure 4.1. The intent was to observe the change in strain at each interval to develop an understanding of the web stress pattern as the gauge field passed over a support. However, due to the varying pull (launch) speed experienced in the field, the observed change in strain between consecutive intervals was negligible. Therefore, only the strains and stresses observed when the gauge field was located directly above a roller support are presented herein.

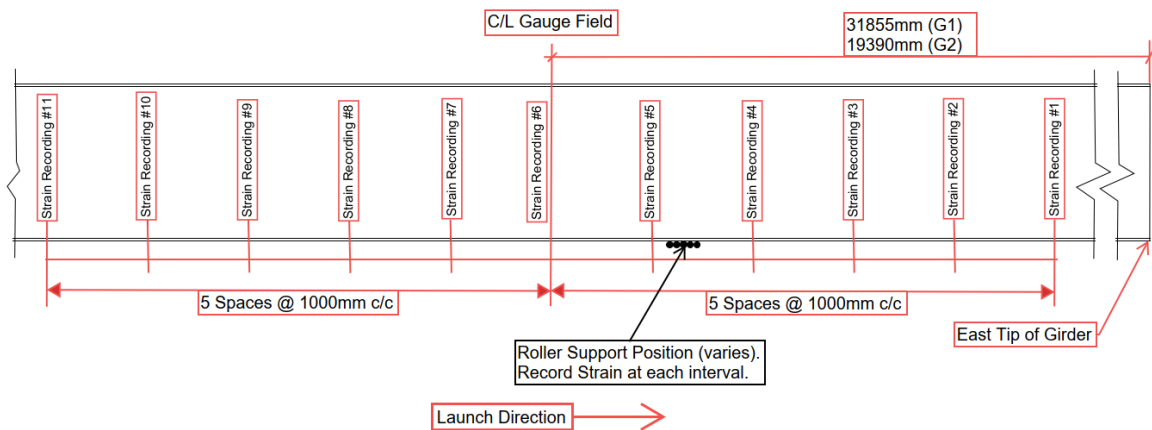


Figure 4.1: Elevation view of strain recording locations

4.2 Global Load Effects

Table 4.1 below presents the global load effects resulting from the dead load of the girders corresponding to the positions of the strain gauge field and associated cantilever lengths. The global load effects were used to calculate the expected flange normal stresses and web shear stresses (refer to Section 4.3 below).

It should be noted that the pre-construction girder launch sequence involved the use of a crane to control girder tip deflections as the east end of each girder arrived at Pier 3. The crane was to fully release the girder once the girder was supported by rollers at Pier 3. The longitudinal strain gauge locations were selected to observe repeatable stresses along the length of the launch. This would have allowed for the maximum cantilever to be realized at three locations in the case of G1 and at four locations in the case of G2. However, during construction, the contractor did not follow the original launch sequence. Instead, the crane connected to the east tip of each girder much earlier than anticipated. The crane connected to G1 once an approximately 10 m long cantilever was launched beyond Pier 2. In the case of G2, the crane connected to the east tip once an approximately 10 m long cantilever was launched beyond Pier 3. In doing so, the crane removed an unknown portion of dead load from the system; the slings between the crane hook and the girder were not slack as the girders were launched. As a result, the stresses at the gauge field were not repeatable beyond Pier 2 for G1 and beyond Pier 3 for G2. Only the stresses that are quantifiable through static analysis and, in the case of G2, repeatable, are presented in the following sections.

Table 4.1: Global load effects

Data Set ID	Location of the Strain Gauge Field Centerline	Cantilever Length (mm)	Total Reaction (kN)	Moment (k-Nm)	Shear (kN) Immediately East of Gauge Field	Shear (kN) Immediately West of Gauge Field
G1-A	West Abutment	31855	889	-5550	-397	442
G2-A	West Abutment	19390	463	-1959	-202	261
G2-C	Pier 1	19390	482	-1959	-202	280
G2-D	Pier 2	19390	502	-1959	-202	300

4.3 Theoretical Stresses at Gauge Field

The theoretical flange normal stresses and maximum web shear stresses from the global load effects are presented in Table 4.2. The maximum top and bottom flange stresses, σ_{TF} , and σ_{BF} , and the maximum shear stress, τ_{Max} , were calculated using the principles of mechanics with the material properties specified by the fabricator as reported in Chapter 3. Girder 2 shows repeatability between data sets A, C, and D in terms of the top and bottom flange stress. τ_{Max} varies slightly between data sets A, C, and D due to the varying back span lengths as the girder was launched.

Table 4.2: Theoretical stresses

Data Set ID	σ_{TF} (MPa)	σ_{BF} (MPa)	τ_{Max} (MPa)
G1-A	43	-36	11.8
G2-A	34	-19	3.3
G2-C	34	-19	3.5
G2-D	34	-19	3.8

4.4 Post Processing of Recorded Data

Data loggers measured and recorded the resistance of the strain gauges throughout both girder launches. To obtain the change in resistance, the initial output resistance at the time of strain gauge installation was subtracted from the recorded resistance at the time of interest (i.e., when the strain gauge field was centered above a specific roller). The change in resistance was thermally corrected to remove the influence of thermal strains. The corresponding strain was calculated using Equation [4.1] (Campbell Scientific, 2006) for a quarter bridge strain gauge:

$$\mu\varepsilon = \frac{-4 \times 10^6 V_r(0.001)}{GF(1 + 2V_r)} \quad [4.1]$$

where: $\mu\varepsilon$ is the dimensionless microstrain, V_r is the change in electrical resistance, and GF is the gauge factor adjusted per the shunt calibration. It should be noted that strain

gauge rosettes were not used on the webs of the box girders. Therefore, the orientation of experimental stresses presented herein correspond to the direction of the strain gauge placement.

4.5 Experimental Results

The following sections present the longitudinal and vertical web stresses as well as the longitudinal flange stresses recorded during the G1 and G2 launches. Refer to Figures 3.7 and 3.8 for the global locations of the strain gauges for each girder. Stresses are reported for both exterior and interior sides of the web from strain gauge pairs that were installed at the same vertical and longitudinal positions on opposite sides of the web. Figures 4.2 and 4.3 depict a schematic of the gauge numbers, shown in the red boxes, for strain gauges installed on the outside and inside surfaces of the south web, respectively. The pairing is summarized in Table 4.3.

Table 4.3: Strain gauge # paring

Web Gauge # Paring:														
Outside Web	1	2	3	4	5	6	7	8	9	10	11	12	13	14
Inside Web	15	16	17	18	19	20	21	22	23	24	25	26	27	28

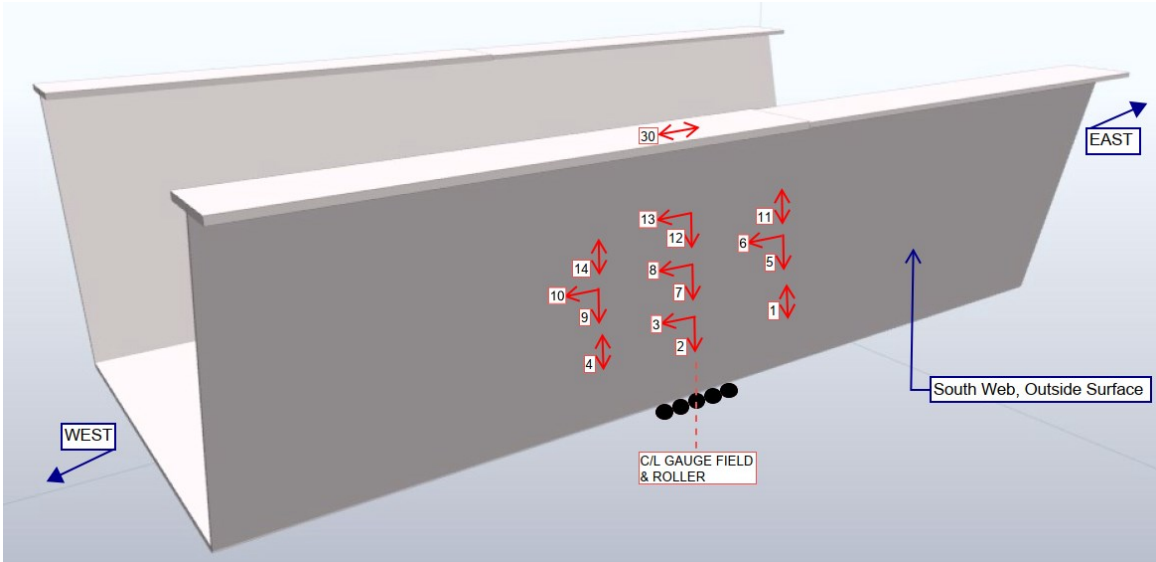


Figure 4.2: Strain gauge numbering schematic - outside web surface

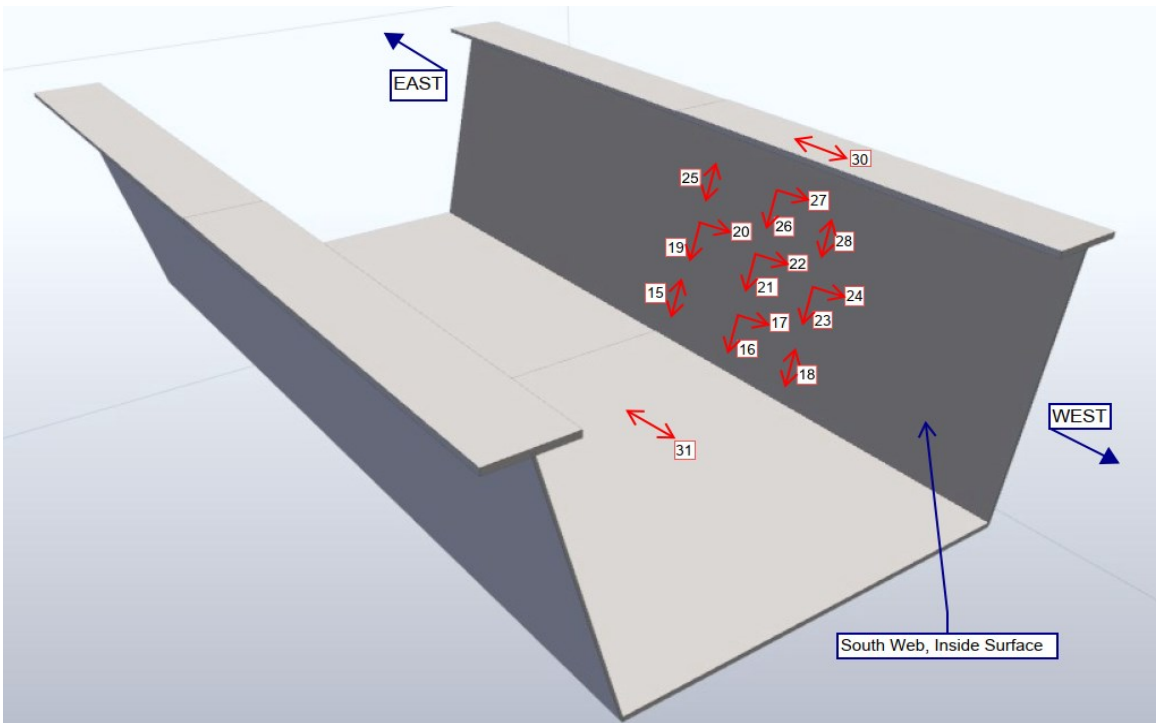


Figure 4.3: Strain gauge numbering schematic – inside web surface

The strain gauge numbers correspond to the recorded stresses shown on Figures 4.4, 4.5, 4.6, and 4.7. These figures feature a red vertical ‘web fold line’ where the left-hand side and right-hand side diagrams represent the measurements obtained on the outside and inside web surfaces respectively. In the following figures, positive values represent tensile stresses and negative values represent compressive stresses.

4.5.1 Girder 1 Recorded Stresses

The stresses obtained from the launch of G1 at the instant when the centerline of the strain gauge field was located directly above the west abutment roller support are presented in Figure 4.4. The legend in the figure shows the types of stress being measured, and “no data” indicates malfunction of strain gauges where no data was recorded. In this case, gauges 12 and 13 on the outside face of the web malfunctioned and gauges 18, 20, 21, and 26 on the inside face of the web malfunctioned.

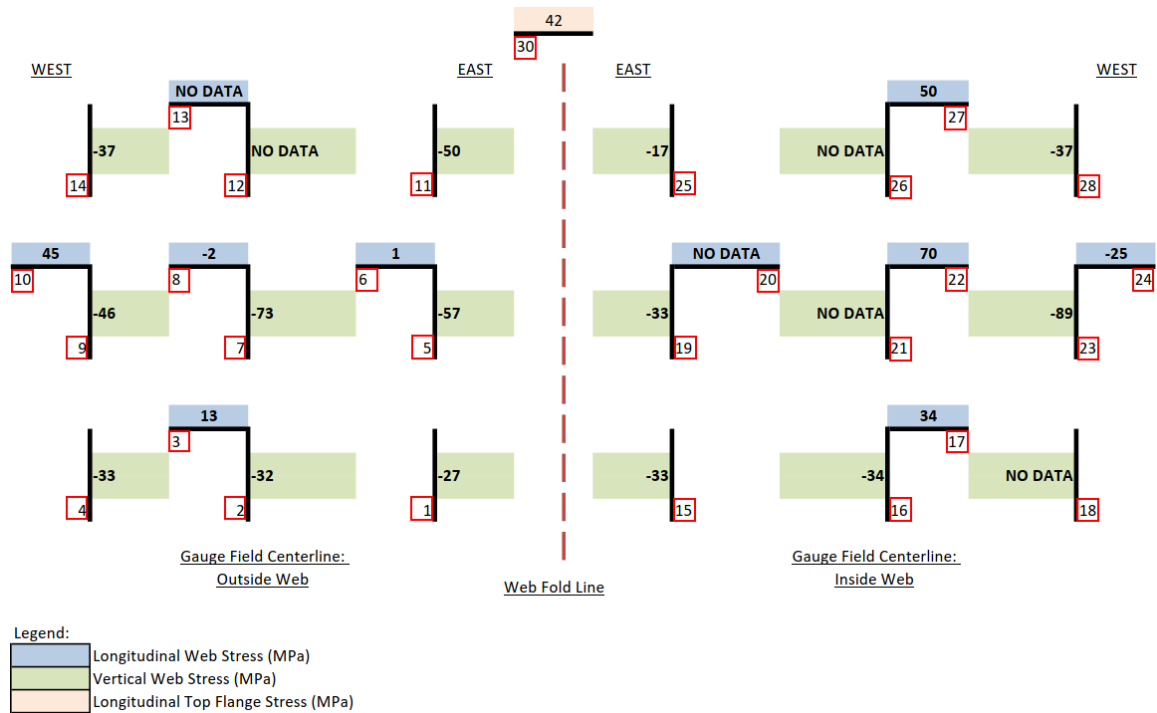


Figure 4.4: G1-A results

The following observations can be made from the G1-A data presented in Figure 4.4.

Longitudinal flange stress:

- The longitudinal top flange stress (42 MPa) shows good agreement with the theoretically predicted stress (43 MPa).
- The bottom flange strain gauge was damaged by ironworkers before the girder launch began and no data is available to compare to the theoretical stress.

Web stresses at lowest row of strain gauges:

- The lowest row of strain gauges was installed 297 mm above the top surface of the bottom flange plate. The vertical stresses at this elevation show good general agreement through the thickness of the web. Good agreement is observed between gauges 1, 2, and 4 on the outside face of the web with a maximum difference of 6 MPa between “neighbouring” gauges. The stresses observed at gauges 15 and 16 show a difference of 1 MPa on the inside face of the web.
- The longitudinal stresses at gauges 2 and 16 are positive indicating tensile stresses. However, based on the reaction from the roller and the negative bending region below the neutral axis associated with the cantilevered condition, it would be expected that the stress would be compressive. In addition, there is a 21 MPa difference in longitudinal stress between the inside and outside surfaces of the web.

Web stresses at middle and upper rows of strain gauges:

- The middle and upper rows of strain gauges were installed 594 mm and 954 mm above the top surface of the bottom flange plate, respectively. Unlike the lowest row, in general, the vertical stresses at the middle and upper rows do not show similarities across the neighboring gauges and through the thickness of the web. The longitudinal stresses at the middle and upper rows also vary significantly between adjacent gauges and gauges on the opposite side of the web.

In summary, the top flange longitudinal stress compares well to the theoretically predicted stress, but the other recorded stresses do not provide reliable results.

4.5.2 Girder 2 Recorded Stresses

The stresses obtained from the launch of G2 are presented in the figures below. Three data sets are available for G2, which correspond to the instant when the centerline of the strain gauge field was located directly above the west abutment roller support (G2-A, Figure 4.5), Pier 1 (G2-C, Figure 4.6) and Pier 2 (G2-D, Figure 4.7).

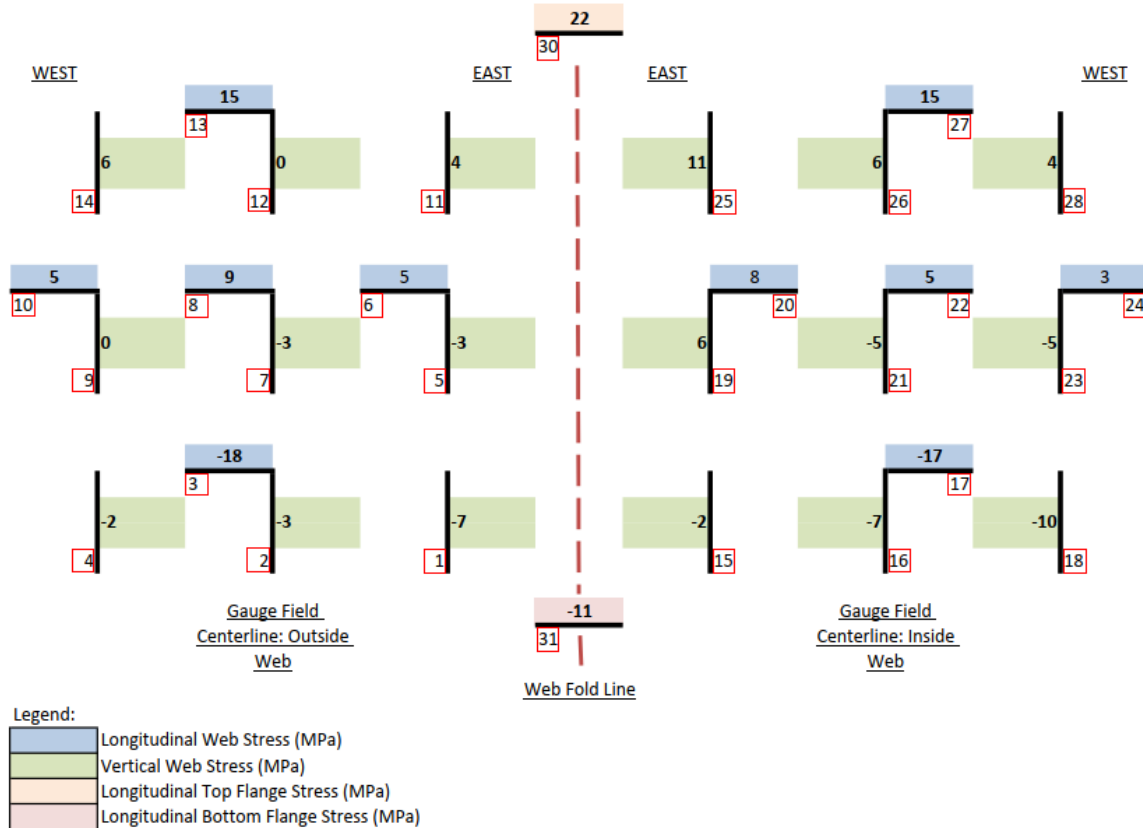


Figure 4.5: G2-A results

The following observations can be made from the G2-A data presented in Figure 4.5.

General:

- There appears to be a general trend in longitudinal stresses where compressive stresses are observed near the bottom of the cross section (lowest row of gauges) and the stresses gradually increase to tensile stresses near the upper portion of the cross section (upper row of gauges). Stresses are observed to be small at the middle row of gauges, but tensile in nature. This trend corresponds to the middle row of

gauges being slightly above the theoretical neutral axis. The middle row of gauges was installed 35 mm above the elevation of the theoretical neutral axis.

Longitudinal flange stresses:

- The longitudinal top flange stress (22 MPa) is less than the expected top flange stress (34 MPa). Similarly, the longitudinal bottom flange stress (-11 MPa) is less than the expected stress of (-19 MPa).

Web stresses at lowest row of strain gauges:

- The lowest row of strain gauges was installed 282 mm above the top surface of the bottom flange plate. The vertical stresses at this elevation show fair general agreement through the thickness of the web between gauges 1 & 15, 2 & 16, and 4 & 18. Fair agreement is also observed between neighbouring gauges 1, 2, & 4 on the outside face of the web and between gauges 15, 16, & 18 on the inside face. The maximum difference in stress between web gauges on the lowest row is 8 MPa.
- The longitudinal stresses at gauges 3 and 17 show good agreement, with a difference of only 1 MPa.

Web stresses at middle row of strain gauges:

- The middle row of strain gauges was installed 564 mm above the top surface of the bottom flange plate. There is good agreement of vertical stresses between the centre and west most gauges (gauges 7, 9, 21 & 23).
- Opposite vertical stress orientations were observed between gauges 5 and 19. Gauge 5, on the outside of the web depicts a compressive stress (-3 MPa) but a tensile stress was observed at gauge 19 on the inside of the web (6 MPa). The magnitudes of stress are in the range of the expected maximum shear stress.
- The longitudinal stresses at the middle row of strain gauges (gauges 6, 8, 10, 20, 22, & 24) show good agreement on both sides of the web with a maximum difference of 4 MPa through the thickness of the web.

Web stresses at upper row of strain gauges:

- The upper row of strain gauges was installed 924 mm above the top surface of the bottom flange plate. There is fair agreement of the vertical stresses at gauges 11,

12, 14, 25, 26, & 28 with a minimum difference of 2 MPa and a maximum difference of 7 MPa through the thickness of the web.

- The longitudinal stresses at the upper row of strain gauges show excellent agreement with both gauges 13 and 17 indicating a tensile stress of 15 MPa.

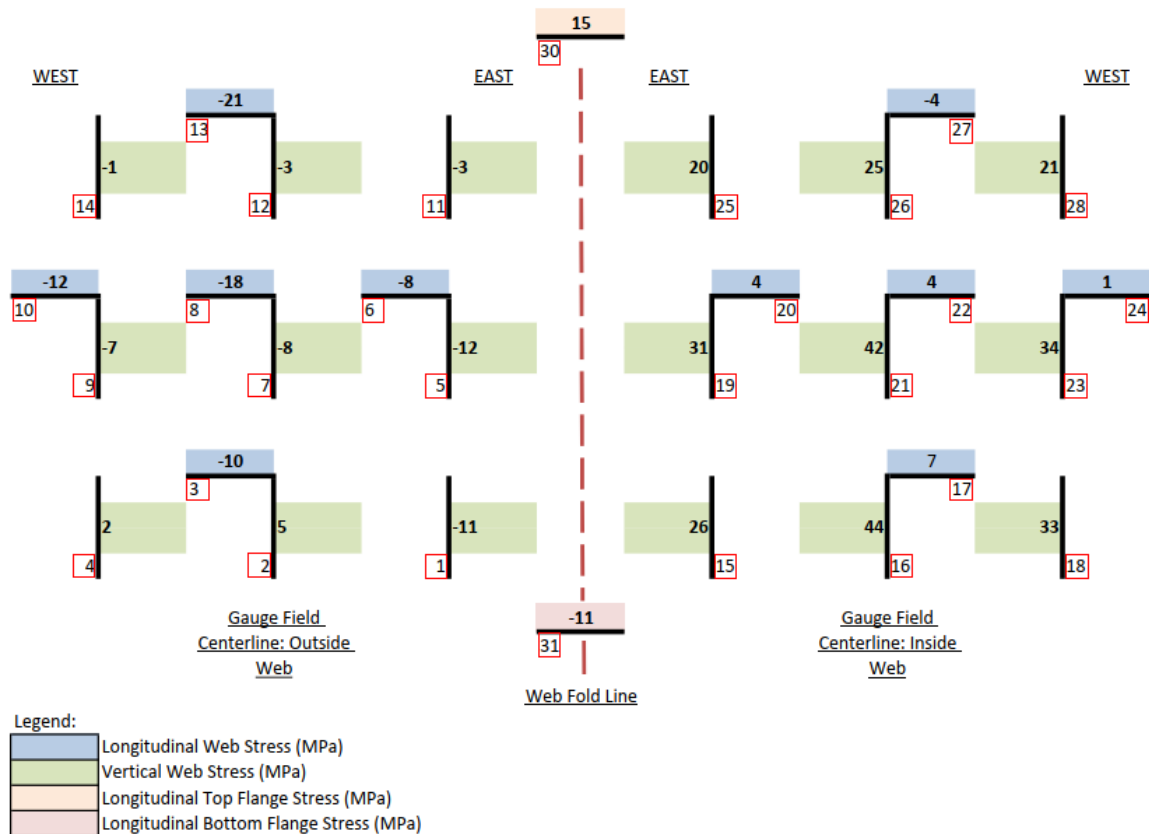


Figure 4.6: G2-C results

The following observations can be made from the G2-C data presented in Figure 4.6.

Longitudinal flange stresses:

- The longitudinal top flange stress (15 MPa) is significantly less than the theoretically expected top flange stress (34 MPa). Similarly, the longitudinal bottom flange stress (-11 MPa) is less than the expected stress (-19 MPa).

Web stresses:

- There is a 20 - 40 MPa difference in vertical stress between gauges on the interior and exterior surfaces of the web. The stresses on the inside face of the web are tensile and no apparent trend is noticeable vertically or longitudinally. The stresses

than the expected stress of (-19 MPa). The orientations of the observed stresses are consistent with the theoretical stress orientations however, the magnitudes of top and bottom flange stresses are lower than expected by 7 MPa and 6 MPa, respectively.

Web stresses at lowest row of strain gauges:

- The vertical stresses on the exterior side of the web (gauges 1, 2, & 4) show fair agreement with neighbouring gauges. However, poor agreement is observed on the interior face of the web (gauges 15, 16, & 18) with a maximum difference in stress of 28 MPa between gauges 15 and 18.
- The longitudinal stresses at gauges 3 and 17 are consistent at 1 MPa, however based on the location of the gauges, compressive stresses would be expected here.

Web stresses at middle row of strain gauges:

- The middle row of strain gauges was installed 564 mm above the top surface of the bottom flange plate. There is good agreement of vertical stresses among neighbouring strain gauges 5, 7, and 9 on the exterior side of the web and good agreement of vertical stresses among gauges 19, 21, and 23 on the interior side of the web. The stresses are compressive on the outside of the web and tensile on the inside of the web which would tend to indicate inward bending of the web panel.
- The longitudinal stresses at gauges 8, 10, 20, 22, and 24 are similar and are within 3 MPa of each other. These small stresses are consistent with a small bending stress near the centroid of the section. The stress at gauge 6 appears to be an outlier.

Web stresses at upper row of strain gauges:

- The upper row of strain gauges was installed 924 mm above the top surface of the bottom flange plate. There is fair agreement of the vertical stresses through the thickness of the web with a minimum difference of 4 MPa occurring between gauges 14 & 28, and a maximum difference of 5 MPa occurring between gauges 11 and 25.

In summary, no obvious trend of longitudinal or vertical stresses is noted. The vertical stresses observed at the middle row of gauges would tend to indicate inward bending of

the web and this is loosely apparent at the lowest and uppermost rows as well. The flange stresses are approximately 30% less than the theoretically expected stresses.

4.6 Concluding Remarks

The experimental program involved the field monitoring of two steel box girders as they were erected via the launching method. Due to the unexpected change of launching plan where a crane was used to control girder tip deflections after the instrumentation was made, data from only one location was collected for G1 (reduced from three). Similarly, data from only three locations was collected from G2 (reduced from four).

In general, although some individual trends are noticeable between data sets, the magnitudes of these stresses vary to a significant extent which put the quality and accuracy of the results in question. While the exercise of field monitoring is valuable, the results underscore the difficulty of achieving quality and consistent information intended for the field monitoring in the first place. Consequently, it was decided that the data collected will not be used to verify the finite element model presented in the subsequent chapter. As a result, the finite element model required verification through other methods including comparing the finite element model to analytical results and other work available in the literature.

CHAPTER 5 FINITE ELEMENT ANALYSIS

5.1 General

A finite element study was conducted to investigate the effects of critical parameters on the web panel buckling capacity of steel box girders subjected to combined patch loading and bending moments. The data collected during the experimental program was intended to verify the outputs from the G1 and G2 finite element models. However, due to the poor quality of the experimental results, the finite element models were verified using other methods. This chapter describes the development of the finite element model and its verification.

The finite element modeling was carried out using Altair® S-FRAME 3D Structural Analysis Software Version 2022.2 (2022). S-FRAME is a commercial software capable of modeling geometric nonlinearities and it offers a large number of element and boundary condition formulations which makes it a robust finite element package for structural engineers. Its simplicity and easy implementation make it an attractive analysis tool in the consulting industry. As the current study investigates steel web panel buckling in the elastic stress range, as is consistent with launching situations, linear elastic material properties are considered appropriate for this work and are sufficiently handled by S-FRAME.

5.2 Description of Elements

The finite element models were constructed using two different element types available in S-FRAME. The flanges and web plates were modeled using 3D quadrilateral thick shell elements and the bracing members were modeled using 3D beam elements. The shell elements have both out-of-plane (bending) and in-plane (membrane) capabilities which makes this element type suitable for analyzing geometries that are susceptible to geometric nonlinearities as well as large displacements and rotations. The beam elements are uniaxial elements with tension, compression, torsion, and bending capabilities. A summary of the element properties and degrees of freedom (DOF) for elements used in the numerical study

is presented in Table 5.1. It should be noted that where appropriate, the beam-to-shell element rotational degrees of freedom (i.e., bracing member-to-box girder web joints) were released to simulate the behaviour of the connections.

Table 5.1: Element summary

Element Type	Number of Nodes	Translational DOFs (At Each Node)	Rotational DOFs (At Each Node)
Quadrilateral Shell	4	U_x, U_y, U_z	$\theta_x, \theta_y, \theta_z$
Beam	2	U_x, U_y, U_z	$\theta_x, \theta_y, \theta_z$

5.3 Material Stress-Strain Relationship

Two groups of linear elastic material models were used to represent the behaviour of the steel plates which make up the box girders. The first group, shown in Figure 5.1, was used to validate the data collected during the experimental program. The individual elastic moduli, E , for specific flanges and webs, based on the material test reports (MTR) provided, were incorporated into the S-FRAME verification finite element model. In practice, girders erected via the launching method are designed so that the stresses developed in the girders remain within the elastic zone. All the material models implemented were linear elastic up to the respective specified yield stress for each section (web or flange plate) based on the MTR.

The second group consisted of a single material model, shown in Figure 5.2, and was used to define the material behaviour in the parametric study. The standard material properties were used for steel where an elastic modulus E , of 200,000 MPa and a yield stress F_y , of 350 MPa were assumed.

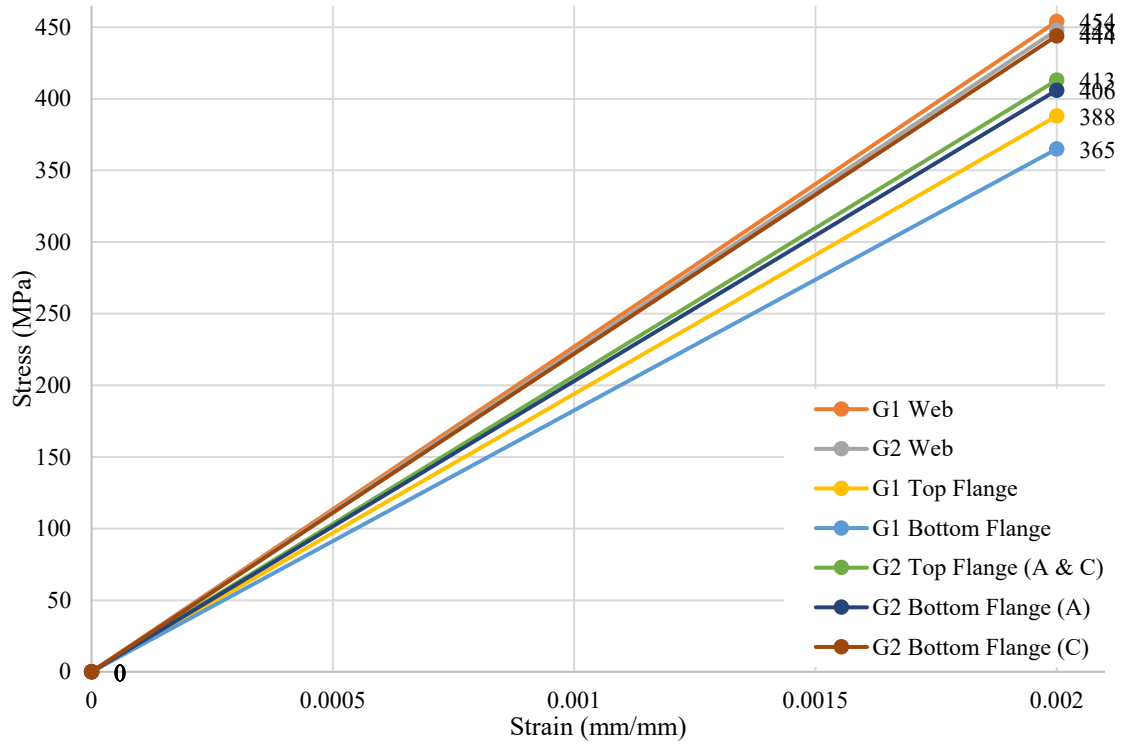


Figure 5.1: Material models used to verify the experimental results

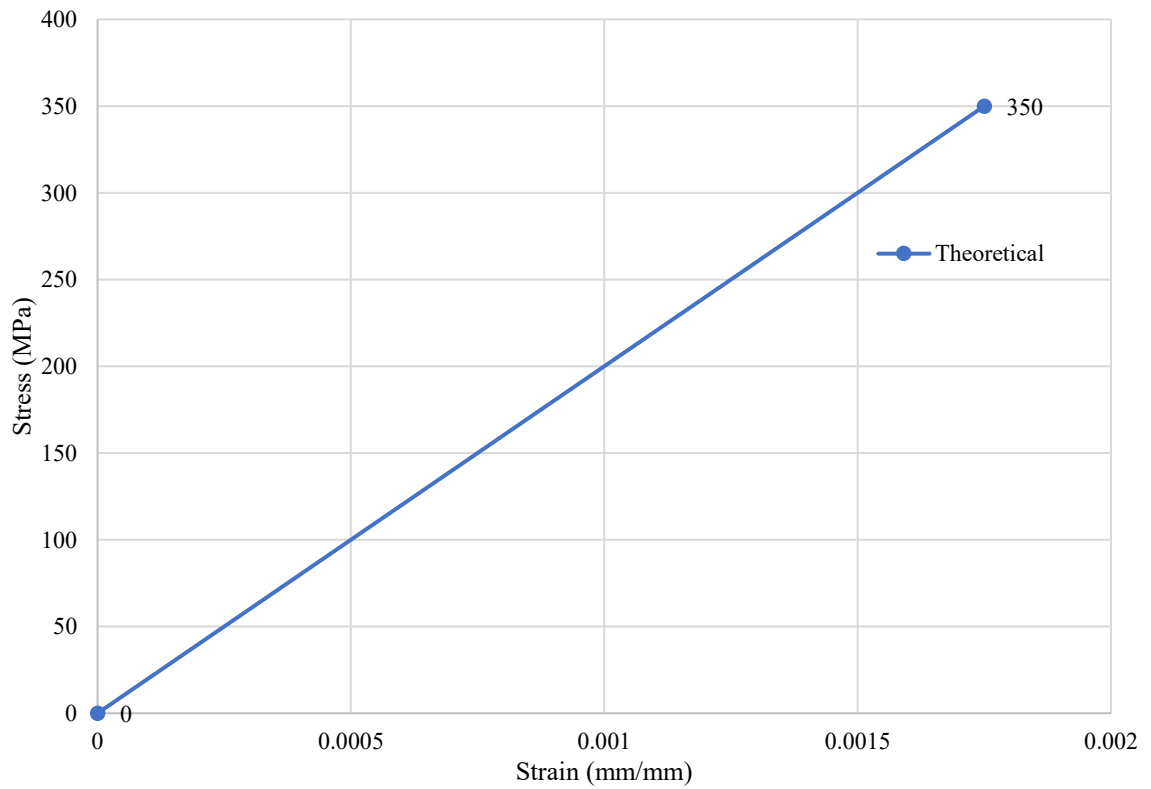


Figure 5.2: Material model used for the parametric study

5.4 Girder Model Length & Finite Element Mesh

For efficiency, a segment of each girder length was isolated and modelled instead of modelling the entire girder. The web panel of interest occurs when the roller is located between two vertical web stiffeners. A comparative test was carried out to assess the effects of modelling a one-bay long girder segment (i.e., the length of a girder between two vertical braced frame locations) versus the effects of modelling a three-bay long girder segment. Figure 5.3 shows the extents of the one-bay and three-bay finite element model.

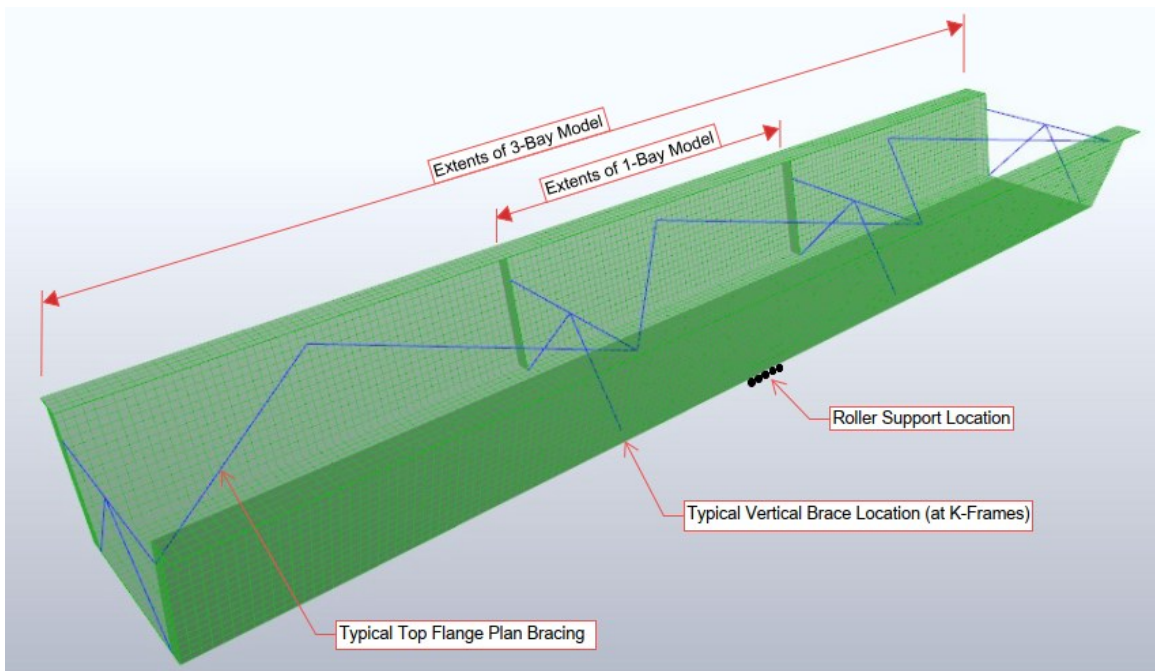


Figure 5.3: Extents of one-bay and three-bay finite element models

In each case, the global load effects were applied to the models at the girder ends where each girder segment was isolated from the entire girder. As shown in Table 5.2, the stresses at the centerline of the web panel above the roller support are similar for a one-bay and three-bay long model. Therefore, only the one-bay scenario is modeled going forward. It should be noted that the small difference in G1-A bottom stress can be attributed to the presence of the WT bottom flange stiffener and the patch load which alters the bottom flange stress distribution.

Table 5.2: One-bay versus three-bay stresses above roller support

Model	FE Top flange Stress (MPa)	Theoretical Top flange Stress (MPa)	FE Bottom Flange Stress (MPa)	Theoretical Bottom flange Stress (MPa)	FE Web Stress at H_{CR}, (MPa)
G1-A 1 Bay	42.2	43.0	-33.1	-35.8	-4.6
G1-A 3 Bay	41.8	43.0	-33.3	-35.8	-4.7
G2-A 1 Bay	35.4	34.1	-19.9	-18.7	-1.0
G2-A 3 Bay	35.1	34.1	-19.8	-18.7	-1.2

A convergence study was conducted to determine the appropriate mesh dimensions for the finite element model. Three different element sizes with edge lengths of 100 mm, 50 mm, and 25 mm were analyzed using a non-linear buckling analysis. The results of the convergence study are provided in Table 5.3. A mesh with a 50 mm edge length is shown to provide sufficient accuracy and computational efficiency.

Table 5.3: Mesh convergence study results

Model	Mesh Size (mm)	Buckling Factor, λ	% Difference	Computation Time
G1-A	100	4.919	-	7 Min, 4 sec
G1-A	50	4.902	0.34	32 Min, 38 Sec
G1-A	25	4.896	0.12	7 Hr, 03 Min
G2-A	100	3.541	-	4 Min, 26 Sec
G2-A	50	3.535	0.17	18 Min, 32 Sec
G2-A	25	3.532	0.12	3 Hr, 43 Min

The girder finite element models were constructed using shell elements for the webs, flanges, and stiffeners. A node was located at the centroidal intersections between webs and flanges so that the two planes could be meshed and so the vertical distance between top and bottom flanges could be maintained. This resulted in the web extending into the top and bottom flanges by half of the thickness of each flange. The relative area of the overlap compared to the overall area of the cross section is small and does not have an appreciable impact on the analysis. Figures 5.4 and 5.5 summarize the discretization of the cross section as well as the stiffening and bracing elements for G1. Figures 5.6 and 5.7 summarize the finite element discretization for G2.

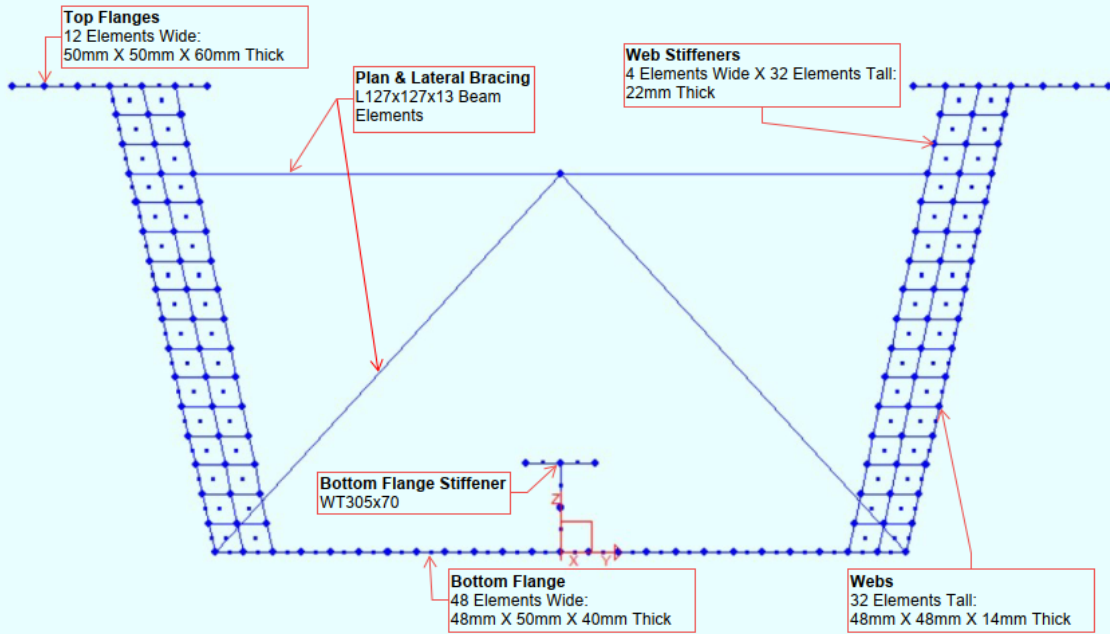


Figure 5.4: G1 model discretization (cross section)

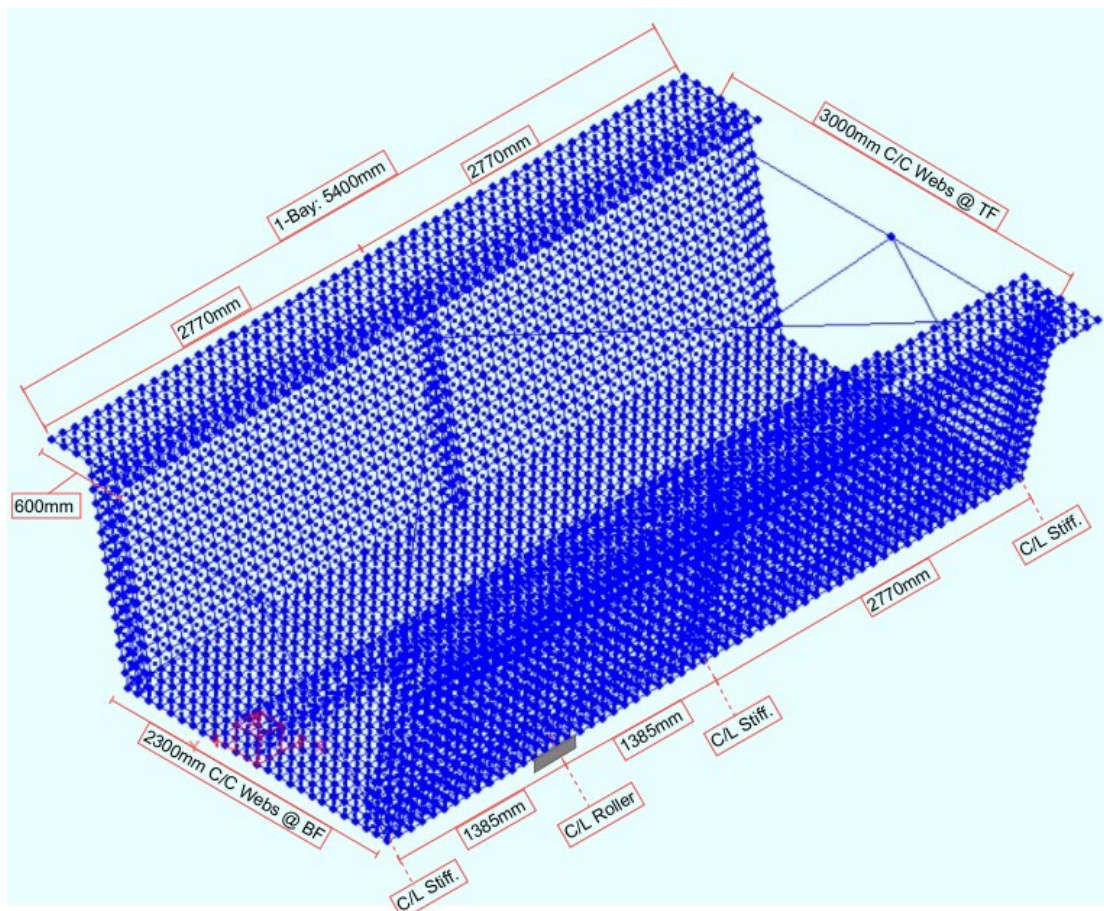


Figure 5.5: G1 model discretization (isometric view)

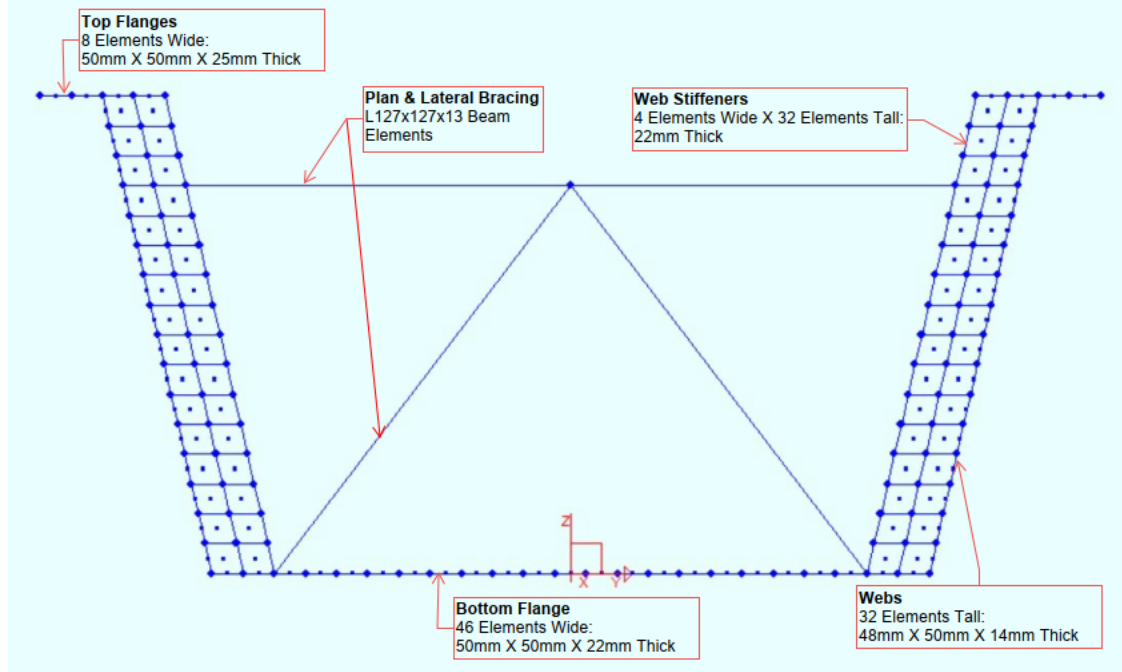


Figure 5.6: G2 model discretization (cross section)

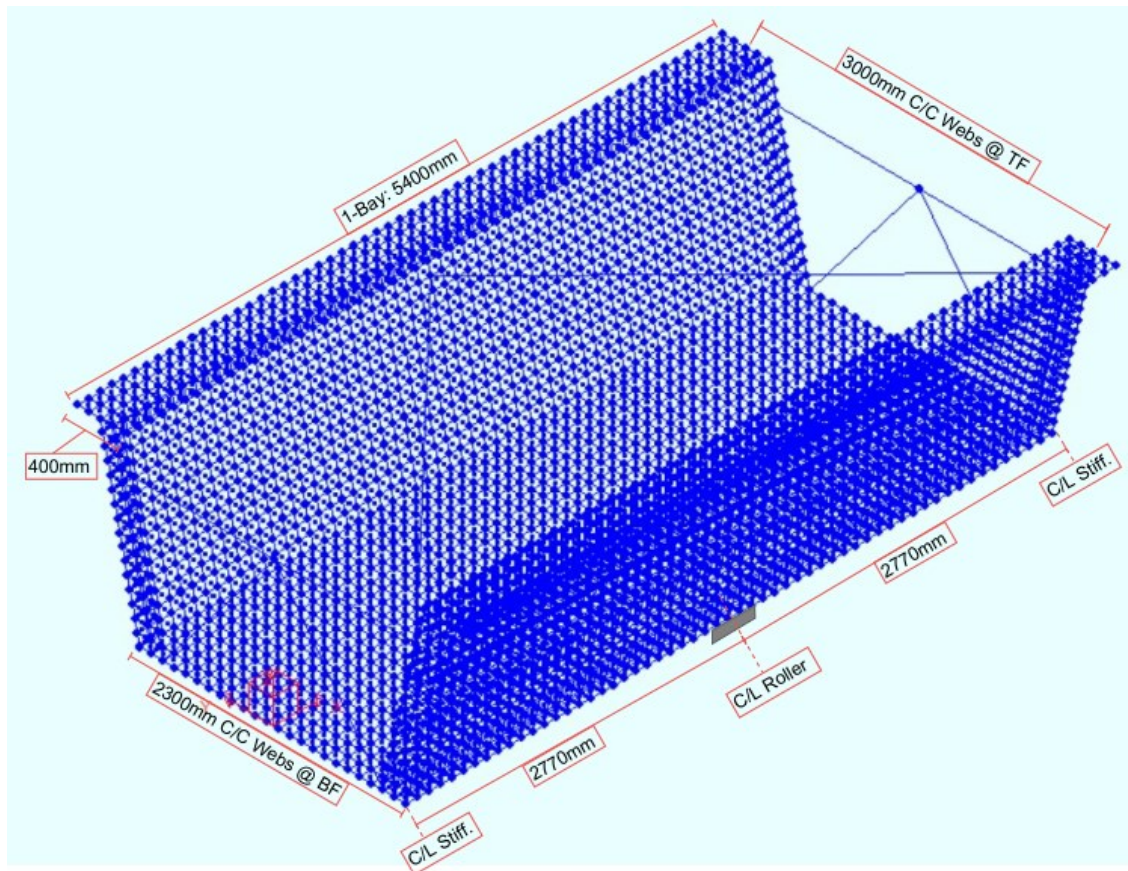


Figure 5.7: G2 model discretization (isometric view)

5.5 Initial Web Geometric Imperfections

The initial web out-of-flatness was considered in the analysis by incorporating a scaled first buckled mode shape into the finite element model. Figure 5.8 below shows an example of the first buckled web mode shape for G1.

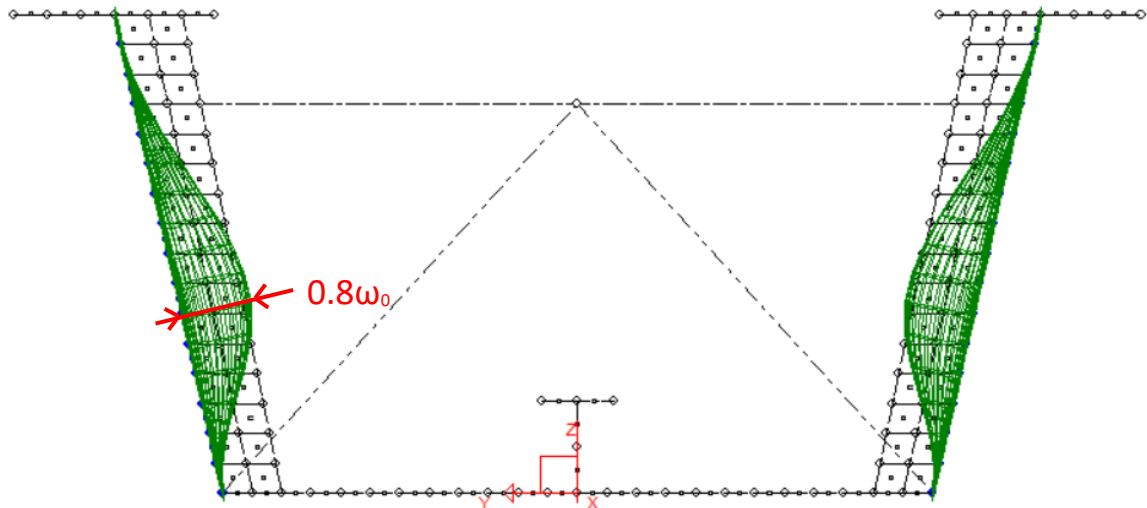


Figure 5.8: Initial web out-of-straightness shape (G1 cross section shown, G2 similar)

The maximum permissible deviation from flatness, ω_0 , for girders with intermediate stiffeners on one side of the web is given by Table J.5(a) of CSA W59 (2018). For webs having a thickness of 14 mm and a ‘least panel dimension’ of 1500 mm (i.e., lesser of the web height or stiffener spacing), ω_0 is specified as 10 mm. Annex C.5 of Eurocode (2006) suggests that the amplitude of the initial geometric imperfections be equal to 80% of the maximum fabrication tolerance. It should be noted that only the maximum out-of-flatness at the centerline of each panel (i.e., one vertical plane) was measured to be 6 mm for both G1 and G2. But the web out-of-flatness profile for the entire panel was not measured. Since the entire panel was not measured, it was decided to apply a maximum out-of-flatness of 8 mm to the G1-A and G2-A numerical models to be consistent with the limits from CSA W59 (2018) and the guidance provided by Annex C.5 of Eurocode (2006).

The general process used to create a numerical model with an initial geometric imperfection involved first running a linear buckling analysis to determine the first buckled mode shape. The buckled geometry of the webs was then scaled to achieve a maximum

amplitude of $0.8 \omega_0$, as shown in Figure 5.8 above, and saved as the initial model geometry.

5.6 Boundary Conditions & Load Application

Loads and boundary conditions were applied in the models to simulate an isolated girder segment on launching rollers. Loads were applied such that static equilibrium was maintained about the centerline of the rollers. Vertical reactions from the rollers were applied as point loads at the centerline of the webs. Weak translational springs were provided at the ends of the models, at the flange-to-web junctions, to ensure overall model stability. The springs were also used to check for residual reactions at the ends of the girder. Reactions at the springs would indicate excessive warping of the cross section and an error in the model.

To simulate the bending and shear load effects at the critical section (i.e., at the centerline of the roller), the equivalent static internal loads were calculated at the ends of the one-bay girder segment. Figure 5.9 depicts an example of the typical loading condition applied at one end of the numerical models. Bending stresses were converted to axial forces and applied to the top and bottom flanges to produce tensile stresses in the top flanges and compressive stresses in the bottom flange. Shear forces were applied as vertical point loads acting along the webs.

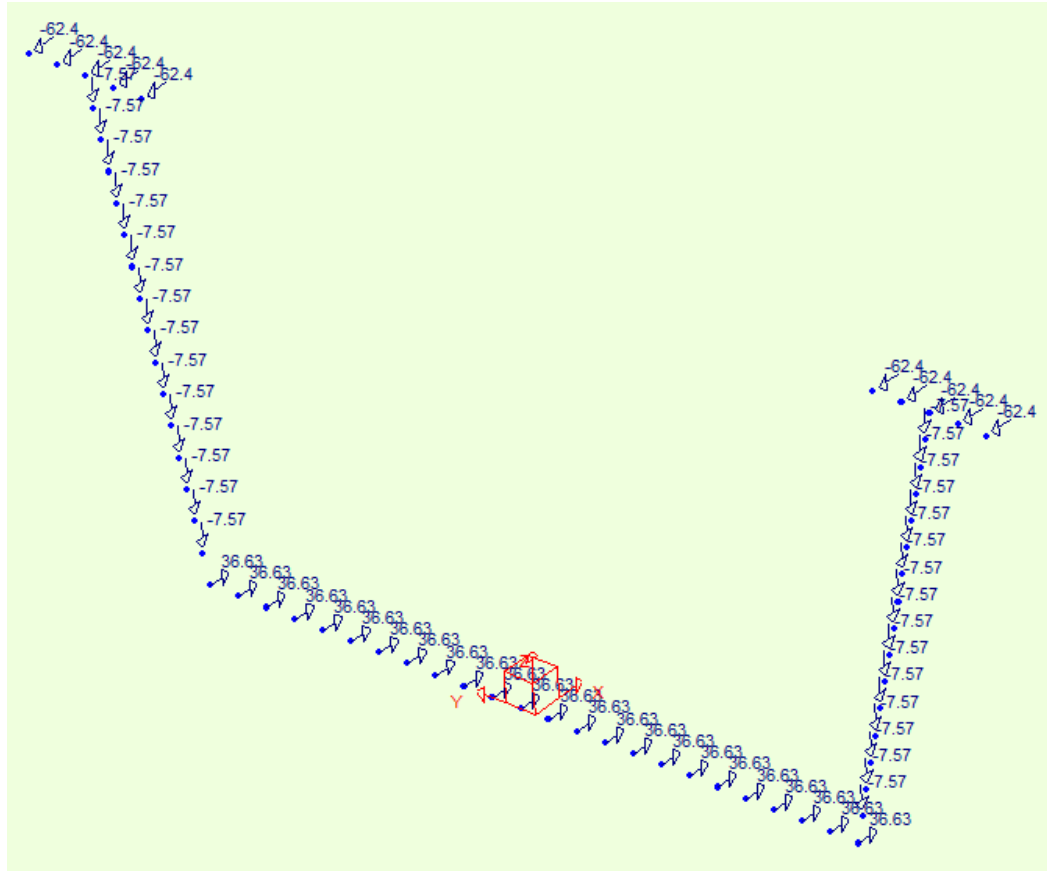


Figure 5.9: Example of the loads applied to the cross section

5.7 Nonlinear Buckling Analysis

S-FRAME's nonlinear buckling analysis is a hybrid of nonlinear static and traditional linear buckling analyses. First, a nonlinear static analysis is performed where the applied load is divided into increments and as each load increment is applied, the geometry and internal stress state is updated. Then, the buckling analysis is performed which computes the buckling load factor (eigenvalue) and corresponding mode shape (eigenvector).

The lowest eigenvalue returned from the buckling analysis is obtained and assessed. If the value is less than 1.0, the girder will buckle under the current applied loading. If the eigenvalue is greater than 1.0, the applied loading would need to be scaled by the obtained eigenvalue in order to reach a buckled state. For the purposes of this research, the applied loading was multiplied by the eigenvalue, λ , and the resulting web stress at the critical

buckling height, H_{cr} , was taken as the critical buckling stress, σ_{cr} .

5.8 Verification of the Finite Element Model

As mentioned previously, the experimental results cannot be fully relied upon for verification of the numerical model due to erroneous readings. Some attempts were still made to compare web stresses from the FE model results with some experimental readings for completeness of the study. This comparison is presented in Section 5.8.2. Additionally, the verification of the numerical model was conducted by comparing results of FE models with longitudinal flange stresses calculated using classic beam theory (Section 5.8.1) and with experimental results from available literature (Section 5.8.3).

5.8.1 Verification of G1 and G2 Flange Stresses

The longitudinal top and bottom flange stress results from the FE models were compared with those obtained from classical beam theory. Figures 5.10 and 5.11 show the stress distribution in girder segments G1-A and G2-A respectively. Flange stress results from G2-C and G2-D are similar to G2-A.

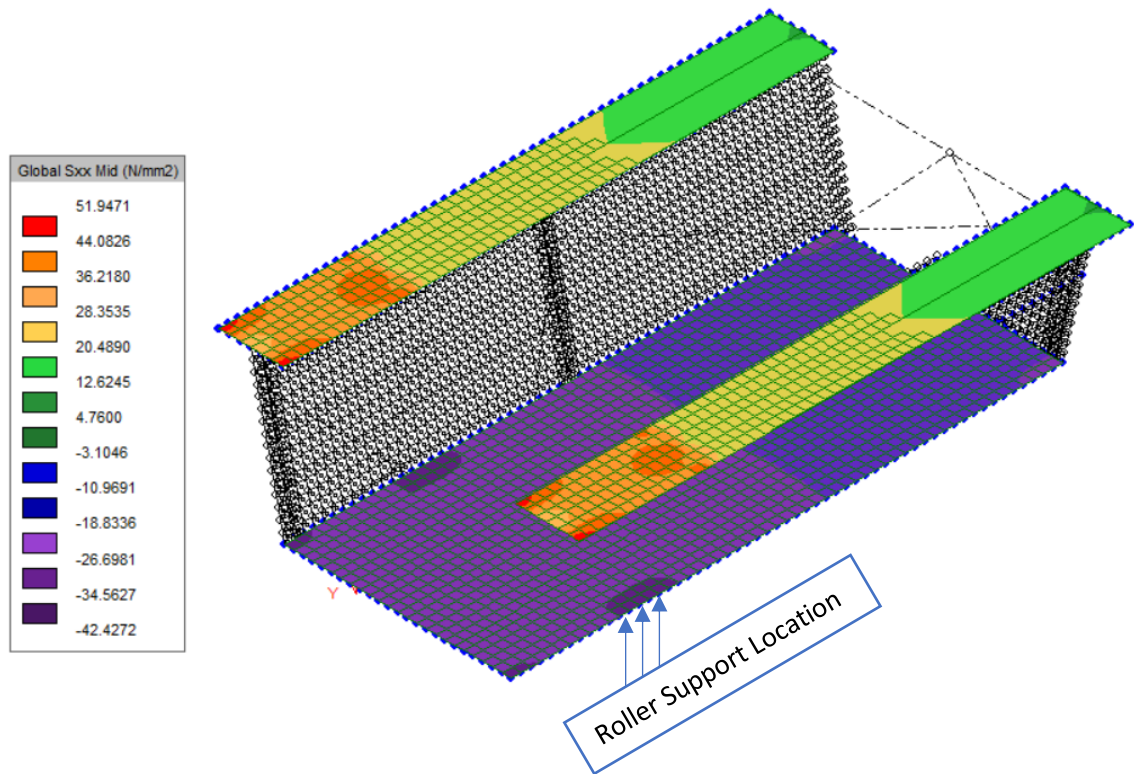


Figure 5.10: G1-A flange stresses

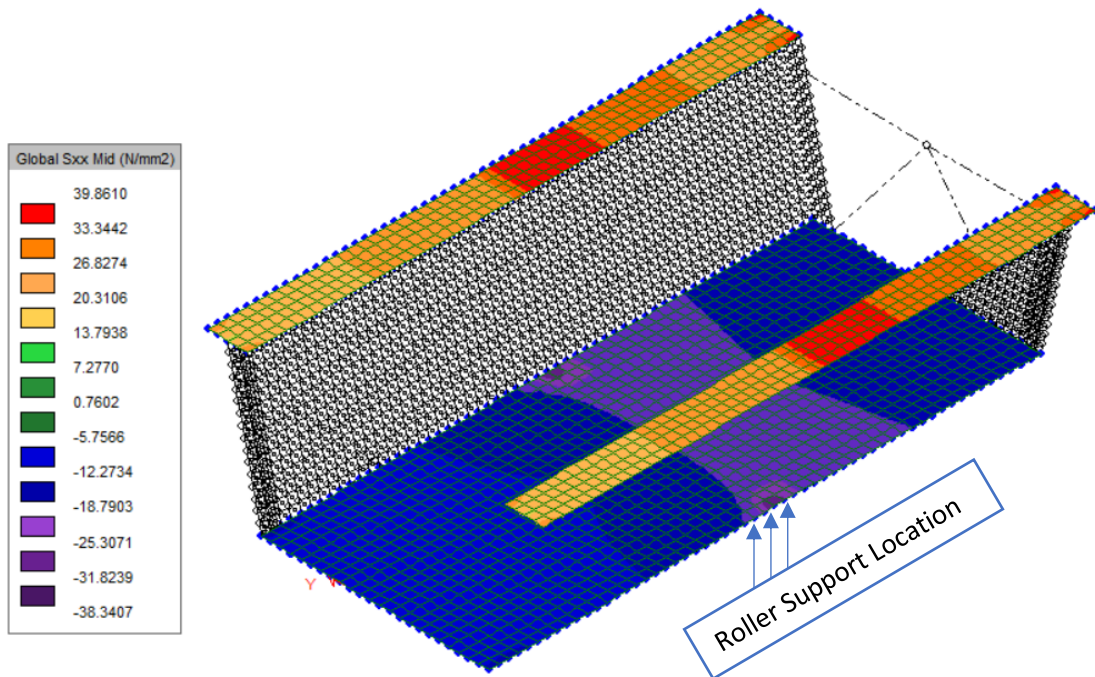


Figure 5.11: G2 flange stresses (G2-A shown, G2-C and G2-D stresses similar)

Table 5.4 summarizes the flange stresses at the location above centerline of the roller support from the finite element models as well as the theoretical stresses. As shown, there is good agreement between the theoretical and results from the models. The flange stresses from the numerical models are within 5% of the theoretical values, except for the G1-A bottom flange stress which showed a difference of 8.3%.

Table 5.4: Comparison of flange stresses between numerical and theoretical models

Model ID	Theoretical Top Flange Stress (MPa)	FE Top Flange Stress (MPa)	% Diff.	Theoretical Bottom Flange Stress (MPa)	FE Bottom Flange Stress (MPa)	% Diff.
G1-A	43	42.2	1.9	-36	-33.1	8.3
G2-A	34	35.4	4.0	-19	-19.9	4.6
G2-C	34	34.4	1.2	-19	18.6	2.1
G2-D	34	34.3	1.0	-19	18.3	3.8

5.8.2 Comparison of the Experimental Versus FE Web Stresses

Although the experimentally measured stresses were deemed not fully reliable, it is still felt a worthwhile exercise to show the comparison of experimental and numerical results for the completeness of this study. This exercise was conducted with experimental results of G2-A and G2-D. Figures 5.12 and 5.13 show comparisons of the experimental and numerical longitudinal and vertical web stresses of G2-A and G2-D respectively where the left portion of each figure presents the longitudinal stress distribution, and the right portion shows the vertical stress distribution. The figures depict a localized segment of the web, taken directly over the roller from FE models. These stresses were taken at the mid-plane of the web and are represented by the coloured contours. The values in the red boxes are the experimentally obtained results, averaged between the inside and outside faces of the web.

The following observations can be made from the G2-A web stress data presented in Figure 5.12. For the longitudinal stresses, the difference in stress between the FE model and the experimental data at the lowest row of data points is approximately 5 MPa. Both

FE and experimental results indicate compressive stress at this location. The difference in stress between the model and experimental data along the middle row of data points ranges from 3 MPa to approximately 10 MPa. The stress predicted by the FE model at the upper row of data points is 9 MPa and the experimentally obtained value is 15 MPa, resulting in a difference of 6 MPa. Both FE and experimental results indicate tensile stress at this location. For the vertical stresses, the difference between numerical and experimental values are generally within 8 MPa of each other. The stress orientations are in agreement for the lowest and middle rows. The trend where compressive stresses are present at the lowest extreme of the web and tensile stresses are present at the upper regions of the web is apparent.

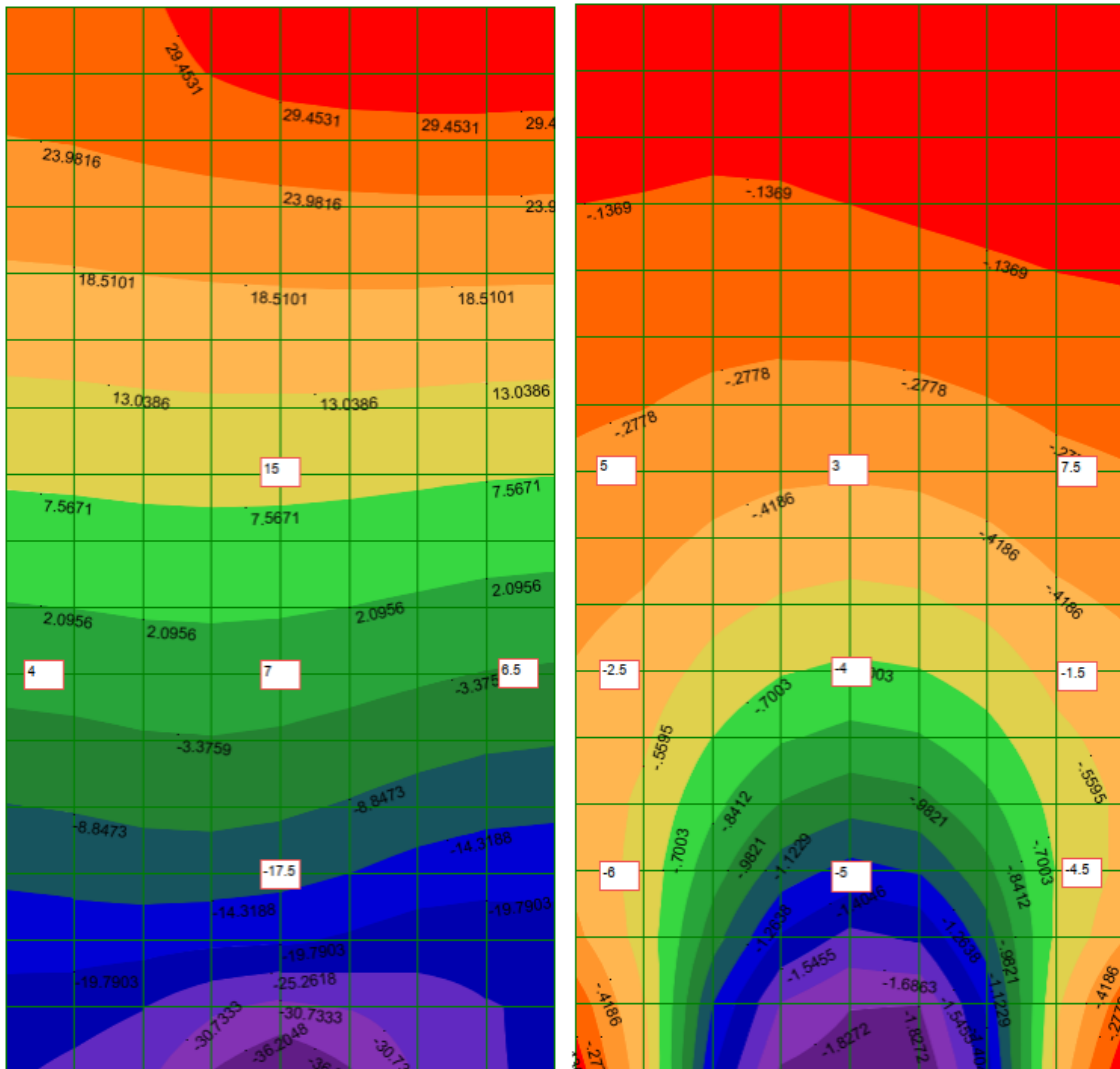


Figure 5.12: G2-A longitudinal (left) and vertical (right) web stresses

The following observations can be made from the G2-D web stress data presented in Figure 5.13. For the longitudinal stresses, the difference in stress between the FE model and the experimental data at the lowest row of data points is approximately 13 MPa. Good agreement is observed between the FE and experimental results at the middle row of data points with a maximum difference of 1.5 MPa. The difference in stress between the FE model and the experimental data at the lowest row of data points is approximately 9 MPa. For the vertical stresses, the differences between the FE and experimental results are all within approximately 4 MPa of each other with the exception of two outliers in the lowest row. In general, although some data points show very good agreement between the FE and experimental results, some data points show fair-to-poor results.

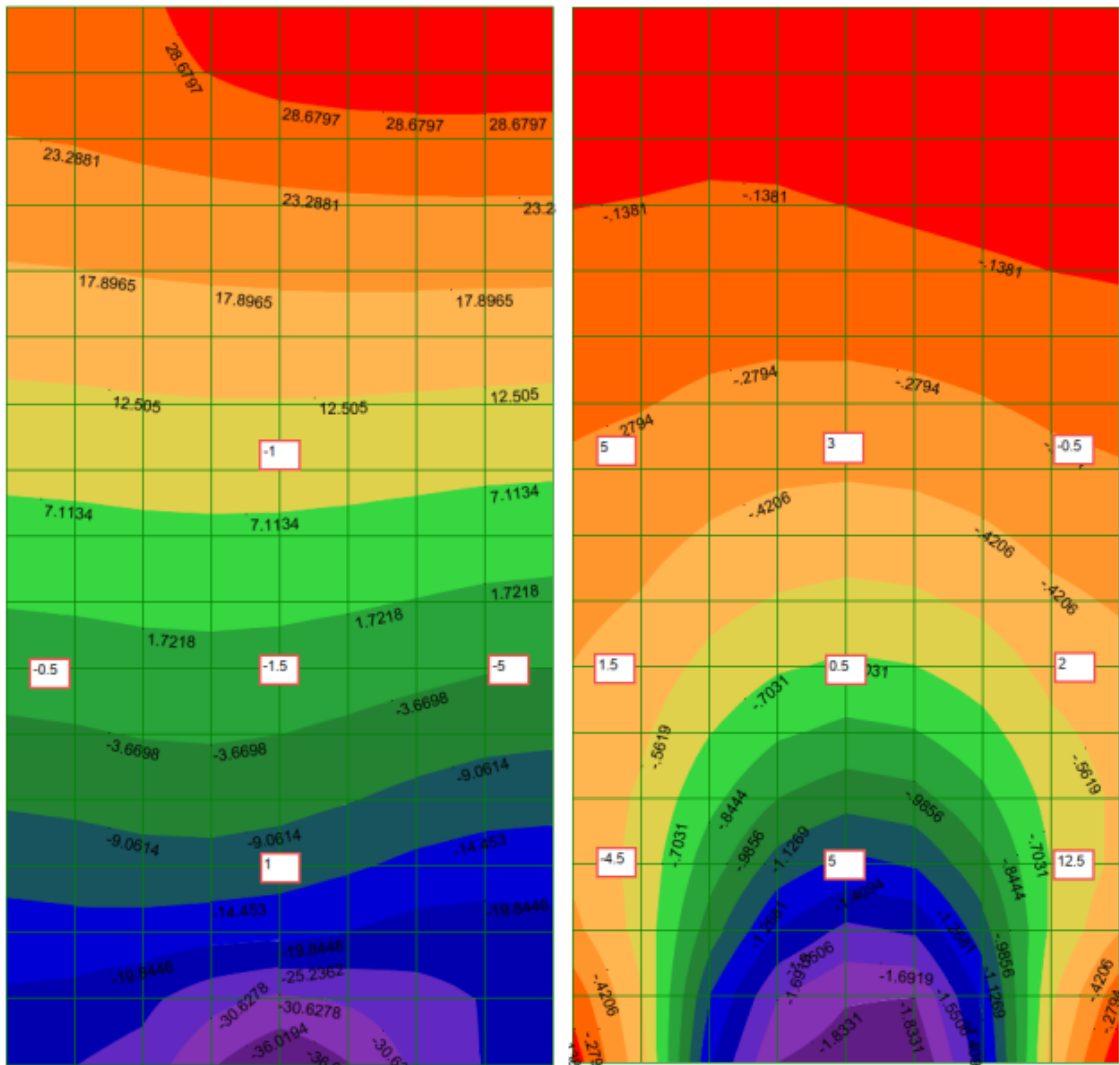


Figure 5.13: G2-D longitudinal (left) and vertical (right) web stresses

5.8.3 Verification of the Plate Girder Model from Literature

The results of linear buckling analyses of three plate girders from the literature were replicated in order to develop confidence in the box girder models and S-FRAME's analysis capabilities. The work of Granath et al. (1999) (see Chapter 2) was used to further verify the model. A brief summary of salient information of the work by Granath et al. (1999) is provided here for ease of reference.

The three girder specimens examined by Granath et al. consisted of all I-shaped sections subjected to patch loading. The test set up used is shown in Figure 5.14. The geometric and material properties of the three specimens are presented in Table 5.5 below where f_{yw} and f_{yf} refer to the yield stress of the web and flange respectively. The vertical stiffener spacing, a , varied from 1008 mm to 1626 mm.

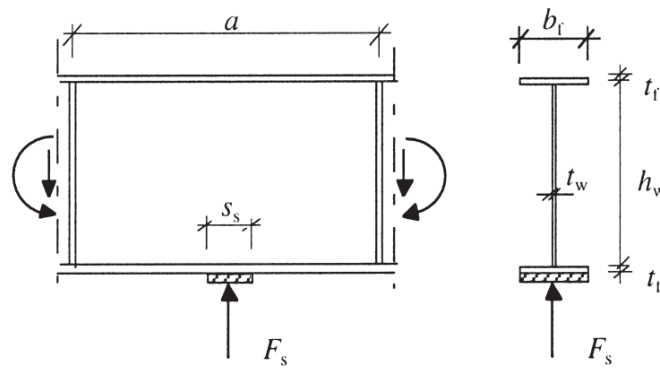


Figure 5.14: Test set up by Granath et al. (1999)

Table 5.5: Relevant properties of girder specimens tested by Granath et al. (1999)

Girder ID	h_w (mm)	t_w (mm)	f_{yw} (MPa)	b_f (mm)	t_f (mm)	f_{yf} (MPa)	a (mm)
A13p	239.8	3.8	830	118.5	12	844	1008
A61p	439.9	3.8	830	120.0	12	844	1626
A71p	320.7	7.9	762	120.5	11.9	844	1405

An example of the stress distribution from the S-Frame model for specimen A61p is shown in Figure 5.15. The critical buckling heights, H_{cr} , measured from the bottom edge of the web, and stresses obtained from the finite element models are compared with those presented by Granath et al. (1999) in Table 5.6.

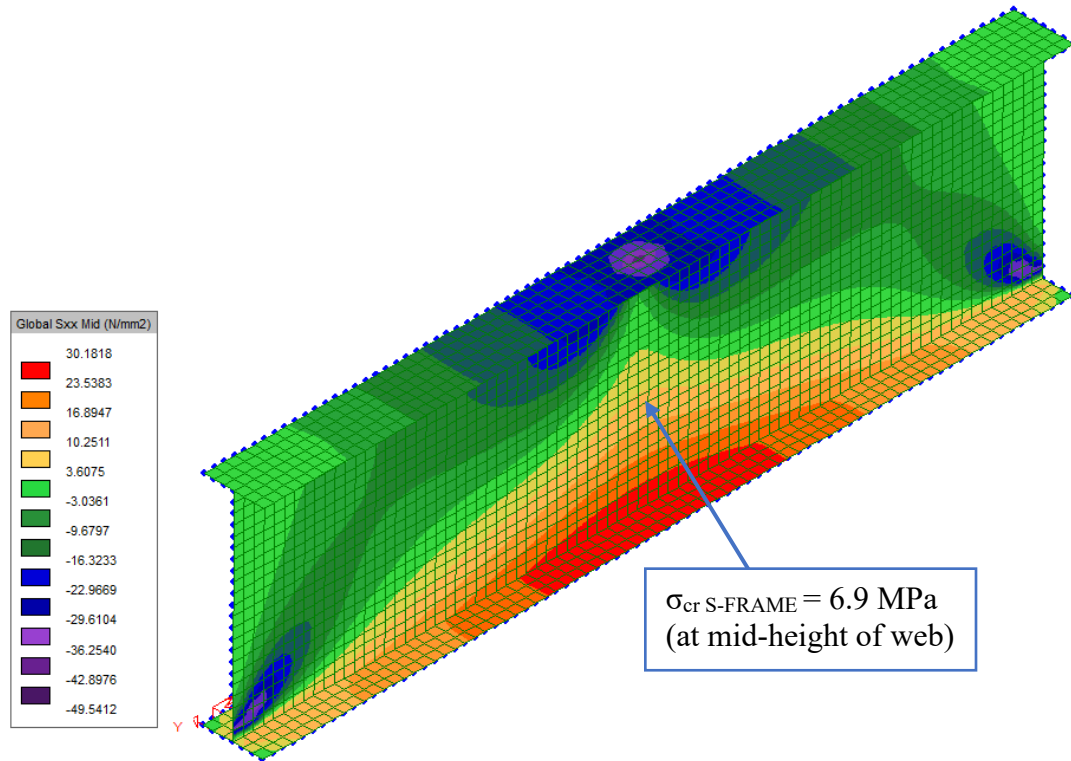


Figure 5.15: Example of the critical web buckling stress (specimen A61p shown)

Table 5.6: Comparison of FE results with specimens from Granath et al. (1999)

Girder ID	H_{cr} Granath (mm)	H_{cr} S-FRAME (mm)	σ_{cr} Granath (MPa)	σ_{cr} S-FRAME (MPa)	% Diff. σ_{cr}
A13p	100	110	15.0	14.8	2
A61p	200	220	7.2	6.9	5
A71p	160	180	44.7	43.9	2

As shown in Table 5.6, good agreement is observed between the results obtained by S-FRAME and those presented by Granath et al (1999). The maximum difference in critical stress was 5% with models A13p and A71p showing results within 2% of each other. The result of this comparative study demonstrates that the model developed using S-FRAME can predict the critical elastic buckling capacity of plate girders with an acceptable level of error.

Granath et al. (1999) classified A71p as a stocky web, A61p as a slender web, and A13p as having a web with intermediate slenderness. The authors demonstrated that the failure mode of the stocky web (A71p) was by web yielding, and the failure mode of the other two girders was by buckling. The authors did not distinguish between web panel buckling or

web crippling, but the progression of failure described by Granath et al. (1999) indicates the failure mode of A13p was by web crippling and A61p was by web panel buckling. P_{cr} is compared to the web yielding resistance, B_{ry} (Eqn. [2.31]), and crippling resistance, B_{rc} (Eqn. [2.32]), in Table 5.7. As shown in the table, the failure modes described by Granath et al. (1999) appear to be accurate as B_{ry} is the limiting value for A71p and P_{cr} is the limiting value for A61p. Although the FE model predicts that web panel buckling would be the failure mode for A13p ($P_{cr} = 159$ kN), the value for web crippling is similar ($B_{rc} = 175$ kN) and therefore the failure mode could be by either panel buckling or crippling. It should be noted that Φ_{bi} was set to 1.0 in equations [2.31] and [2.32].

Table 5.7: Comparison of the critical buckling load to the web yielding and crippling resistances

Girder ID	P_{cr} Granath & S-FRAME (kN)	B_{ry} (kN) Eqn. [2.31]	B_{rc} (kN) Eqn. [2.32]
A13p	159	213	175
A61p	85	213	175
A71p	811	440	757

5.9 Summary

In this chapter, a numerical model using the finite element method was developed to simulate the behaviour of steel trapezoidal box girders subjected to bending moments and concentrated vertical patch loads. The finite element analysis program capabilities and subsequently, the girder models, were verified using classical beam theory, experimental results from this study and experimental results from literature. It is unfortunate that the experimental results from this study did not provide conclusive verification of the FE model. The comparison of the model against the classical beam theory and results from literature showed the developed model can predict the stress and buckling load accurately.

CHAPTER 6 PARAMETRIC STUDY

6.1 General

A study of various parameters affecting the behaviour and capacity of box girder web panels subjected to both bending moment and patch load was conducted, and the results are presented in this chapter. The numerical models described in Chapter 5 were used in this parametric study. The parameters investigated included the thickness of the box girder webs, the height of the webs, the inclination of the webs, the transverse stiffener spacing, the bottom flange and top flange thicknesses, and the influence of weld induced residual stress. In total, 104 finite element models were analyzed as part of this parametric study. The chapter concludes by comparing the FE results to current code practice where appropriate.

6.1.1 Girder Geometry Development and Applied Loading

The Shubenacadie River Bridge box girders were designed to minimize the overall girder depth to facilitate the approach grades and other existing site conditions. As a result, the geometry of those girders is not exactly representative of typical box girder geometry for bridges with similar spans. In other words, the Shubenacadie River girders are relatively shallow with thick flanges whereas bridges with similar spans would typically have deeper girders with thinner flanges. As the main purpose of this research was to develop a general understanding of the behaviour of full-scale steel box girder webs encountered in practice, a survey of recently erected (within approximately 10 years) steel box girders using the incremental launching method in Atlantic Canada was conducted. The geometry of these bridge girders is presented Table 6.1 with the symbols defined in Figure 6.1. Representative models used in the parametric study were derived from the geometric envelope of these girders. In Table 6.1, “a” refers to the longitudinal distance between transverse web stiffeners.

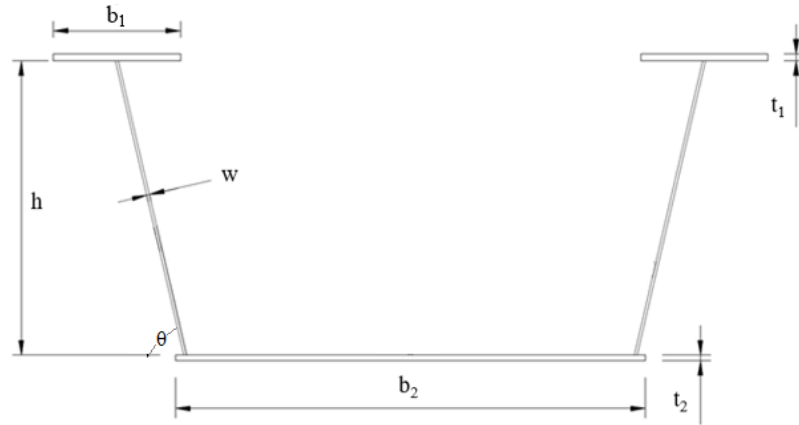


Figure 6.1: Box girder geometric schematic

Table 6.1: Summary of girders used to create the parametric study envelope

Girder & Section	b₁ (mm)	t₁ (mm)	b₂ (mm)	t₂ (mm)	h (mm)	w (mm)	h/w	θ (°)	a (mm)	a/h
Shubenacadie River Bridge – A										
	400	25	2300	22	1500	14	107	79	5540	3.7
Shubenacadie River Bridge – B										
	650	60	2300	45	1500	14	107	79	2770	1.9
South River Bridge – 1										
	500	25	2300	20	2400	16	150	82	6500	2.7
South River Bridge – 11										
	800	60	2300	45	2400	16	150	82	3305	1.4
West River Bridge – A										
	550	30	2250	22	1900	14	136	79	3120	1.6
West River Bridge – B										
	550	45	2250	30	1900	14	136	79	6240	3.3
Indian Sluice Bridge – B										
	400	25	2080	22	2100	14	150	86	5180	2.5
Indian Sluice Bridge – D										
	600	60	2080	38	2100	14	150	86	2500	1.2
Sydney River Pedestrian Bridge – B										
	500	30	2150	20	2100	14	150	85	5715	2.7
Sydney River Pedestrian Bridge – D										
	500	50	2150	30	2100	14	150	85	5715	2.7
Sydney River Bridge – A										
	600	30	2850	25	2300	16	144	77	5415	2.4
Sydney River Bridge - B										
	900	60	2850	45	2300	16	144	77	2710	1.2
Max	900	60	2850	45	2400	16	150	86	6500	3.7
Min	400	25	2080	20	1500	14	107	77	2500	1.2

In this parametric study, the bending moment and patch load applied to the finite element models corresponded to the loads generated by the steel self-weight condition of a 20 m long launch cantilever and 20 m long back span. The applied bending moment at the critical section was 3500 kN-m and the corresponding reaction (patch load) at the roller support was 700 kN, or 350 kN per web.

The critical buckling stresses presented herein were calculated using the eigenvalue method. A step-by-step example of the process used to calculate the critical buckling stresses from the FE models is included in Appendix C.

6.1.2 Finite Element Model Characteristics

Similar to the finite element models described in Chapter 5, all finite element models developed for the parametric study utilized approximately 50 mm by 50 mm shell elements. A linear elastic material model was used for the steel girders with a yield strength $F_y = 350$ MPa, elastic modulus $E = 200\,000$ MPa and Poisson's ratio of 0.3.

Global load effects were applied to an isolated, one-bay, girder FE model segment. The shear force at each end of the isolated segment was applied to the girder webs and the bending moment was resolved to axial forces applied at the top and bottom flanges. The patch load (roller reaction) was applied vertically below the bottom flange and was 400 mm long. The FE model did not provide longitudinal or transverse restraint from the roller to the girder bottom flange.

The width of the top flanges, b_1 , was 550 mm and the width of the bottom flange, b_2 , was 2300 mm in all FE models of this parametric study. In addition, unless otherwise noted (see Section 6.5), the thicknesses used for the top flange, t_1 , and bottom flange, t_2 , were 42 mm and 30 mm respectively. A WT section (WT 305x70) was used in all models to prevent bottom flange buckling and 'force' the web elements to buckle before the bottom flange. The presence of a bottom flange stiffener is common in practice, especially near negative moment regions, and therefore bottom flanges are generally sufficiently stiffened to resist compressive stresses encountered during girder launching situations.

6.2 Effect of Web Thickness

In this section, the effect of varying the girder web thickness, w , from 10 mm to 16 mm was studied. The associated panel slenderness ratio, h/w , was also varied by virtue of changing w . A typical range of web thicknesses from the bridge girders presented in Table 6.1 is 14 to 16 mm. However, CSA S6 (2019) permits girder webs to be as thin as 10 mm. Therefore, four finite element models were created with the geometries presented in Table 6.2, noting that all other geometric properties were kept constant while the web thickness varied. The buckling stress, σ_{cr} , and the buckling patch load, P_{cr} , obtained from the finite element analysis are also presented in Table 6.2.

Table 6.2: Geometric properties & FE results per web; effect of web thickness

Model #	h (mm)	w (mm)	θ (°)	h/w	a (mm)	a/h	FE Results	
							σ_{cr} (MPa)	P_{cr} (kN)
A1	2075	10	83	209	5760	2.8	3.5	618
A2	2075	12	83	174	5760	2.8	7.3	1026
A3	2075	14	83	149	5760	2.8	13.8	1684
A4	2075	16	83	131	5760	2.8	32.3	3887

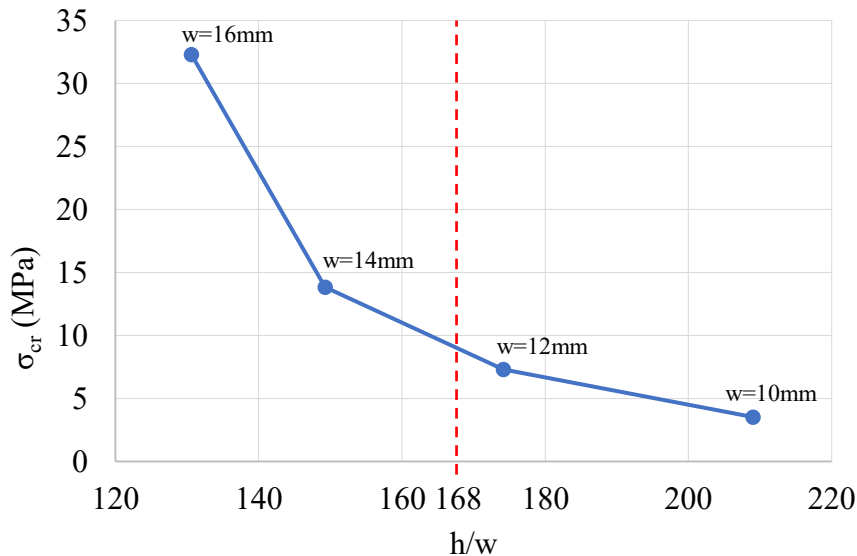


Figure 6.2: Critical buckling stress versus web panel slenderness for web thicknesses of 10mm to 16mm

Figure 6.2 plots the critical buckling stress versus web slenderness ratio h/w , as the web thickness varies from 10 to 16 mm. It shows that as the web slenderness increases, i.e. as the web becomes thinner, the critical buckling stress decreases, however, with a diminishing rate. It shows that the change in critical buckling stress is greatest between the 16 mm and 14 mm thick web cases (with a rate of reduction of 103%) and less drastic between the 12 mm and 10 mm thick web cases (with a rate of reduction of 11%). CSA S6 (2019) permits web slenderness ratios up to 168, as referenced by the vertical red dashed line in Figure 6.2. The code maximum was developed from fatigue testing on beams with unstiffened webs and the limit was set to prevent fatigue cracking in the flange-to-web welds. For webs under flexural compression, the h/w limit for a Class three web is set to be 102 (CSA S6, 2019). As shown in Tables 6.1 and 6.2, the slenderness ratio is commonly larger than 102. Therefore, local buckling of the cross section would be expected and this is evidenced by the relatively low values of critical buckling stresses in Table 6.2. It should be noted that the panel width and height for this series of models were 5760 mm and 2075 mm respectively, which represent a relatively large unstiffened panel.

6.3 Effect of Web Height

The effect of varying the girder web height is studied in this section. Web heights of 1500 to 3000 mm, increasing in 500 mm increments, were modelled while keeping the other geometric properties constant. For each web thickness of 10 to 16 mm studied in the previous section, four web heights were studied. As a result, 16 finite element models were created with the geometries presented in Table 6.3, along with the buckling stress, σ_{cr} , and the buckling patch load, P_{cr} , obtained from the finite element analysis.

Table 6.3: Geometric properties and FE results per web; effect of web height

Model #	h (mm)	w (mm)	θ (°)	h/w	a (mm)	a/h	FE Results	
							σ_{cr} (MPa)	P_{cr} (kN)
B1.1	1500	10	80	152	5760	3.8	8.6	840
B1.2	2000	10	80	203	5760	2.8	4.4	622
B1.3	2500	10	80	253	5760	2.3	1.4	496
B1.4	3000	10	80	304	5760	1.9	1.5	415
B2.1	1500	12	80	127	5760	3.8	12.2	1435
B2.2	2000	12	80	169	5760	2.8	8.8	1035
B2.3	2500	12	80	211	5760	2.3	7.0	821
B2.4	3000	12	80	253	5760	1.9	6.2	675
B3.1	1500	14	80	109	5760	3.8	23.1	2066
B3.2	2000	14	80	145	5760	2.8	15.3	1551
B3.3	2500	14	80	181	5760	2.3	12.0	1206
B3.4	3000	14	80	217	5760	1.9	11.5	1011
B4.1	1500	16	80	95	5760	3.8	45.5	2836
B4.2	2000	16	80	127	5760	2.8	35.3	2243
B4.3	2500	16	80	158	5760	2.3	26.3	1715
B4.4	3000	16	80	190	5760	1.9	22.5	1410

Series B model results are shown in Figure 6.3 where the critical buckling stress versus the web slenderness ratio is plotted for each web thickness. In general, it shows that an increase in h/w, due to an increase in the web height, also results in a decrease in the critical buckling stress. Regardless of the source of the h/w increase, whether it be the reduction in the web thickness or an increase in the web height, the greater the h/w, the lower the critical buckling stress. Also as similarly observed in the previous section, the rate of decrease is not linear; the rate of reduction becomes less pronounced as the web slenderness shifts to a high value region. This observation underscores that the web slenderness ratio h/w, as opposed to web thickness or web height alone, captures the influence of the geometric properties on buckling stress. It is interesting to note, however, that for a given h/w ratio, the thicker web results in higher critical buckling stress. In other words, when h/w is equivalent between webs of different thicknesses, the thicker web carries a higher buckling stress.

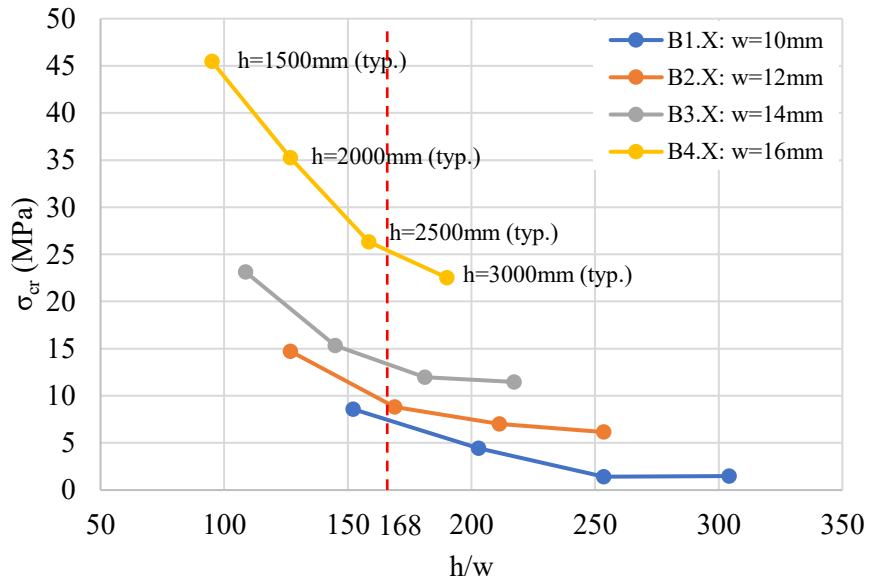


Figure 6.3: Critical buckling stress versus web panel slenderness for web heights of 1500mm to 3000mm

6.4 Effect of Web Inclination

In this section, the effect of varying the girder web inclination is assessed. Previous research on plate girders is limited to the case where the girder webs are vertical. Since trapezoidal box girders have inclined webs, the effect of web inclination is assessed in this section. In this study, the angle of the web, θ , is measured relative to the horizontal axis so that a web inclination of 90° indicates the web is vertical. Five angles of web inclination were studied corresponding to web slopes presented in Table 6.4. CSA S6 (2019) does not allow webs to be sloped less than 4:1 (or 76°) to limit out-of-plane bending of box girder web plates. In order to encompass this limit, the maximum slope considered in the study was 3:1 (or 72°) and used as the lower bound for the data set.

Table 6.4: Web inclination and corresponding slope

Model #	Web Inclination (°)	Web Slope (Vertical:Horizontal)
C1.X	90	-
C2.X	85	12:1
C3.X	80	6:1
C4.X	76	4:1
C5.X	72	3:1

Similar to Series A and B data sets, each slope was modelled using four web thicknesses and a web height of 2500 mm was considered, resulting in 20 FE models for this series. Table 6.5 presents the girder geometries included in this portion of the parametric study as well as the FE results.

Table 6.5: Geometric properties and FE results per web; effect of web inclination

Model #	h (mm)	w (mm)	θ (°)	h/w	a (mm)	a/h	FE Results	
							σ_{cr} (MPa)	P_{cr} (kN)
C1.1	2500	10	90	250	5760	2.3	3.0	521
C2.1	2500	10	85	251	5760	2.3	2.9	516
C3.1	2500	10	80	254	5760	2.3	2.9	503
C4.1	2500	10	76	258	5760	2.2	2.8	487
C5.1	2500	10	72	263	5760	2.2	2.7	467
C1.2	2500	12	90	208	5760	2.3	10.4	860
C2.2	2500	12	85	209	5760	2.3	9.7	852
C3.2	2500	12	80	212	5760	2.3	8.6	830
C4.2	2500	12	76	215	5760	2.2	8.0	804
C5.2	2500	12	72	219	5760	2.2	7.1	771
C1.3	2500	14	90	179	5760	2.3	17.3	1291
C2.3	2500	14	85	179	5760	2.3	15.3	1277
C3.3	2500	14	80	181	5760	2.3	13.2	1245
C4.3	2500	14	76	184	5760	2.2	12.8	1205
C5.3	2500	14	72	188	5760	2.2	12.0	1156
C1.4	2500	16	90	156	5760	2.3	24.0	1803
C2.4	2500	16	85	157	5760	2.3	22.0	1781
C3.4	2500	16	80	159	5760	2.3	20.0	1734
C4.4	2500	16	76	161	5760	2.2	18.9	1678
C5.4	2500	16	72	164	5760	2.2	18.1	1609

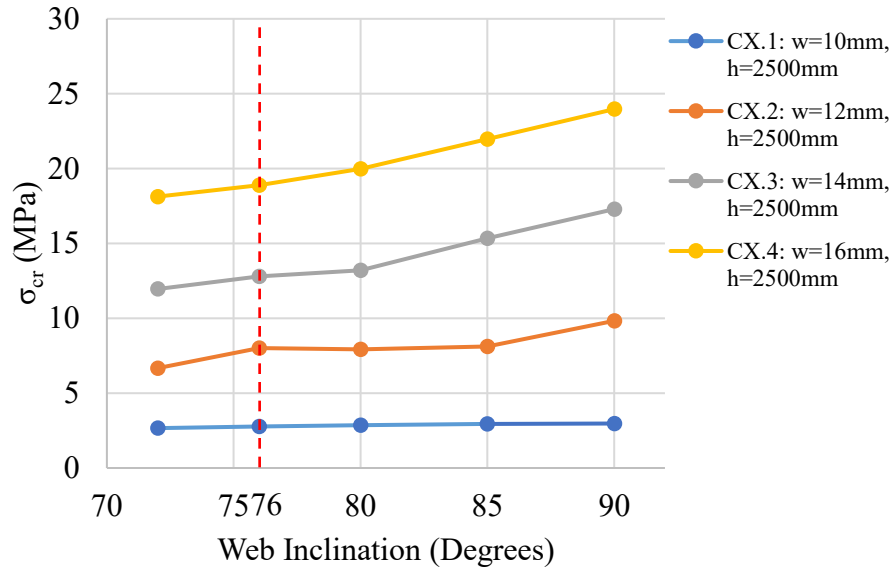


Figure 6.4: Critical buckling stress versus web inclination

The critical buckling stress versus the web inclination is presented in Figure 6.4 for four web thicknesses. The CSA S6 (2019) limit of 76° is represented by the vertical red dashed line where values to the left of the line are not permitted by CSA S6 (2019). While there is a general trend, especially for thicker webs, indicating an increase in the critical buckling stress as the web inclination increases, the extent of this increase is insignificant. For example. For a web thickness of 16 mm, the buckling stress of a 90° web inclination is 27% higher than that of a 76° of web inclination. As the web becomes thinner, the extent of this increase as a result of web inclination diminishes. At a web thickness of 10 mm, the effect is nearly none.

6.4 Effect of Web Stiffener Spacing

The effect of varying the web stiffener spacing, i.e., panel aspect ratio, while keeping the web height constant, is studied in this section. Web stiffeners provide out-of-plane stiffness to the web as well as frame the web panel. Web stiffeners form boundaries for a web panel. Panel aspect ratios of 0.5 to 4.0 were modelled by changing the web stiffener spacing from 1 m to 8 m, in increments of 1 m. Table 6.6 presents the girder geometries included in this portion of the parametric study as well as the FE results. Similar to Sections 6.2 and 6.3, four web thicknesses were included in this section resulting in 32 FE models.

Table 6.6: Geometric properties and FE results per web; effect of stiffener spacing

Model #	h (mm)	w (mm)	θ (°)	h/w	a (mm)	a/h	t _{stiff} (mm)	FE Results	
								σ_{cr} (MPa)	P _{cr} (kN)
D1.1	1985	10	83	200	1000	0.5	16	43.5	1190
D1.2	1985	10	83	200	2000	1.0	16	10.8	721
D1.3	1985	10	83	200	3000	1.5	16	3.9	654
D1.4	1985	10	83	200	4000	2.0	16	3.9	645
D1.5	1985	10	83	200	5000	2.5	16	3.8	643
D1.6	1985	10	83	200	6000	3.0	16	3.8	641
D1.7	1985	10	83	200	7000	3.5	16	3.8	639
D1.8	1985	10	83	200	8000	4.0	16	3.8	638
D2.1	1985	12	83	167	1000	0.5	16	67.1	1830
D2.2	1985	12	83	167	2000	1.0	16	21.3	1169
D2.3	1985	12	83	167	3000	1.5	16	8.9	1082
D2.4	1985	12	83	167	4000	2.0	16	8.4	1070
D2.5	1985	12	83	167	5000	2.5	16	7.6	1064
D2.6	1985	12	83	167	6000	3.0	16	7.5	1060
D2.7	1985	12	83	167	7000	3.5	16	7.5	1056
D2.8	1985	12	83	167	8000	4.0	16	7.7	1051
D3.1	1985	14	83	143	1000	0.5	16	94.7	2591
D3.2	1985	14	83	143	2000	1.0	16	33.3	1731
D3.3	1985	14	83	143	3000	1.5	16	14.9	1626
D3.4	1985	14	83	143	4000	2.0	16	14.8	1606
D3.5	1985	14	83	143	5000	2.5	16	14.7	1596
D3.6	1985	14	83	143	6000	3.0	16	14.6	1587
D3.7	1985	14	83	143	7000	3.5	16	14.5	1579
D3.8	1985	14	83	143	8000	4.0	16	14.4	1569
D4.1	1985	16	83	125	1000	0.5	16	121.5	3440
D4.2	1985	16	83	125	2000	1.0	16	47.1	2398
D4.3	1985	16	83	125	3000	1.5	16	33.8	2263
D4.4	1985	16	83	125	4000	2.0	16	31.6	2233
D4.5	1985	16	83	125	5000	2.5	16	31.3	2215
D4.6	1985	16	83	125	6000	3.0	16	30.5	2199
D4.7	1985	16	83	125	7000	3.5	16	30.3	2184
D4.8	1985	16	83	125	8000	4.0	16	30.1	2167

CSA S6 (2019) does not specify a maximum value for panel aspect ratio for web buckling. However, the code does limit a/h to 3.0 in order to include the effect of tension field action in web shear resistance calculations. In practice, the panel aspect ratio is generally kept below 3.0. However, for the purposes of this parametric study, and because values of a/h

exceeded 3.0 in the table of surveyed bridge girders (see Table 6.1), the maximum a/h ratio modelled was 4.0.

The data from Series D1, D2, D3 and D4 is plotted in Figure 6.5 to show the effect of the web stiffener spacing on the critical buckling stress. For all web thickness studied, the aspect ratio of 2.0 is shown to be the dividing boundary. Below this boundary (i.e., $a/h < 2.0$), an increase in aspect ratio significantly reduces the buckling stress and whereas the aspect ratio effect is negligible above this boundary (i.e., $a/h > 2.0$). The most pronounced reduction in the buckling stress occurs when the aspect ratio increased from 0.5 to 1.5 and the rate of this reduction is nearly the same for all web thicknesses.

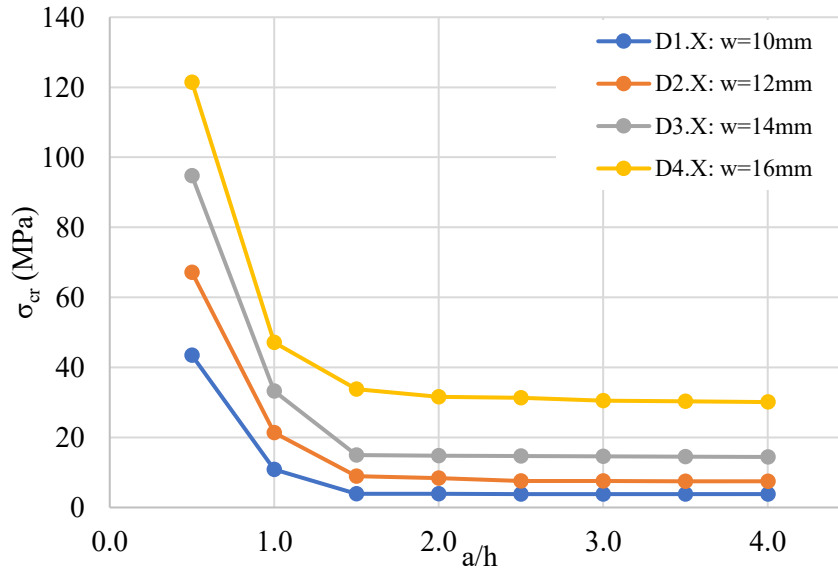


Figure 6.5: Critical buckling stress versus web panel aspect ratio for stiffener spacing of 1m to 8m

6.4.1 Effect of Stiffener Thickness

In this section, the effect of three stiffener thicknesses (16 mm, 25 mm, and 40 mm) on the critical buckling stress were compared. The girder properties from model series D.4 were used as the baseline as this series had 16 mm thick stiffeners. An additional 16 models were created; 8 models with 25 mm thick stiffeners (D5 series) and 8 models with 40 mm thick stiffeners (D6 series). The panel aspect ratios varied from 0.5 to 4.0. In all cases, the stiffeners were modelled as full depth stiffeners with a width of 200 mm. Table 6.7

describes the girder geometries for Series D5 and D6 and presents the FE results.

Table 6.7: Geometric properties and FE results per web; effect of vertical stiffener thickness

Model #	h (mm)	w (mm)	θ (°)	h/w	a (mm)	a/h	t _{stiff} (mm)	FE Results	
								σ_{cr} (MPa)	P _{cr} (kN)
D5.1	1985	16	83	125	1000	0.5	25	138.9	4129
D5.2	1985	16	83	125	2000	1.0	25	69.7	2428
D5.3	1985	16	83	125	3000	1.5	25	44.7	2268
D5.4	1985	16	83	125	4000	2.0	25	42.7	2235
D5.5	1985	16	83	125	5000	2.5	25	39.5	2217
D5.6	1985	16	83	125	6000	3.0	25	35.2	2200
D5.7	1985	16	83	125	7000	3.5	25	34.1	2184
D5.8	1985	16	83	125	8000	4.0	25	33.9	2168
D6.1	1985	16	83	125	1000	0.5	40	140.8	4211
D6.2	1985	16	83	125	2000	1.0	40	70.7	2468
D6.3	1985	16	83	125	3000	1.5	40	46.8	2273
D6.4	1985	16	83	125	4000	2.0	40	44.2	2237
D6.5	1985	16	83	125	5000	2.5	40	41.2	2218
D6.6	1985	16	83	125	6000	3.0	40	37.5	2202
D6.7	1985	16	83	125	7000	3.5	40	35.0	2184
D6.8	1985	16	83	125	8000	4.0	40	33.9	2169

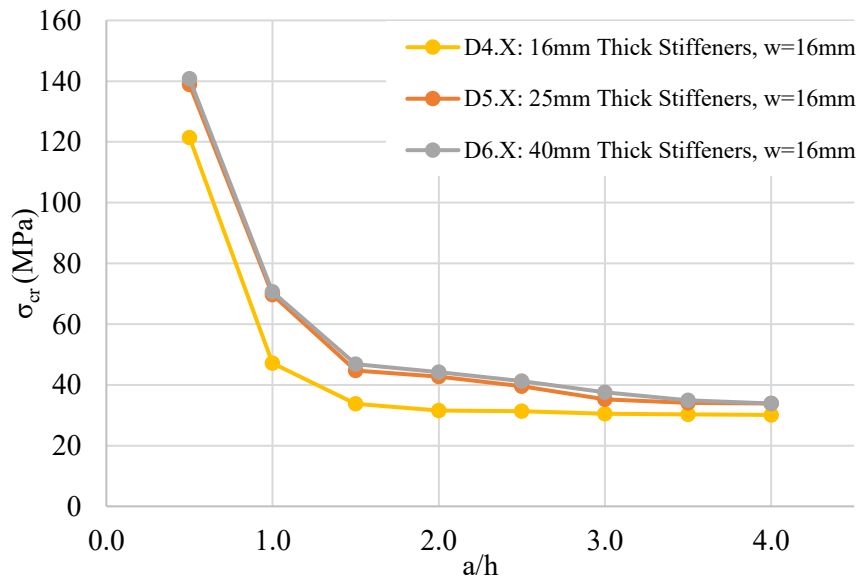


Figure 6.6: Critical buckling stress versus web panel aspect ratio for vertical stiffener thicknesses of 16mm to 40mm

The data from Series D4, D5, and D6 is plotted in Figure 6.6 to demonstrate the effect of the web stiffener thickness on the critical buckling stress. As shown in the figure, an increase in critical buckling stress is evident for the 25 mm thick stiffeners compared to the 16 mm thick stiffeners for all aspect ratios. A further increase in thickness to 40 mm, however, does not result in a noticeable increase in buckling stress. In other words, there is no practical benefit to using 40 mm thick stiffeners instead of 25 mm thick stiffeners to stabilize the girder web. It is also observed that using a thicker web stiffener for increasing the buckling stress is only beneficial for aspect ratios less than 3.

6.5 Effect of Flange Thickness

In this section, the effect of flange thickness, t_1 (top), and t_2 (bottom), on the critical buckling stress is considered. The top and bottom flanges of box girders bound the web plate and therefore are considered as boundary conditions. In order to compare the effectiveness of the top versus bottom flange thickness a normalized ratio of flange thickness to web thickness was used (t_1/w or t_2/w).

Three thicknesses for the top flange and three thicknesses for the bottom flange were studied in combination with two aspect ratios as detailed in Table 6.8. A total of 10 FE models were analyzed in this section. In this series of FE models, the height, thickness, and inclination of the web were kept constant. The height of the web was 1985 mm, the thickness of the web was 14 mm, and the inclination of the web was 83° . The FE results from this section are presented in Table 6.8.

Series E1 and E2 were used to evaluate the top flange effects and Series E3 and E4 were used to evaluate the effect of the bottom flange. The critical buckling stress versus the flange to web ratio is presented in Figure 6.7.

Table 6.8: Geometric properties and FE results per web; effect of flange thickness

Model #	t ₁ (mm)	t ₂ (mm)	h/w	a (mm)	a/h	t ₁ /w	t ₂ /w	FE Results	
								σ _{cr} (MPa)	P _{cr} (kN)
E1.1	30	30	143	5760	2.9	2.1	-	17.8	1777
E1.2	45	30	143	5760	2.9	3.2	2.1	17.8	1583
E1.3	60	30	143	5760	2.9	4.3	-	17.8	1466
E2.1	30	30	143	2880	1.4	2.1	-	32.8	1823
E2.2	45	30	143	2880	1.4	3.2	2.1	32.8	1624
E2.3	60	30	143	2880	1.4	4.3	-	32.8	1501
E3.1	45	40	143	5760	2.9	-	2.9	21.1	1877
E3.2	45	20	143	5760	2.9	-	1.4	12.6	1112
E4.1	45	40	143	2880	1.4	-	2.9	39.8	1992
E4.2	45	20	143	2880	1.4	-	1.4	24.0	1175

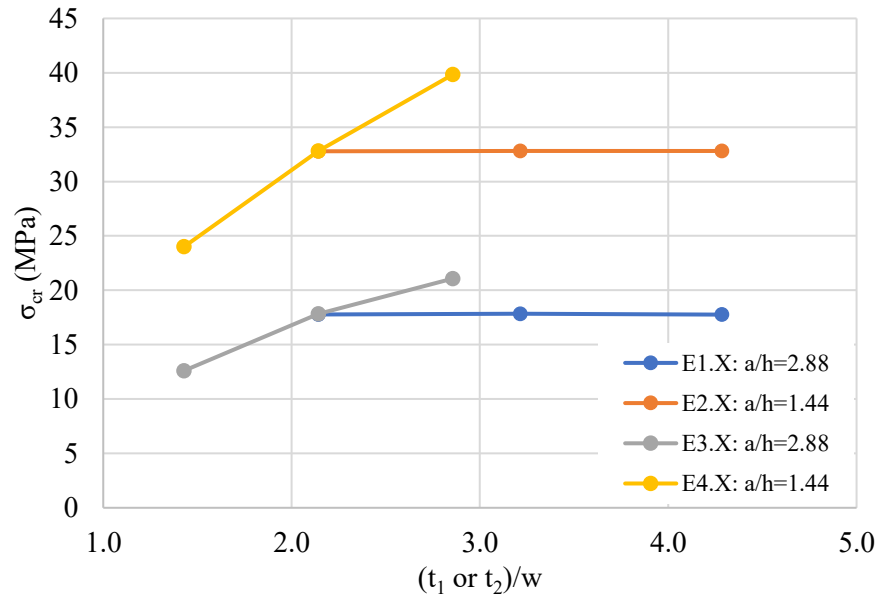


Figure 6.7: Critical buckling stress versus the ratio of flange to web thickness

As shown in Figure 6.7, the orange and blue lines are essentially flat indicating that increasing the thickness of the top flange has no appreciable effect on the critical buckling stress, especially with tall webs. Conversely, the bottom flange appears to have an effect on the critical buckling stress. The yellow and grey lines in Figure 6.7 show that as the ratio of t₂/w increases, σ_{cr} also increases. In the case where the panel aspect ratio is 1.44 (yellow line), a rate of increase of 79% was observed by increasing the bottom flange from 20 to 40 mm. For the panel aspect ratio of 2.88 (grey line), the rate of increase was 42.5%. This indicates that the bottom flange is more effective in providing a boundary restraint

than the top flange. This is expected as the bottom flange, a continuous plate, is expected to provide more stiffness than the top flange consisting of two non-jointed individual plates. In addition, the thicker the bottom flange, the more the patch load is distributed through the flange (i.e., a longer length of web is loaded). Further, comparison of the orange and grey lines shows the effect of flange to web thickness ratio on increasing the buckling stress is more pronounced in the case of aspect ratio of 1.44 vs. 2.88. In other words, the benefit of using a thicker bottom flange is associated with the panel aspect ratio, i.e., distance between web stiffeners. Closely spaced stiffeners enable a greater increase in buckling stress as a result of bottom flange thickness increase than widely spaced stiffeners.

6.6 Effect of Residual Stresses

In design practice, the effects of residual stresses are typically not explicitly included in analysis as the effects are reflected in the load and resistance factors. Residual stresses were not considered in the numerical model verification phase of the research. The effect of residual stresses was studied in this section.

Based on available literature on welding induced residual stresses of plated structures, the idealized residual stress pattern is shown in Figure 6.8 (Asadina & Roddis, 2020) where σ_{RT} and σ_{RC} represent residual tensile and compressive stresses respectively. This pattern was applied to the models with $F_y = 350$ MPa adopted as the value for σ_{RT} for all models. Two levels of compressive residual stress, σ_{RC} , were studied and they were 10% and 25% of F_y , which correspond to ‘medium’ and ‘heavy’ compressive residual stress respectively (Jo et. al, 2020 and Asadnia & Roddis, 2020). The baseline FE models used for the 0% residual stress case were A2 and A4 which had 12 mm and 16 mm thick webs respectively. Residual stresses were applied in the FE models as prestresses in the quadrilateral elements. The widths of the tensile and compressive residual stress blocks were calculated to equalize the magnitudes of compressive and tensile force on each plate element of the cross section (i.e. net longitudinal force on the cross section = 0 kN). Table 6.9 presents the girder geometries and residual stress levels included in this portion of the parametric study and results are shown in Table 6.9 and Figure 6.9.

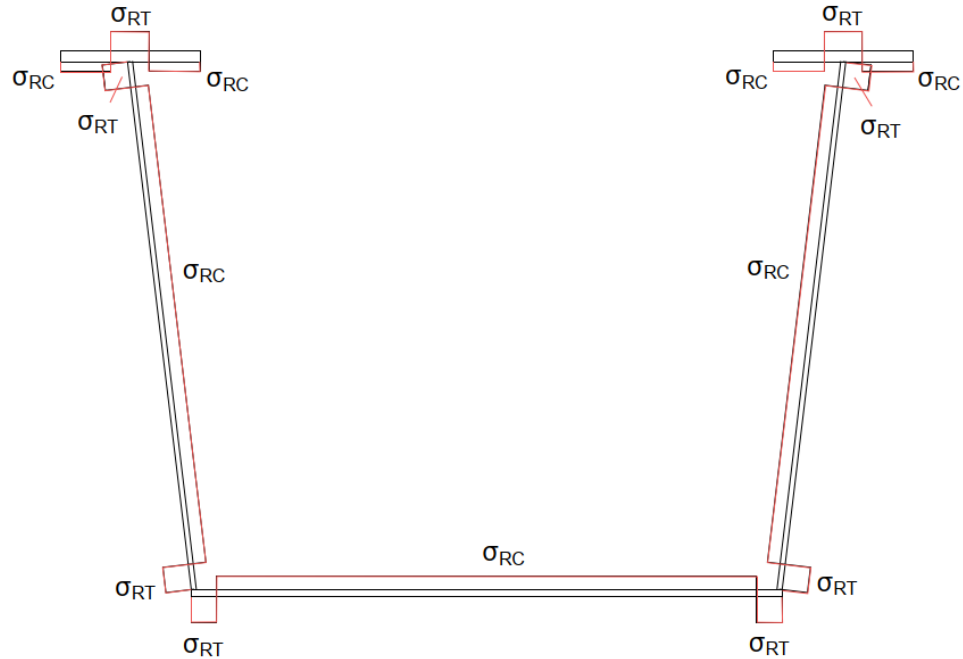


Figure 6.8: Idealized longitudinal residual stress profile applied to the FE models

Table 6.9: Properties of girder models and FE results; effect of residual stresses

Model #	h (mm)	w (mm)	θ (°)	h/w	a/h	σ_{RT} (MPa)	σ_{RC} (MPa)	FE Results	
								σ_{cr} (MPa)	P_{cr} (kN)
F1.1 (A2)	2075	12	83	174	2.8	0	0	7.3	1026
F1.2	2075	12	83	174	2.8	F_y	10% (F_y)	6.7	935
F1.3	2075	12	83	174	2.8	F_y	25% (F_y)	6.1	856
F2.1 (A4)	2075	16	83	131	2.8	F_y	0	32.3	3887
F2.2	2075	16	83	131	2.8	F_y	10% (F_y)	30.3	3641
F2.3	2075	16	83	131	2.8	F_y	25% (F_y)	28.1	3369

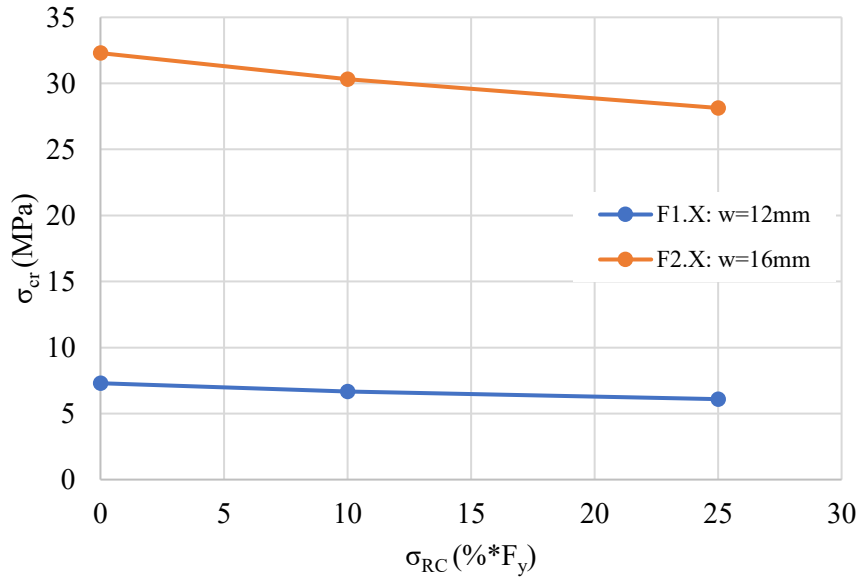


Figure 6.9: Critical buckling stress versus applied residual stress

Series F data is plotted in Figure 6.9 to show the effect of compressive residual stresses on the critical buckling stress for two web thicknesses. In general, the critical buckling stress is reduced as the compressive residual stress increases. The reduction is more pronounced in the case of the thicker web. For the 12 mm thick web case, the rate of reduction in critical buckling stress was 4.8% as the residual stress varied from 0% to 25% whereas the rate of reduction was 16.8% for the 16 mm thick web case. The magnitudes in reduction of critical buckling stress are considered low. It should be reiterated that this study focused on stresses in the elastic range. For the post yield or post buckling regions, presence of residual stresses may have a more profound effect.

6.7 Comparison of P_{cr} with CSA S6 (2019) Web Bearing Resistances

As described in Chapter 2, the current CHBDC evaluates unstiffened web bearing capacity by calculating the web yielding, B_{ty} , and web crippling, B_{rc} , resistances (CSA S6, 2019). For ease of reference, they are reproduced below from Chapter 2.

$$B_{ry} = \Phi_{bi}w(N + 10t)F_y \quad [2.31]$$

$$B_{rc} = 1.45\Phi_{bi}w^2\sqrt{F_yE_s} \quad [2.32]$$

As the web thickness is the main geometric parameter in these equations, the critical buckling loads obtained from the web slenderness FE study were compared with these equations where Φ_{bi} was set as 1.0 for the comparison. It should be pointed out that the calculations consider the web (or portion of) fully yielded or partially yielded (crippled in the inelastic range). While FE results were obtained in the elastic range for panel buckling, the comparison is intended to shed light on applicability of the code web resistance equations on panel buckling evaluation. Values of B_{ry} and B_{rc} for the four web thicknesses considered in the study are provided in Table 6.10.

Table 6.10: B_{ry} and B_{rc} values for web thicknesses considered

Web Thickness (mm)	Eqn. [2.31]	Eqn. [2.32]
	B_{ry} (kN)	B_{rc} (kN)
10	2450	1213
12	2940	1747
14	3430	2378
16	3920	3106

Figure 6.10 shows the P_{cr} values from the FE analysis plotted against the web yielding and crippling resistances. It can be seen that all the FE critical panel buckling loads are less than the web yielding (blue line) and web crippling resistances (green line). In other words, for the panels considered, the web slenderness is in the range that panel buckling in the elastic range is triggered before crippling and yielding. If $\Phi_{bi} = 0.8$ is used for design, the web crippling resistance will compare with the FE results better. However, it still does not fully predict the panel buckling capacity with an adequate safety margin for some results. In conclusion, the web yielding and crippling resistance equations are not sufficient in predicting the panel buckling behaviour and capacity for webs with high slenderness.

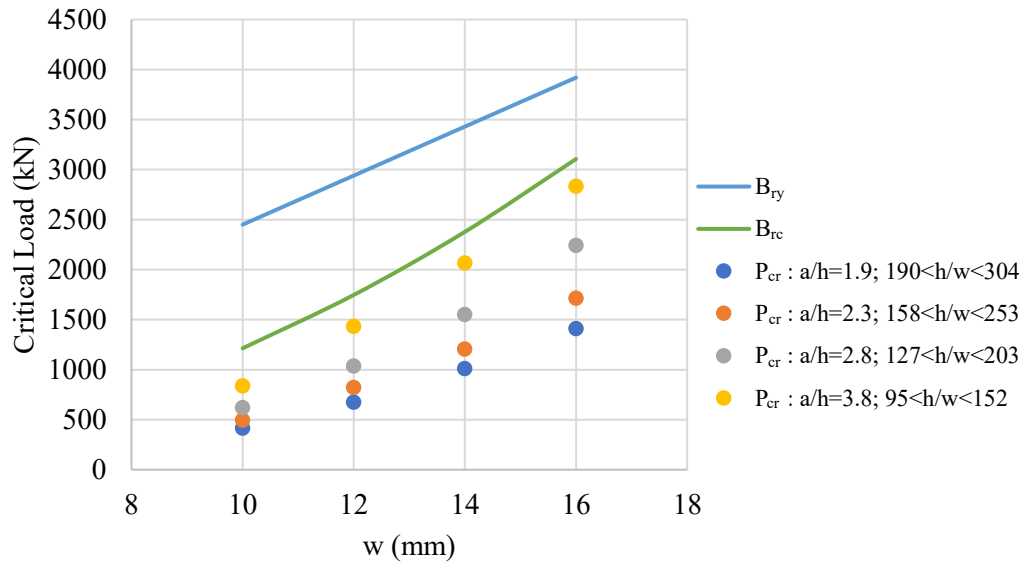


Figure 6.10: Critical load versus web thickness for varying h/w ratios

6.8 Comparison of P_{cr} with Eurocode 3 Part 1-5 (2006)

A comparison of the FE critical buckling loads with the web plate buckling formula currently presented in Eurocode 3 (2006) was also conducted. The Eurocode equations follow the principles of the classic plate buckling theory with a refined evaluation of plate boundary conditions (see Equation [2.43]). However, they have not been verified for large web panels (i.e., large h/w and a/h ratios) commonly found in trapezoidal box girders. Details of the Eurocode equations are found in Chapter 2 and a sample calculation of the critical buckling load using the Eurocode equations is included in Appendix C.

For this comparison, FE study results from the data groups assessing the web slenderness and web aspect ratios were used. Figure 6.11 shows the comparison for critical buckling loads versus h/w ratios for a constant value of a/h. Both FE results and code values show an evident decreasing trend of critical buckling load as h/w increases for all aspect ratios considered. For a given aspect ratio, the Eurocode equations provide an accurate estimate of buckling load as web slenderness h/w varied.

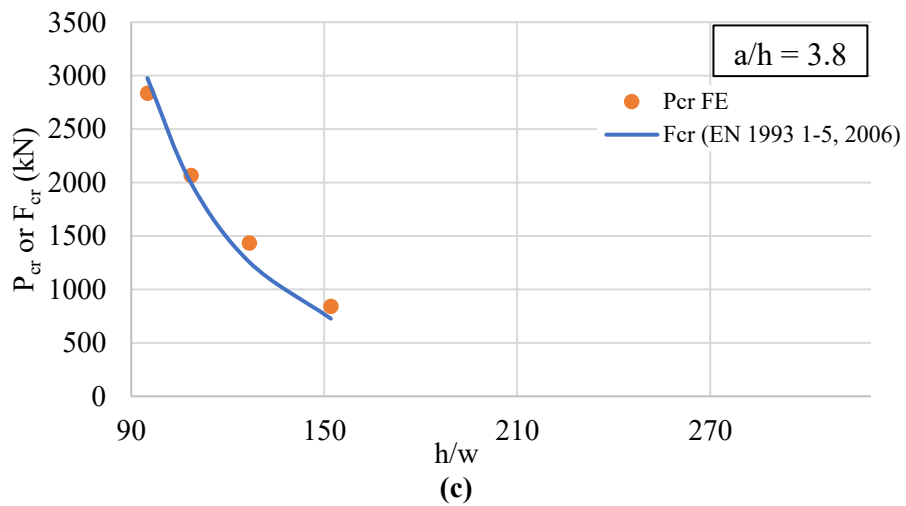
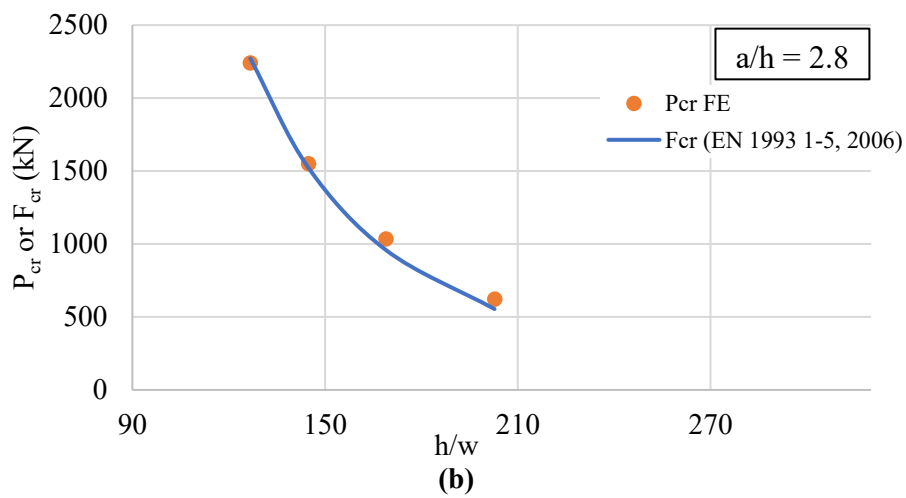
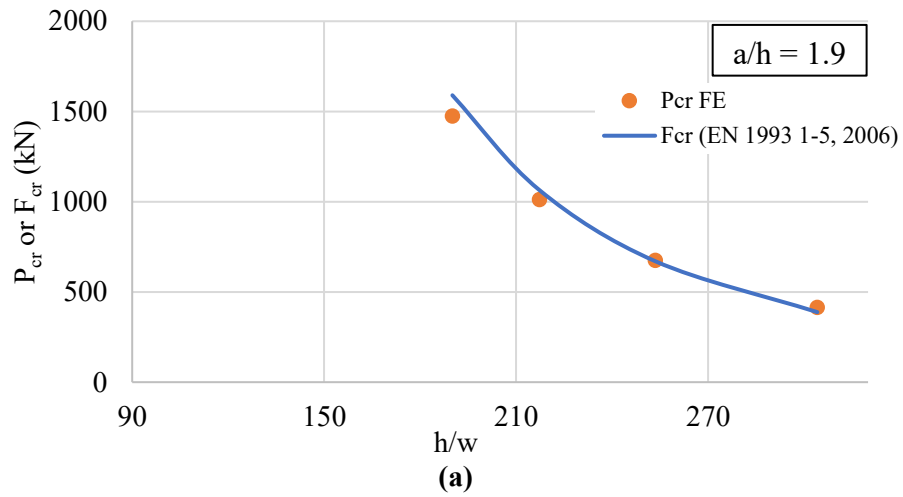


Figure 6.11: Critical load versus h/w for (a) a/h=1.9, (b) a/h=2.8, and (c) a/h=3.8

Figure 6.12 compares the critical buckling loads versus web aspect ratio a/h for a given web slenderness ratio h/w . In general, the Eurocode values compare well with the FE results, both suggesting that a/h of 2.0 is the separation point, beyond which increasing a/h ratio has little effect in changing the critical buckling load.

However, the following discrepancies between the Eurocode values and FE results are noted. For $h/w=125$, the Eurocode values show an overprediction of buckling load for when $a/h < 2.0$. This overprediction is most pronounced when a/h is in the range of 0.5~1.0 with a magnitude of up to 40%. On the other hand, for $h/w=200$, the Eurocode values show an underprediction of buckling load for when $2.0 < a/h < 4.0$ with a magnitude of 15% for this entire aspect range. For $h/w=167$, in between of the two aforementioned slenderness values, the Eurocode values had the best agreement with the FE results.

While developed for evaluation of plate girder web buckling, this comparison exercise shows that the Eurocode performs reasonably well for evaluation of box girder web resistance where panel buckling is concerned. From a practical standpoint, $a/h < 1.0$ and $a/h > 3.0$ are not commonly encountered in practice, the discrepancies as described above may not have practical significance. Overall, the Eurocode equations are proven to be adequate and accurate for the evaluation of web resistance when panel buckling in the elastic range is concerned.

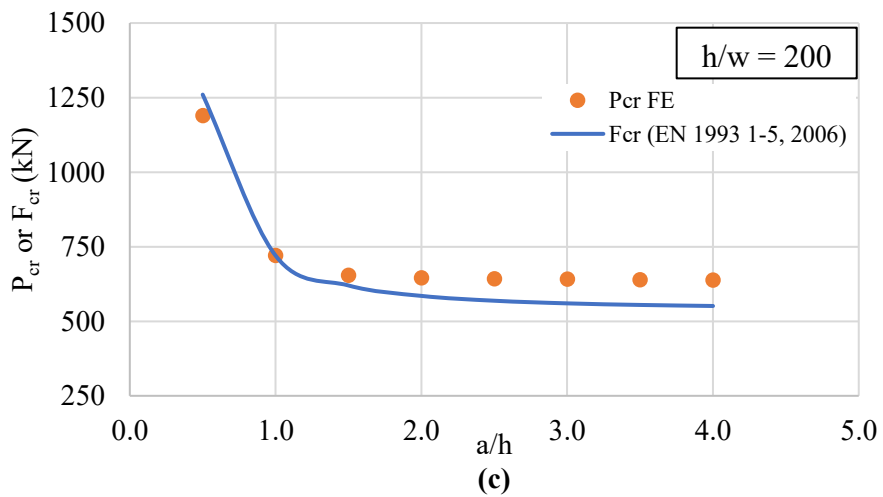
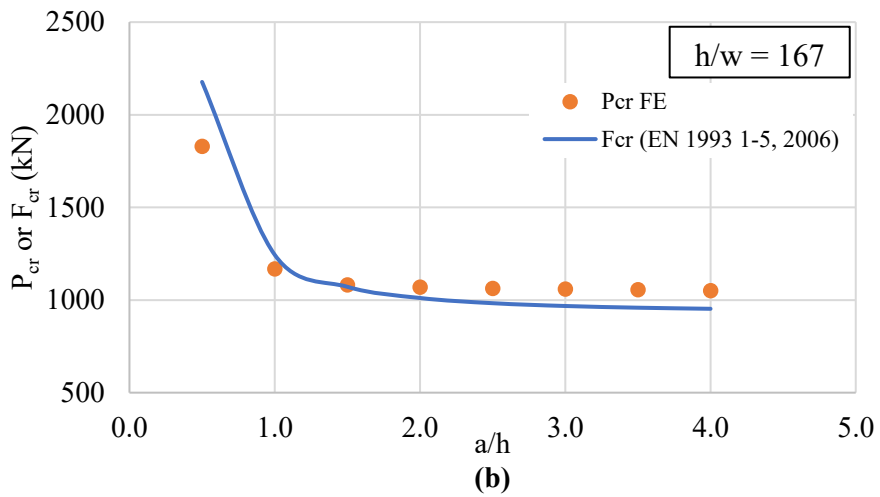
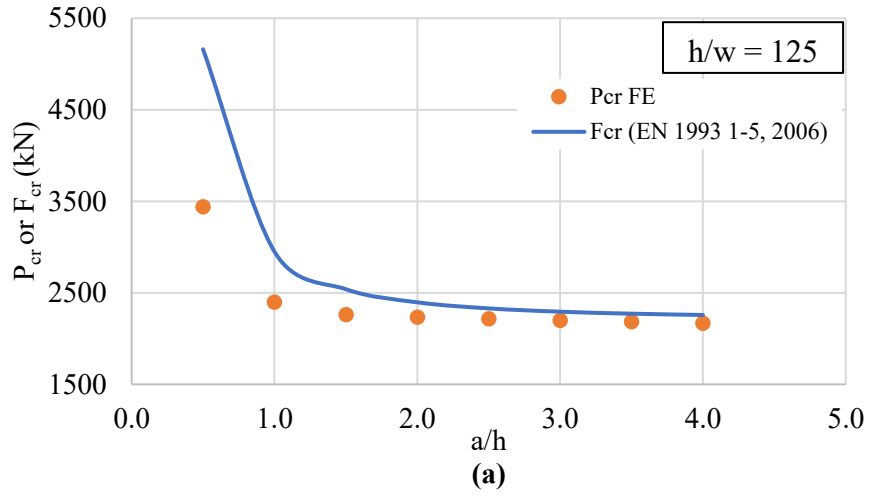


Figure 6.12: Critical load versus a/h for (a) $h/w=125$, (b) $h/w=167$, and (c) $h/w=200$

CHAPTER 7 CONCLUSIONS AND RECOMMENDATIONS

7.1 Summary

This study was conducted to develop an understanding of the buckling capacity of steel box girder webs subjected to reaction forces and bending moments typically encountered during girder erection via incremental launching. Compressive stresses due to reaction forces and negative bending moments found in the lower region of girder webs, especially between vertical stiffener locations, can cause web panels to buckle out of plane when the stress experienced by the web is within the elastic range. The treatment of this panel buckling is not explicitly addressed in CSA S6 (2019). While some guidance is provided in Eurocode 3 Part 1-5 (2006), this had not been evaluated for box girder geometries. This study was then motivated to provide field data supplemented by numerical results to gain a better understanding of panel buckling behaviour and capacity for steel box girders during launching.

In the field monitoring portion, strain gauges were installed on the webs of two steel trapezoidal box girders that were incrementally launched over the Shubenacadie River in Nova Scotia. The purpose of the field monitoring phase was to record stresses in the webs of the girders during erection and to verify the results of subsequent FE models. Significant challenges were encountered with the instrumentation, and the data collected during this phase of the research was deemed not completely reliable.

The numerical portion of the research included the development of finite element models capable of predicting the buckling behaviour and capacity of webs of steel box girders subjected to concentrated compression and flexure. The finite element models were verified using results from the literature. A parametric study was then conducted to investigate the effects of several key geometric parameters on the critical web buckling capacity. Finally, the numerical results were used to assess the critical buckling formula prescribed by Eurocode 3 Part 1-5 with respect to applicability on box girder geometries commonly found in Atlantic Canada.

7.2 Conclusions

The following conclusions are derived from both the field monitoring and FE analysis portions of this research:

- The data collected during the field monitoring phase of the research showed large variations in the recorded data. Although some trends were noticeable between data sets, stress repeatability was not observed/achieved and therefore it was deemed that the field data was not reliable.

- Results from the literature (i.e., work by Granath et al, 1999), were successfully replicated by the FE model. This indicates that the developed model is capable of predicting the buckling behaviour and capacity of girder webs and that FE modelling is a good alternative for further studies.

- Based on the results of the parametric study, the most influential parameters on the web buckling capacity are the web slenderness ratio, h/w , and the web panel aspect ratio, a/h . The critical web buckling stress was assessed over a range of h/w and a/h ratios. The following observations were made:
 - As the web slenderness ratio increases, whether due to the reduction of web thickness or the increase in web height, the critical buckling stress decreases. The rate of reduction, however, diminishes as the web becomes thinner.
 - As the panel aspect ratio increases, the critical buckling stress decreases. However, the decrease is negligible for a/h values greater than approximately 2.0. The failure mode for panels with aspect ratios less than 0.5 was observed to be by web crippling rather than web panel buckling.
 - The effect of increasing the angle of inclination (i.e., increasing the verticality) has a more pronounced effect on thicker webs compared to thinner ones. In the case of thicker webs (16 mm thick for example), as the web inclination increased, the critical buckling stress also increased. However, in the case of thinner webs (10 mm thick for example), the

increase in critical buckling stress from increasing the web inclination was negligible.

- The bottom flange has more pronounced effect on the critical buckling stress than the top flange. As the bottom flange became thicker, the critical buckling stress increased, whereas the increase in the top flange thickness had negligible effect on the critical buckling stress.
 - Two levels of welding included residual stress were included in the parametric study and were found to produce a decrease in critical buckling stress in the order of 15%. It should be noted that this study focused on the stresses in the elastic range and for post yield-or post-buckling regimes, the presence of residual stresses may have a more profound effect.
-
- In this study, the critical web buckling loads were found to be less, significantly less in some cases, than the corresponding web bearing resistances (yielding and crippling) prescribed in CSA S6 (2019). Therefore the web bearing resistance equations are not suitable for predicting the web panel buckling capacity.
 - The critical web buckling equations prescribed in Eurocode 3 Part 1-5 (2006) which was developed for I-shaped plate girders, are shown to predict the critical buckling load of box girder webs with acceptable accuracy for web panels in the elastic stress range.

7.3 Recommendations

The following recommendations and suggestions for future work are developed from observations during the field monitoring and numerical study:

- In lieu of full-scale field testing, scaled box girder geometries, suitable for lab testing could be fabricated.
- Perform field testing in seasons where the weather is more stable or during more thermally neutral seasons (i.e., not in the winter).

- If full scale launch monitoring was to be reconducted, pause the launch at critical cantilever locations and wait until the dynamic effects of the launch are dampened to take a manual reading of the strains. Elaborate continuous monitoring is not required for FE model verification.
- Record test specimen initial out of flatness measurements within the boundaries of an entire web panel for incorporation into the FE model.
- Consider the use of strain rosette (tri-axial) type gauges, instead of bi-axial gauges, in order to capture the full state of stress at a given location on the test specimen.
- Consideration of the restraining effect, due to friction, of the launching rollers on the boundary conditions could be incorporated in future work.
- A FE model with non-linear material and geometric properties should be developed in order to understand the web panel capacity through the entire stress range (i.e., elastic to plastic). Varying levels of bending moment and patch load should be considered in the parametric study to fully capture the critical buckling limits under different loading conditions.

REFERENCES

- AASHTO LRFD Bridge Design Specifications. (2015). Washington, D.C. American Association of State Highway and Transportation Officials.
- American Society for Testing and Materials. (2022). Standard Test Methods and Definitions for Mechanical Testing of Steel Products (ASTM Standard A370-22).
- Asadnia, M., & Roddis, W. M. K. (2019). Strength-Based Out-of-Flatness Tolerance for Bottom Flanges of Steel Box Girders. *Journal of Bridge Engineering*, 25(2)
- Bagchi, D. K., & Rockey, K. C. (1968). A Note on the Buckling of a Plate Girder Web Due to Partial Edge Loadings. International Association for Bridge and Structural Engineering Congress Report, 489-491.
- Baur, Willi. (1977). Bridge Erection by Launching is Fast, Safe and Efficient. *Journal of Civil Engineering Education. American Society of Civil Engineers*, 47(3).
- Bedair, O. (2015). Design Expression for Web Shear Buckling of Box Sections by Accounting for Flange Restraints. *Journal of Constructional Steel Research*, 110, 163-169.
- Bergfelt, A. (1971). Studies and tests on slender plate girders without stiffeners shear strength and local web crippling. *IABSE Reports of the Working Commissions*, 11, 67-83.
- Braun, B., & Kuhlmann, U. (2010, September 8-10). The Interaction Behaviour of Steel Plates Under Transverse Loading, Bending Moment and Shear Force. In E. Batista, P. Vellasco, L. de Lima (Eds.), *International Colloquium on Stability and Ductility of Steel Structures*, Rio de Janeiro, Brazil, (pp. 731-738).
- Campbell Scientific (2006). CR5000 Measurement and Control System: Operator's Manual. Retrieved November 2013 from <http://www.campbellsci.ca/manuals>.
- CAN/CSA S6 (2019). Canadian Highway Bridge Design Code. Canadian Standards Association. Mississauga, Ontario, Canada.
- CAN/CSA S6.1 (2019). Canadian Highway Bridge Design Code Commentary. Canadian Standards Association. Mississauga, Ontario, Canada.
- CAN/CSA W59 (2018). Welded Steel Construction (Metal Arc Welding). Canadian Standards Association. Mississauga, Ontario, Canada.

- Chacón, R., Mirambell, E., & Real, E. (2013). Transversally Stiffened Plate Girders Subjected to Patch Loading. Part 1. Preliminary Study. *Journal of Constructional Steel Research*, 80, 483-491.
- Chacón, R., Mirambell, E., & Real, E. (2013). Transversally Stiffened Plate Girders Subjected to Patch Loading: Part 2. Additional Numerical Study and Design Proposal. *Journal of Constructional Steel Research*, 80, 492-504.
- Chen, H. (1994). *Ultimate Strength and Buckling Behaviour of Stiffened Webs Used in Design of Steel Box Girder Bridges*. [Master's thesis, Concordia University].
- Durkee, Jackson L. (1972). Railway Box-Girder Bridge Erected by Launching. *Journal of the Structural Division, American Society of Civil Engineers*, 98, 1443-1463.
- Elgaaly, M. (1975, November 24). Failure of Thin-Walled Members Under Patch Loading. *3rd International Specialty Conference on Cold-Formed Steel Structures, Paper 7* (pp. 357-381). Missouri University of Science and Technology Scholars' Mine.
- El-Gaaly, M. A., & Rockey, K. C. (1973, October 22). Ultimate Strength of Thin-Walled Members Under Patch Loading and Bending. *International Specialty Conference on Cold-Formed Steel Structures, Paper 2* (pp. 139-167). Missouri University of Science and Technology Scholars' Mine.
- Elgaaly, M., Salkar, R., & Eash, M. Webs Under Compressive Edge Loads. 589-600.
- EN 1993-1-5 (2006). Eurocode 3: Design of Steel Structures Part 1-5: Plated Structural Elements. European Committee for Standardization.
- Google Maps (2015). [Shubenacadie River Bridge Construction Site]. Retrieved July 2015 from <http://www.google.com/maps>.
- Gozzi, J. (2007). *Patch Loading Resistance of Plated Girders – Ultimate and Serviceability Limit State*. [Doctoral Thesis, Luleå University of Technology].
- Graciano, C. (2015). Patch Loading Resistance of Longitudinally Stiffened Girders – A Systematic Review. *Journal of Thin-Walled Structures*, 95, 1-6.
- Graciano, C., & Ayesterán, A. (2013). Steel Plate Girder Webs Under Combined Patch Loading, Bending and Shear. *Journal of Constructional Steel Research*, 80, 202-212.
- Graciano, C., & Casanova, E. (2005). Ultimate Strength of Longitudinally Stiffened I-Girder Webs Subjected to Combined Patch Loading and Bending. *Journal of Constructional Steel Research*, 61, 93-111.

- Graciano, C., & Lagerqvist, O. (2003). Critical Buckling of Longitudinally Stiffened Webs Subjected to Compressive Edge Loads. *Journal of Constructional Steel Research*, 59, 1119-1146.
- Granath, P., & Lagerqvist, O. (1999). Behaviour of Girder Webs Subjected to Patch Loading. *Journal of Constructional Steel Research*, 50, 49-69.
- Jo, E.-J., Vu, Q.-V., & Kim, S.-E. (2020). Effect of Residual Stress and Geometric Imperfection on the Strength of Steel Box Girders. *Steel and Composite Structures*, 34(3), 423-440.
- Johansson, B., & Lagerqvist, O. (1995). Resistance of Plate Edges to Concentrated Forces. *Journal of Constructional Steel Research*, 32, 69-105.
- Johansson, B., Maquoi, R., & Sedlacek, G. (2001). New Design Rules for Plated Structures in Eurocode 3. *Journal of Constructional Steel Research*, 57, 279-311.
- Khan, M. Z., & Johns, K. C. (1975). Buckling of Web Plates Under Combined Loadings. *Journal of the Structural Division, Proceedings of the American Society of Civil Engineers*, 101(ST10), 2079-2092.
- Khan, M., Paradowska, A., Uy, B., Mashiri, F., & Tao, Z. (2016). Residual Stresses in High Strength Steel Welded Box Sections. *Journal of Constructional Steel Research*, 116, 55-64.
- Kovacevic, S., Ceranic, A., & Markovic, N. (2021). Patch Load Resistance of Longitudinally Stiffened Steel Plate Girders: A Parametric Study. *Ernst & Sohn*, 2107-2114.
- Kulak, G.L., and Grondin, G.Y. (2010). Limit States Design in Structural Steel (9th ed.). Canadian Institute of Steel Construction, Markham, ON, CAN.
- Lagerqvist, O., & Johansson, B. (1996). Resistance of I-Girders to Concentrated Loads. *Journal of Constructional Steel Research*, 39(2), 87-119.
- Loaiza, N., Graciano, C., & Chacón, R. (2019). Influence of the Patch Loading Length on the Buckling Coefficient of Longitudinally Stiffened Plate Girders. *Revista Facultad de Ingeniería, Universidad de Antioquia*, 91, 60-69.
- Altair® S-FRAME 3D Structural Analysis Software, Enterprise Edition, Version 2022.2, 1995-2022 Altair Engineering Canada.
- Maiorana, E., Pellegrino, C., & Modena, C. (2008). Linear Buckling Analysis of Unstiffened Plates Subjected to Both Patch Load and Bending Moment. *Journal of Engineering Structures*, 30(12), 3731-3738.

- Paik, J. K., Thayamballi, A. K., & Lee, J. M. (2004). Effect of Initial Deflection Shape on the Ultimate Strength Behavior of Welded Steel Plates Under Biaxial Compressive Loads. *Journal of Ship Research*, 48(1), 45-60.
- Roberts, T. M. (1981). Slender Plate Girders Subjected to Edge Loading. *Proceedings of the Institution of Civil Engineers, Part 2*, 71, 805-819.
- Roberts, T. M., & Markovic, N. (1983). Technical Note 352 Stocky Plate Girders Subjected to Edge Loading. *Proceedings of the Institution of Civil Engineers, Part 2*, 75, 539-550.
- Roberts, T. M., & Newark, A. C. B. (1997). Strength of Webs Subjected to Compressive Edge Loading. *Journal of Structural Engineering*, 123, 176-183.
- Roberts, T. M., & Rockey, K. C. (1979). A Mechanism Solution for Predicting the Collapse Loads of Slender Plate Girders When Subjected to In-Plane Patch Loading. *Proceedings of the Institution of Civil Engineers, Part 2*, 67(1), 155-175.
- Roberts, T. M., & Shahabian, F. (2001). Ultimate Resistance of Slender Web Panels to Combined Bending Shear and Patch Loading. *Journal of Constructional Steel Research*, 57, 779-790.
- Sennah, K. M., & Kennedy, J. B. (2002). Literature Review in Analysis of Box-Girder Bridges. *Journal of Bridge Engineering*, 7(2), 134-143.
- Shahabian, F., & Roberts, T. M. (1999). Buckling of Slender Web Plates Subjected to Combinations of In-Plane Loading. *Journal of Constructional Steel Research*, 51, 99-121.
- Shahabian, F., & Roberts, T. M. (2000). Combined Shear-And-Patch Loading of Plate Girders. *Journal of Structural Engineering*, 126, 316-321.
- Shimizu, S. (1994). The collapse behaviour of web plates on the launching shoe. *Journal of Constructional Steel Research*, 31(1), 59-72.
- Tang, Q. (2005). *Web bearing resistance of beams framing over column caps*. [Masters thesis, Dalhousie University].
- Timoshenko, S. P., & Gere, J. M. (1961). *Theory of Elastic Stability*. New York: McGraw-Hill.
- Tupula Yamba, François-Xavier (1981) *Buckling behaviour of steel box-girder bridges*. [PhD thesis, Concordia University].

- Vishay. 2007. Tech Note TN-514: Shunt Calibration of Strain Gage Instrumentation. Vishay Micro-Measurements. Retrieved November 2013 from <http://www.vishaypg.com/micro-measurements/stress-analysis-strain-gages/technotes-list/>.
- Wolchuk, R. (1980). Proposed Specifications for Steel Box Girder Bridges. *Journal of the Structural Division, Proceedings of the American Society of Civil Engineers*, 106(12), 2463-2474.
- Wolchuk, R. (1981). Design Rules for Steel Box Girder Bridges. International Association for Bridge and Structural Engineering Proceedings, 49-60.
- Zetlin, L. (1995). Elastic Instability of Flat Plates Subjected to Partial Edge Loads. *Proceedings of the American Society of Civil Engineers, Paper 795, 81*, 1-24.
- Zhang, Y., & Luo, R. (2012). Patch Loading and Improved Measures of Incremental Launching of Steel Box Girder. *Journal of Constructional Steel Research*, 68(1), 11-19.
- Ziemian, R. D. (2010). *Guide to Stability Design Criteria for Metal Structures* (Sixth ed.). John Wiley & Sons.

APPENDIX A

Table A.11: Procedure to determine the critical buckling height, H_{cr} , of Girder G1:

Step 1

Determine global load Effects at ends of three-bay long girder segment:

Shubenacadie 2D Girder Global Load Effects Summary						
G1-A6		Cantilever Length = 31855 mm				
Location of RXN:	West Abutment	Dead Load Moment (kN-m)	Dead Load Shear (kN)	V_{DL} West (kN)	V_{DL} East (kN)	RXN (kN)
West	3 Bay	-2618	354			
	CL Field	-5550		492	-397	889
East	3 Bay	-2567	-237			

Step 2

Determine G1 section properties at strain gauge location:

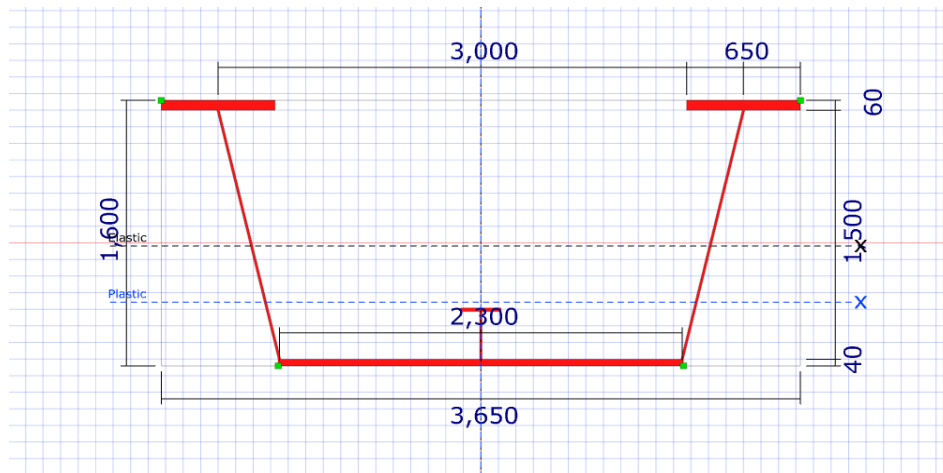


Figure A.1: G1-A cross section (S-Frame, 2023)

G1-A Section Properties		
Area (A)	223000	mm ²
Elastic Centroid Offset X (X)	1825	mm
Elastic Centroid Offset Y (Y)	722	mm
Moment of Inertia X (Ix)	1.12E+11	mm ⁴
Moment of Inertia Y (Iy)	2.96E+11	mm ⁴
Elastic Section Modulus Bottom X (Sx2)	1.55E+08	mm ³
Elastic Section Modulus Top X (Sx1)	1.28E+08	mm ³

Step 3

Determine nodal forces to apply in FE model:

S-Frame Inputs: G1-A		Top Flg. Stress (MPa)	Top Flg. Force (kN)	Bot. Flg. Stress (MPa)	Bot. Flg. Force (kN)	Web Force Per Node (kN)	Roller Force Per Node (kN)
West	3 Bay	-20.5	-1595.3	-16.9	-1621.5	11.8	88.9
	CL Field	-43.4	-3382.0	-35.8	-3437.4	11.8	88.9
East	3 Bay	-20.1	-1564.3	-16.6	-1589.9	-7.9	88.9

Step 4

Perform buckling analysis to determine the point of maximum web deflection and obtain H_{cr} :

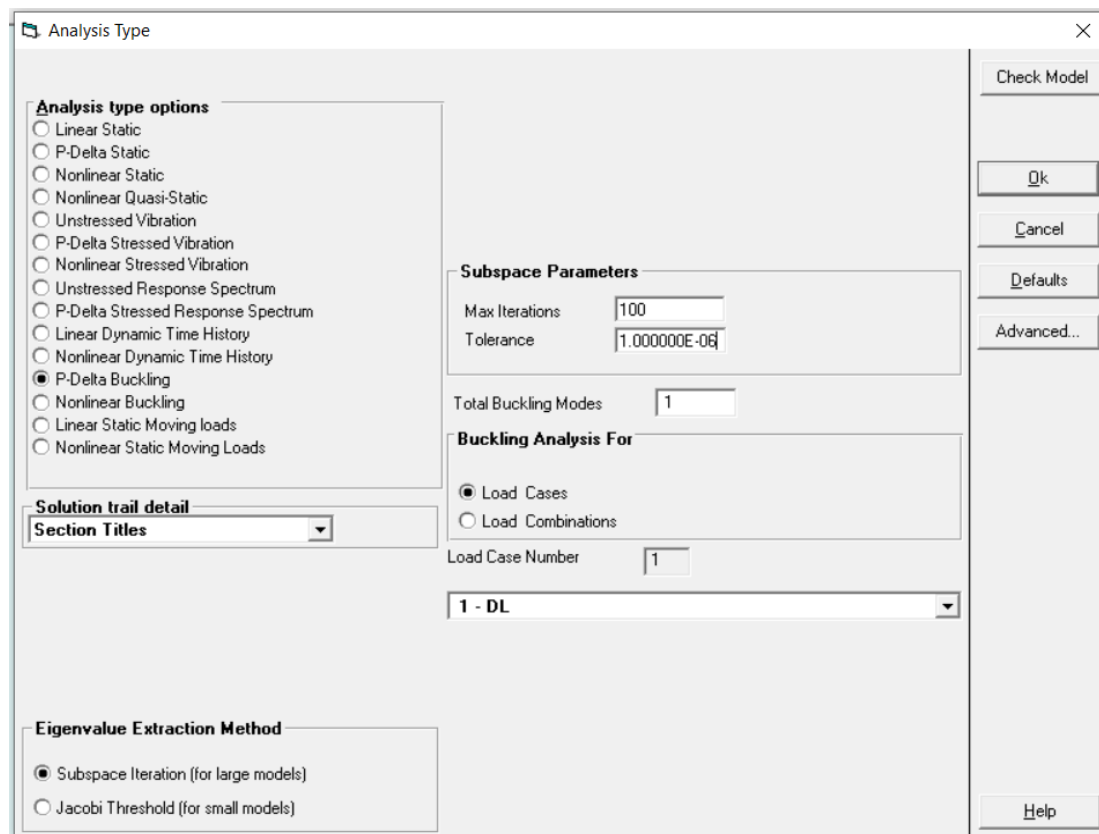
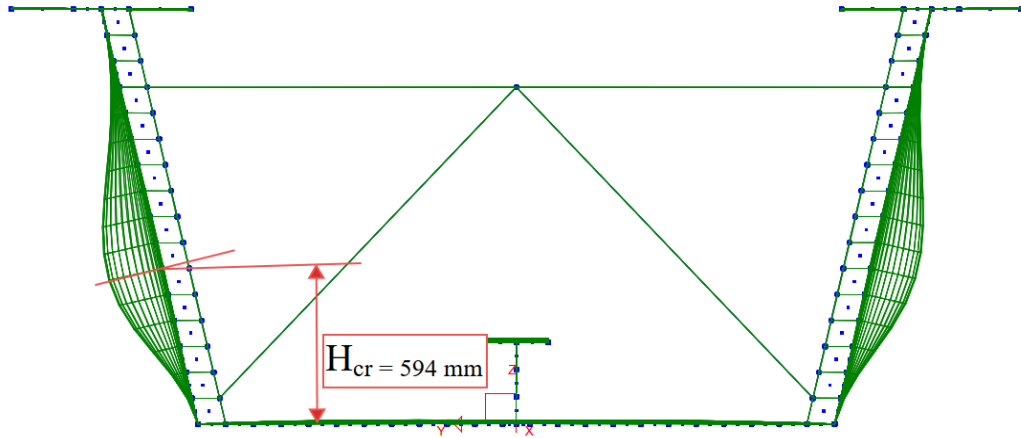


Figure A.2: G1-A buckling analysis set up (S-Frame, 2023)

Step 4 Continued:



ALTAIR

S-FRAME

Enterprise Version 2022.2.0
© 1995-2022 Altair Engineering Canada, Ltd.

Figure A.3: G1-A buckled shape and H_{cr} (S-Frame, 2023)

Table A.12: Procedure to determine the critical buckling height, H_{cr} , of Girder G2:

Step 1

Determine global load Effects at ends of three-bay long girder segment:

Shubenacadie 2D Girder Global Load Effects Summary						
G2-A6		Cantilever Length = 19390 mm				
Location of RXN:	West Abutment	Dead Load Moment (kN-m)	Dead Load Shear (kN)	V_{DL} West (kN)	V_{DL} East (kN)	RXN (kN)
West	3 Bay	-223	150			
	CL Field	-1959		261	-202	463
East	3 Bay	-640	-115			

Step 2

Determine G2 section properties at strain gauge location:



Figure A.4: G2-A cross section (S-Frame, 2023)

G2-A Section Properties		
Area (A)	114000	mm ²
Elastic Centroid Offset X (X)	1700	mm
Elastic Centroid Offset Y (Y)	566	mm
Moment of Inertia X (Ix)	4.44E+10	mm ⁴
Moment of Inertia Y (Iy)	1.44E+11	mm ⁴
Elastic Section Modulus Bottom X (Sx2)	7.84E+07	mm ³
Elastic Section Modulus Top X (Sx1)	4.52E+07	mm ³
Elastic Section Modulus Y (Sy)	84800000	mm ³

Step 3

Determine nodal forces to apply in FE model:

S-Frame Inputs: G2-A		Top Flg. Stress (MPA)	Top Flg. Force (kN)	Bot. Flg. Stress (MPA)	Bot. Flg. Force (kN)	Web Force Per Node (kN)	Roller Force Per Node (kN)
West	3 Bay	-3.9	-108.6	-2.1	-152.9	5.0	
	CL Field	-34.1	-953.9	-18.7	-1343.3		46.3
East	3 Bay	-14.2	-283.2	-8.2	-431.0	-3.8	

Step 4

Perform buckling analysis to determine the point of maximum web deflection and obtain H_{cr} :

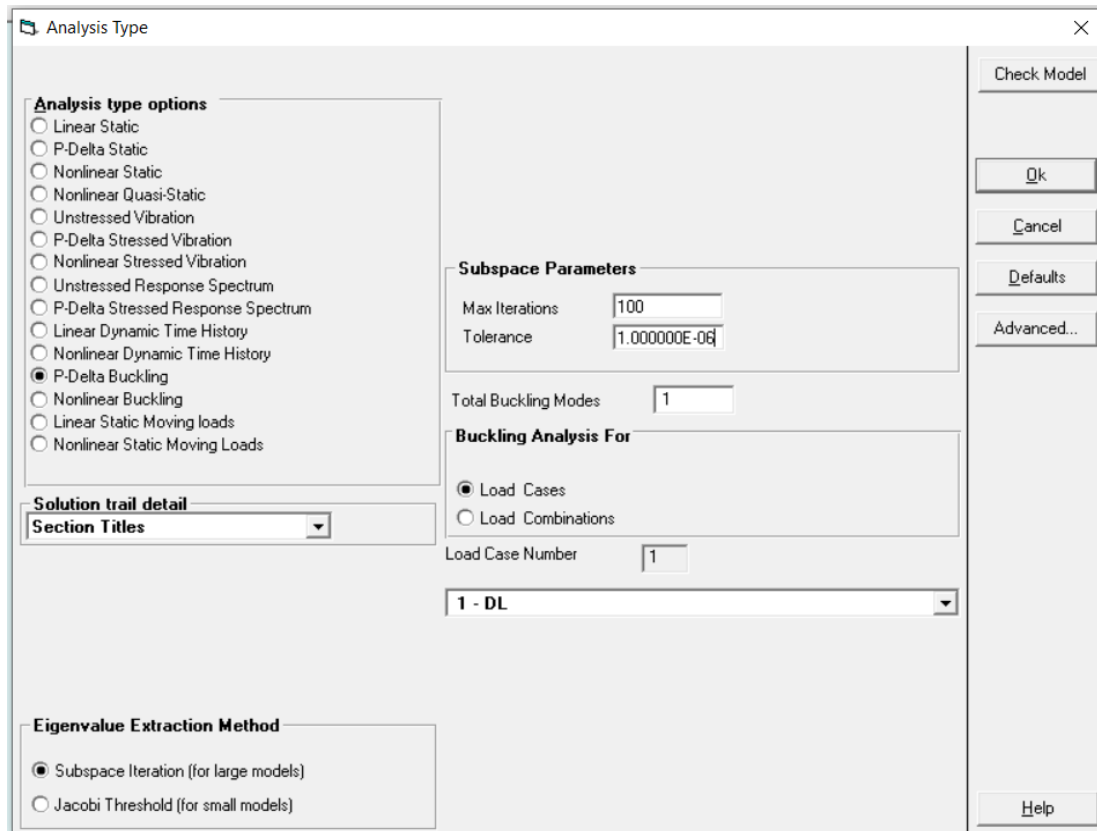
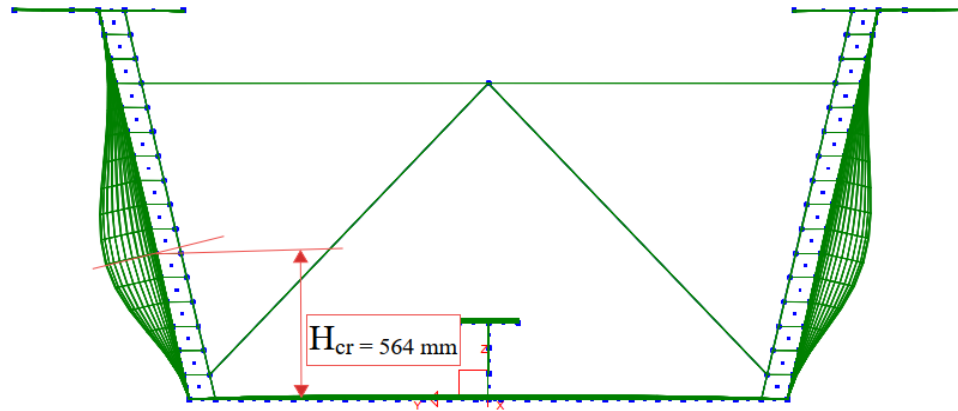


Figure A.5: G2-A buckling analysis set up (S-Frame, 2023)

Step 4 Continued:



ALTAIR

S-FRAME

Enterprise Version 2022.2.0
© 1995-2022 Altair Engineering Canada, Ltd.

Figure A.6: G2-A buckled shape and H_{cr} (S-Frame, 2023)

APPENDIX B

Table B.1: Strain gauge properties - G1

Channel / Gauge #	Gauge Type		Orientation	Gauge Factor
1	Uniaxial	SGD-5/350-LY11	Vertical	2.14
2	Biaxial	SGD-3/350-RYB21	Vertical	2
3	Biaxial	SGD-3/350-RYB21	Horizontal	2
4	Uniaxial	SGD-5/350-LY11	Vertical	2.14
5	Biaxial	SGD-3/350-RYB21	Vertical	2
6	Biaxial	SGD-3/350-RYB21	Horizontal	2
7	Biaxial	SGD-3/350-RYB21	Vertical	2
8	Biaxial	SGD-3/350-RYB21	Horizontal	2
9	Biaxial	SGD-3/350-RYB21	Vertical	2
10	Biaxial	SGD-3/350-RYB21	Horizontal	2
11	Uniaxial	SGD-5/350-LY11	Vertical	2.14
12	Biaxial	SGD-3/350-RYB21	Vertical	2
13	Biaxial	SGD-3/350-RYB21	Horizontal	2
14	Uniaxial	SGD-5/350-LY11	Vertical	2.14
15	Uniaxial	SGD-5/350-LY11	Vertical	2.14
16	Biaxial	SGD-3/350-RYB21	Vertical	1.99
17	Biaxial	SGD-3/350-RYB21	Horizontal	1.99
18	Uniaxial	SGD-5/350-LY11	Vertical	2.14
19	Biaxial	SGD-3/350-RYB21	Vertical	1.99
20	Biaxial	SGD-3/350-RYB21	Horizontal	1.99
21	Biaxial	SGD-3/350-RYB21	Vertical	2
22	Biaxial	SGD-3/350-RYB21	Horizontal	2
23	Biaxial	SGD-3/350-RYB21	Vertical	1.99
24	Biaxial	SGD-3/350-RYB21	Horizontal	1.99
25	Uniaxial	SGD-5/350-LY11	Vertical	2.14
26	Biaxial	SGD-3/350-RYB21	Vertical	2
27	Biaxial	SGD-3/350-RYB21	Horizontal	2
28	Uniaxial	SGD-5/350-LY11	Vertical	2.14
30	Uniaxial	SGD-5/350-LY11	Longitudinal	2.14
32	Uniaxial	SGD-7/350-LY11	Temperature	2.14

Notes:

1. Manufacturer: Omega Strain Gauges
2. SGD Series Specifications:
 - a. Service Temperature: -75 to 200°C
 - b. Max. Strain: 30 000 micro strain
 - c. Excitation Voltage: 9.5 to 13V
 - d. Gauge Resistance 350Ω

Table B.2: Strain gauge properties - G2

Channel / Gauge #	Gauge Type		Orientation	Gauge Factor
1	Uniaxial	SGD-7/350-LY11	Vertical	2.14
2	Biaxial	SGD-3/350-RYB21	Vertical	2
3	Biaxial	SGD-3/350-RYB21	Horizontal	2
4	Uniaxial	SGD-7/350-LY11	Vertical	2.14
5	Biaxial	SGD-6/350-RYB21	Vertical	2.13
6	Biaxial	SGD-6/350-RYB21	Horizontal	2.13
7	Biaxial	SGD-6/350-RYB21	Vertical	2.13
8	Biaxial	SGD-6/350-RYB21	Horizontal	2.13
9	Biaxial	SGD-3/350-RYB21	Vertical	2
10	Biaxial	SGD-3/350-RYB21	Horizontal	2
11	Uniaxial	SGD-7/350-LY11	Vertical	2.14
12	Biaxial	SGD-3/350-RYB21	Vertical	2
13	Biaxial	SGD-3/350-RYB21	Horizontal	2
14	Uniaxial	SGD-7/350-LY11	Vertical	2.14
15	Uniaxial	SGD-7/350-LY11	Vertical	2.14
16	Biaxial	SGD-3/350-RYB21	Vertical	2
17	Biaxial	SGD-3/350-RYB21	Horizontal	2
18	Uniaxial	SGD-7/350-LY11	Vertical	2.14
19	Biaxial	SGD-6/350-RYB21	Vertical	2.13
20	Biaxial	SGD-6/350-RYB21	Horizontal	2.13
21	Biaxial	SGD-6/350-RYB21	Vertical	2.13
22	Biaxial	SGD-6/350-RYB21	Horizontal	2.13
23	Biaxial	SGD-3/350-RYB21	Vertical	2
24	Biaxial	SGD-3/350-RYB21	Horizontal	2
25	Uniaxial	SGD-7/350-LY11	Vertical	2.14
26	Biaxial	SGD-6/350-RYB21	Vertical	2.13
27	Biaxial	SGD-6/350-RYB21	Horizontal	2.13
28	Uniaxial	SGD-7/350-LY11	Vertical	2.14
29	Biaxial	SGD-3/350-RYB21	Transverse	2
30	Biaxial	SGD-3/350-RYB21	Longitudinal	2
31	Uniaxial	SGD-7/350-LY11	Longitudinal	2.14
32	Uniaxial	SGD-7/350-LY11	Temperature	2.14

Notes:

1. Manufacturer: Omega Strain Gauges
2. SGD Series Specifications:
 - a. Service Temperature: -75 to 200°C
 - b. Max. Strain: 30 000 micro strain
 - c. Excitation Voltage: 9.5 to 13V
 - d. Gauge Resistance 350Ω

APPENDIX C

Table C.1: Worked example - critical buckling stress

<u>Step 1</u>				
Determine global load Effects at ends of one-bay long girder segment:				
Model #: B3.2				
Global Load Effects:		Dead Load Moment (kN-m)	Dead Load Shear (kN)	RXN (kN)
West	1 Bay	-3500	350	700
East	1 Bay	-3500	-350	
Cantilever length = 20 m				
<u>Step 2</u>				
Determine girder section properties at critical section (section directly above the leading roller support):				
Figure C.1: Box girder section schematic				
B3.2 Section Properties:				
b_1 (mm)	550	w_1 (mm)	2970	
t_1 (mm)	42	Web slope ($^\circ$)	81	
b_2 (mm)	2300	S_{top} (mm ³)	1.15E+08	
t_2 (mm)	30	S_{bottom} (mm ³)	1.6058E+08	
h (mm)	2000	$A_{top\ fl}$ (mm ²)	46200	
w (mm)	14	$A_{bottom\ fl}$ (mm ²)	69000	

Step 3

Determine axial flange forces, web shear forces, and roller reaction forces:

σ_{top} (MPa)	30.45
Top Flange Force (kN)	1407
σ_{bottom} (MPa)	21.80
Bottom Flange Force (kN)	1504
Shear Force per web (kN)	175
Roller Reaction per web (kN)	350

Step 4

Discretize FE model and calculate nodal forces:

Model Discretization:		Load Inputs at 1-Bay Extents:	
# Top Flange Nodes	14	Top Flange Force per Node (kN)	100.5
# Bottom Flange Nodes	25	Bottom Flange Force per Node (kN)	60.2
# Web Nodes (per web)	20	Web Force per Node (kN)	8.75
# Roller Nodes (per web)	5	Roller Force per Node (kN)	70

Step 4 Continued

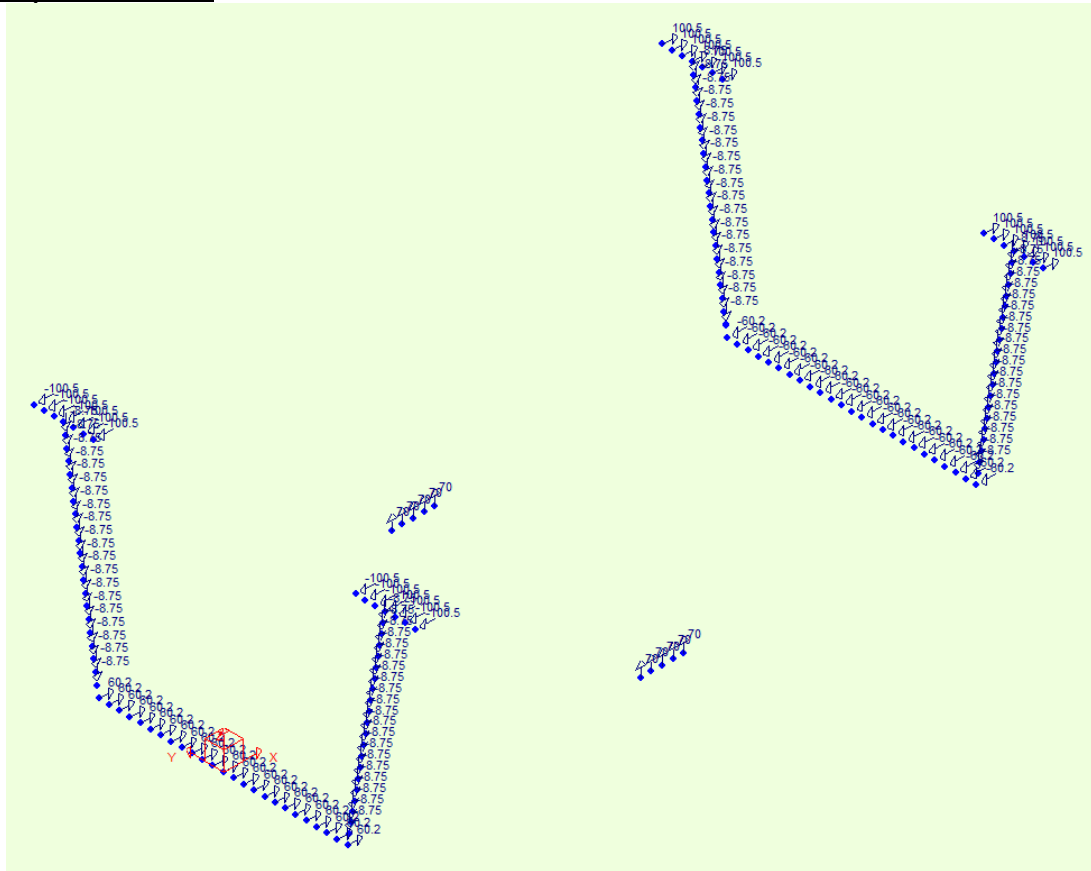


Figure C.2: Nodal loads applied in FE model (S-Frame, 2023)

Step 5

Run buckling analysis (see Appendix A for analysis type dialogue box (S-Frame 2023)).

Scale resulting mode shape to 8 mm maximum web amplitude. Save geometry as the initial geometric imperfection:

Step 5 Continued

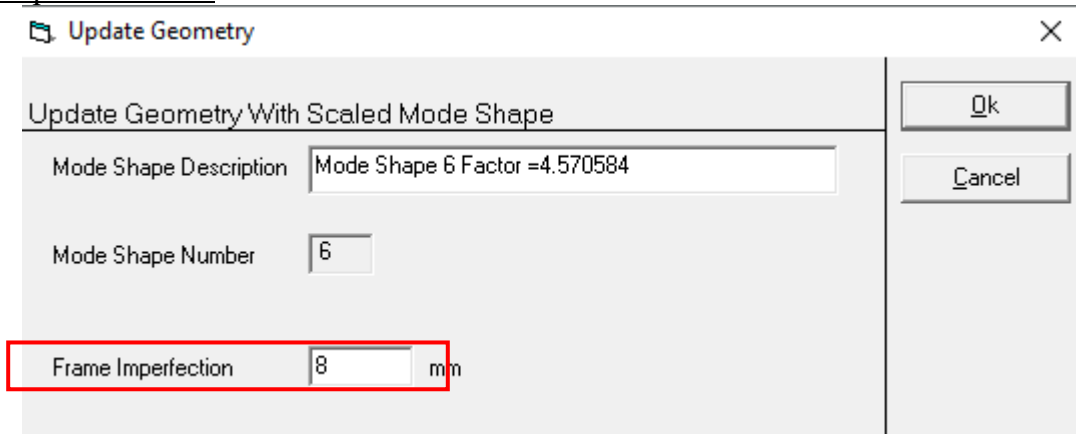


Figure C.3: Example of update geometry window; 8 mm imperfection applied (S-Frame, 2023)

Step 6

Run non-linear buckling analysis to obtain buckling factor, λ , and critical buckling height H_{cr} :

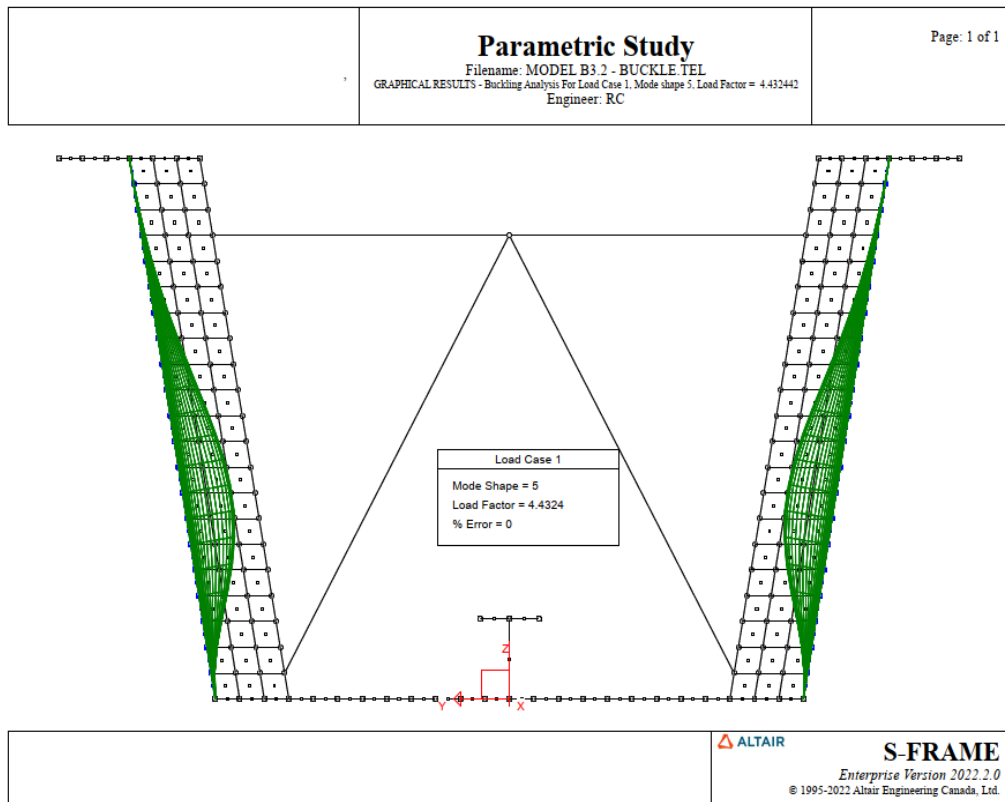


Figure C.4: Model B3.2 buckled shape and H_{cr} (S-Frame, 2023)

Step 6 Continued

Results:

$$\lambda = 4.4324$$

$$H_{cr} = 800 \text{ mm}$$

Step 7

Run non-linear static analysis and extract web stress at H_{cr} :

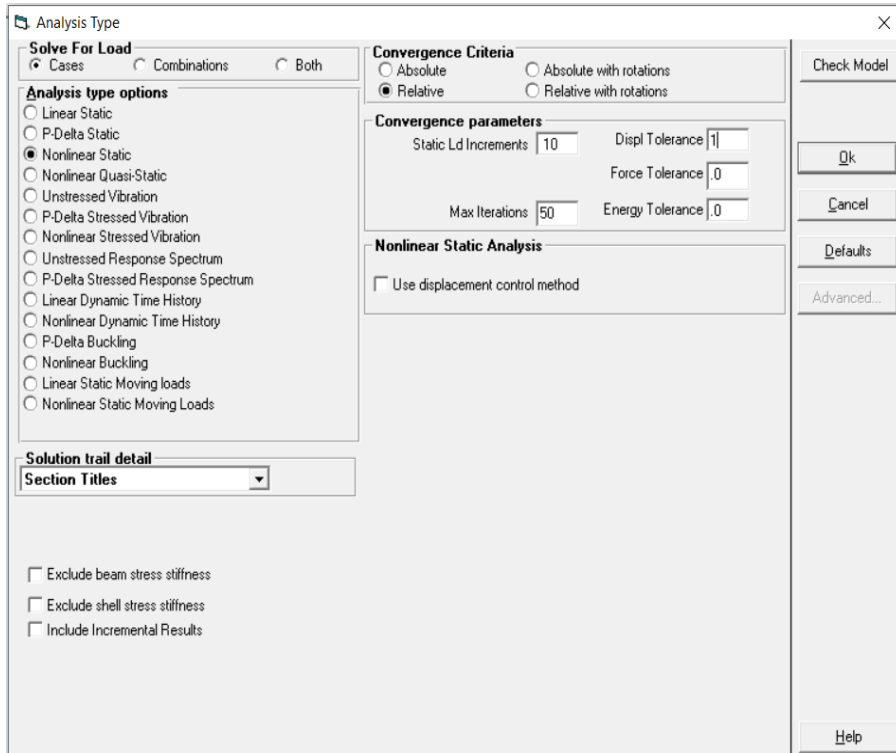


Figure C.5: Non-linear analysis set up (S-Frame, 2023)

Step 7 Continued

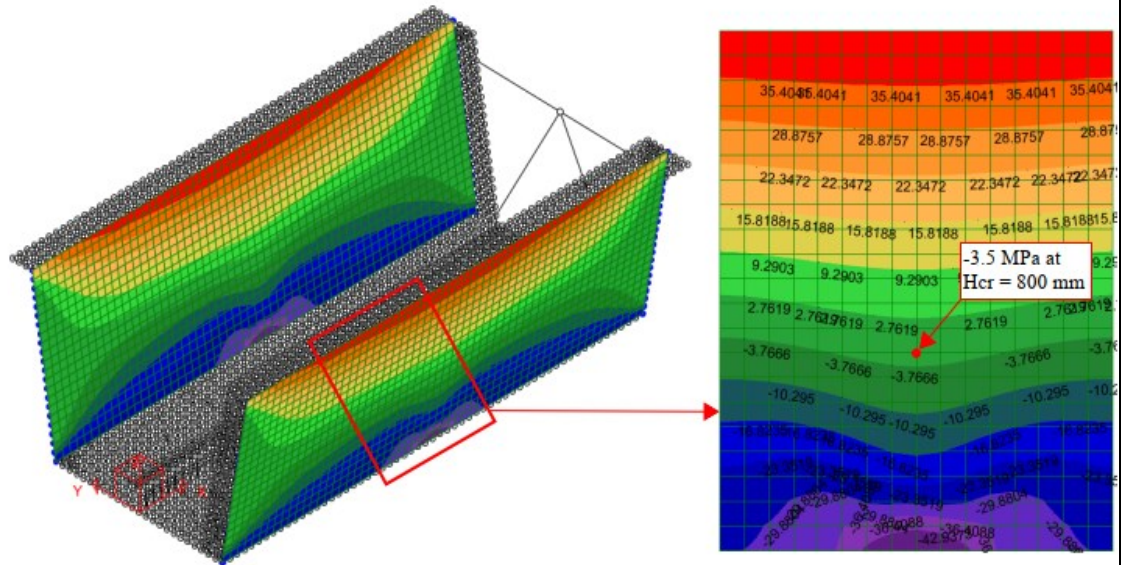


Figure C.6: Model B3.2 non-linear static stress results (S-Frame, 2023)

Result:
 $\sigma = -3.5 \text{ MPa}$

Step 8

Calculate σ_{cr} :

$$\sigma_{cr} = \lambda * \sigma$$

$$\sigma_{cr} = (4.4324) * (-3.5) = 15.5 \text{ MPa (Compression)}$$

Calculate P_{cr} :

$$P_{cr} = \lambda * (\text{Roller Rxn})$$

$$P_{cr} = (4.4324) * (350) = 1551 \text{ kN}$$

Table C.2: Calculation of B_{ry} and B_{rc} from CHBDC (CSA S6, 2019)

CHBDC (CSA, 2019) Clause: 10.10.8

$$B_r = \Phi_{bi} w (N + 10t) F_y$$

$$B_r = 1.45 \Phi_{bi} w^2 \sqrt{F_y E_s}$$

$$E_s = 200000 \text{ MPa}$$

$$F_y = 350 \text{ MPa}$$

$$N = 400 \text{ mm}$$

$$w = 14 \text{ mm}$$

$$t = 30 \text{ mm}$$

$$\phi_{bi} = 1.0$$

Results:

$$B_{ry} = 3430 \text{ kN}$$

$$B_{rc} = 2378 \text{ kN}$$

Table C.3 Calculation of F_{cr} from Eurocode 3 (EN 1993 1-5, 2006)

Eurocode 3 (EN 1993 1-5, 2006)

$$F_{cr} = 0.9k_F E \frac{t_w^3}{h_w}$$

$$k_F = 6 + 2 \left(\frac{h_w}{a} \right)^2$$

E =	200000	MPa
t_w =	14	mm
h_w slope =	2028	mm
a =	5760	mm

Results:

k_f =	6.25
F_{cr} =	1522 kN